Functional cementitious composites with micro-sized particulate fillers for additive construction and energy-efficient buildings

A Dissertation Presented for the

Doctor of Philosophy

Degree

The University of Tennessee, Knoxville

Adam Lee Brooks

December 2023

Acknowledgements

This research was made possible by the U.S. Department of Energy (DOE) Building Technology Office (DE-EE-0008677), the National Science Foundation (CMMI-1563551, CMMI-1954517, CMMI-1663302), and by University of Tennessee, Knoxville (UTK) startup funds. The content of this paper does not reflect of view of the funding agencies. This research would not be possible without the support and assistance of many colleagues throughout the process: Zhenglia Shen, Dominic Hanna, Babak Salarieh, Yawen He, Yucen Li, Peyman Zandifaez, and the many undergraduate assistants as well.

I would like to thank my advisor Dr. Hongyu "Nick" Zhou for convincing me do pursue a graduate degree when I was an undergraduate researcher and for all the guidance and trust he placed in me on numerous projects and experiments. I would also like to thank my committee members: Dr. Baoshan Huang, Dr. Som Shrestha, and Dr. Shuai Li for all their support. The UTK Civil engineering administrative and technical staff were always there to make sure that t's were crossed and i's were dotted, that supplies were orders, fixtures fabricated, and testing facilities were maintained.

Finally, I would like to thank my family and friends that have supported me and believed in me throughout this process. My parents who were always there when to listen and encourage me. My sister and brother-in-law who did not always understand why I was doing this but were always there when I needed an escape from the stress. And of course, my wonderful wife who was always my guiding light during every storm and never waivered in her belief in me and my choices.

Abstract

With a growing energy demand, the development of sustainable and energy efficient building materials is growing rapidly. Numerous researches have focused on low carbon footprint construction materials, high-performance thermal insulations, high-performance façade, and thermal energy storage. Among these, the development of functional cementitious composites has attracted significant attention due to its potential utilities in building energy reduction and decarbonatization efforts. For example, fly ash cenospheres have been used as micro-size lightweight fillers to achieve low density and thermal conductivity. The use of phase change materials (PCM) in concrete has been studied to answer energy demands. While their inclusion into concrete has been achieved, the encapsulation methods have left questions about their implementation and use. Current research uses micro-encapsulation in a soft polymer shell, resulting in low strengths and greatly limiting their applicability.

This research aims to address these concerns by studying the synergistic role of micro-size functional additives (MSFA), specifically core-shell particles (CSP) with rigid shells, in developing functional cementitious composites that can be used in buildings to enable reduction in thermal loads and energy consumption while maintaining their ability to support mechanical loads as well as to serve architectural functionalities. This was achieved through a series of multiscale experimental and numerical studies. First, a broad scale study of MSFA were conducted on cementitious composites with CPSs by investigating both the thermal conductivities and mechanical performance. This study demonstrated the ability of rigid CSPs to reduce the self-weight and thermal conductivity while maintaining/increasing the mortars strength. Based on this study, cenospheres were used in further studies to identify the hierarchical relationship with both normal and light weight aggregates in concrete and

component forms. At the same time the rigid shell MSFA were used to replace the polymer shell in the micro-encapsulation process to achieve both high thermal storage capabilities while maintaining high strength. Component level panels were poured using cenosphere encapsulated PCM to evaluate their performance in an active thermal energy storage system, and testing is ongoing. Finally, micro-encapsulated PCM was evaluated for the use in the emerging additive manufacturing of cementitious composites by incorporating it into 3d printing “inks”.

Table of Contents

Chapter 1. Introduction and literature review 1

1.1 Background 2
1.2 Literature review 4
1.2.1 Lightweight functional cementitious composites for reduced self-weight 4
1.2.2 Lightweight functional cementitious composites for increased thermal insulation. 7
1.2.3 Thermal energy storage 8
1.2.4 Cementitious composites for additive construction (3D printing) 12

Chapter 2. Problem statement and Research objective 15

2.1 Problem Statement 16
2.2 Research objectives 18

Chapter 3. Cementitious composites containing functional micro-sized fillers 22

3.1 Effects of micro-sized fillers on the mechanical and thermal performance of functional cementitious composites 23
3.1.1 Material preparation and mix design 23
3.1.2 Thermal property test using Transient Plane Source (TPS) method 28
3.1.3 Mechanical testing 29
3.1.4. Thermal test results 29
3.1.5 Compressive strength 34
3.1.6 Microstructures and fracture topography 39
3.1.7 Thermal conductivity of LWCC containing particulate LWFs 44
3.1.8 Thermal conductivity and strength: the implication on building structural and energy performance 50
3.2 Thermal energy storage cementitious composites 54
3.2.1 Preparation of fly-ash cenopshere encapsulated phase change material (CenoPCM) .. 54
3.2.2 Thermophysical properties of CenoPCM 58
3.2.3 Mix design and materials preparation 63
3.2.4 Experimental method and setup 66
3.2.5 Thermal properties 70
3.2.6. Elastic modulus 73
3.2.7 Compressive strength 75
3.2.8 Fracture toughness 77

Chapter 4. Lightweight concrete containing micro-sized functional fillers 82

4.1 Mixture design and material preparation 83
4.2 Experimental setup for mechanical tests 89
4.3 Thermal property measurement using transient plane source (TPS) method 93
4.4 Mechanical properties 94
4.5 Thermal properties 98

4.6 Effects of aggregates and binder materials 101
4.7 Microstructures and damage 102
4.8 Balancing mechanical and thermal properties of LWCs 111
4.9. A two-step homogenization scheme 112
4.10. Effective thermal properties of lightweight concrete containing FAC 112

Chapter 5. Building envelopes 117

5.1 Small-scale calibrated hot box apparatus setup and calibration 118
5.1.1. Instrumentation and setup 118
5.1.2 Calibration 121
5.2. Thermal performance characterization of wall panels 123
5.2.1 Specimen design 123
5.3 Mechanical performance of small scale concrete sandwich panels 129
5.3.1 Experimental setup for uniaxial compression 131
5.3.2 Mechanical behavior 135

Chapter 6. Towards future additive construction 142

6.1 Material design of 3D printable mixture design incorporating TES 143
6.2 Fresh properties and printing parameters 148
6.2.1 Concrete 3D printer setup 148
6.3 Evaluation of effects of MEPCM on printing parameters 148
6.3.1 Experimental procedures 148
6.3.2 Flowability 151
6.3.3 Extrudability 153
6.3.4 Buildability 153
6.4 Thermal properties of cementitious composites containing MEPCM 157
6.4.1 Energy storage capacity 157
6.4.2 Thermal conductivity 159
6.5 Microstructure and mechanical properties 165
6.5.1 Microstructures 165

Chapter 7. Conclusions 175

Bibliography 180

Vita 192

List of Tables

Table 1. Properties of the lightweight particle filler (LWF) materials used in this research 25
Table 2. Density, mechanical, and thermal properties of the tested mixture groups 37
Table 3. Properties of the MEPCM materials used in this research 60
Table 4. Mixture design of cementitious composites (no silica sand) containing CenoPCM 62
Table 5. Test matrix and mix proportions (by weight, kg of materials/m3 of concrete). 65
Table 6. Density, mechanical, and thermal properties of the tested mixture groups 72
Table 7. Fracture Toughness test results 79
Table 8. Test matrix and mix proportions (by weight, kg of materials/ m^3 of concrete) 85
Table 9. Aggregate properties 90
Table 10. Experimental results* 95
Table 11. Energy input, loss, and test panel R-value 124
Table 12. Thermal properties of concrete materials 126
Table 13. Concrete sandwich wall panel composition and thermal transmittance 128
Table 14. Test matrix and mix proportions (by weight, kg of materials/ m^3 of concrete) 133
Table 15. Properties of the MEPCM 147
Table 16. Extrudability of printing materials with different contents of PCM 154
Table 17. DSC test results for cement paste and cement mortar containing MEPCM 158
Table 18. Thermal properties of the tested mixture groups 163
Table 19. Density, mechanical, and thermal properties of the tested mixture groups 170

List of Figures

Figure 1: The hierarchical microstructure of lightweight cementitious composite materials containing fly-ash cenosphere (FAC) fillers 17
Figure 2: Interactions between MSFA, material properties, and structural and building application. 19
Figure 3: Characterization of fly ash cenospheres (FAC): 27
Figure 4: The Transient Plane Source (TPS) tests for determining thermal properties: 30
Figure 5: Picture showing the mechanical test setup. 31
Figure 6: Thermal properties of LWCC tested through Transient Plane Source (TPS) method: . 33
Figure 7: Compressive strength vs. dry density of LWCCs containing: 35
Figure 8: SEM images showing the microstructure of LWCC containing: 41
Figure 9: Fracture topography showing the fracture surfaces of LWCCs containing: 43
Figure 10: Microstructure and effective thermal conductivity of lightweight cementitious composite (LWCC): 46
Figure 11: Comparisons between the predicted thermal conductivities as functions of the LWF volume fraction 49
Figure 12: Thermal and mechanical properties map of LWCC. 51
Figure 13: Correlations between compressive strength, thermal resistance (R-value), and the volume fraction of LWF particles 53
Figure 14: Properties of the fly-ash cenosphere (FAC) used for microencapsulation and the Micronal MEPCM: 56
Figure 15: CenoPCM production: 57
Figure 16: Thermophysical Properties of MEPCM: 61
Figure 17: Effects of cementitious matrix on the CenoPCM properties: 64
Figure 18: Experimental set-ups for mechanical and thermal testing. 67
Figure 19: Fracture toughness: 69
Figure 20: Thermal properties of LWCC tested through Transient Plane Source (TPS) method: (a) Thermal conductivity; (b) Volumetric heat capacity above and below phase change temperature (sensible heat) 71
Figure 21: Elastic moduli of cementitious composites containing MEPCM: 74
Figure 22: Compressive strength of cementitious composites containing MEPCM: 76
Figure 23: SEM image showing microcracking and damaged cementitious composites containing MEPCM: 78
Figure 24: Results of the fracture toughness tests on cementitious composites containing Micronal® and CenoPCM: 80
Figure 25: Common ingredients within structural lightweight concrete 86
Figure 26: The mercury intrusion porosimetry (MIP) test and SEM imaging performed on RiverLite™ LWA 87
Figure 27: Characterization test performed on aggregates: 88
Figure 28: Mechanical test setup: 91

Figure 29: The Transient Plane Source (TPS) method for thermal constants analysis: 92
Figure 30: Mechanical property relationships: 97
Figure 31: Thermal properties of LWCC tested through Transient Plane Source (TPS) method: 99
Figure 32: Effect of aggregates and binder materials: 100
Figure 33: Optical microscopic images of lightweight aggregate concrete: 104
Figure 34: SEM image showing the hierarchical microstructure the FAC-filled micro-cellular cementitious matrix and LWA 105
Figure 35: Fracture topographic images: (a) NWC (reference); (b) LWC with coarse LWA; (c) LWC with fine NWA substitute by FAC and fine LWA; and (d) LWC with 100% substitution of fine and coarse NWA 108
Figure 36: Stress-strain behavior: 109
Figure 37: Thermo-mechanical relationships: 110
Figure 38: Microstructure and effective thermal conductivity of lightweight cementitious composite (LWCC): 113
Figure 39: Comparison between calculated and experimental results: 116
Figure 40: Hot box setup and instrumentation: 120
Figure 41: The scaled-down concrete sandwich wall panel specimen for thermal testing: 127
Figure 42: Hot box testing results versus finite different method simulated results and thermal properties of tested panels: 130
Figure 43: Scaled-down concrete sandwich wall panel specimen for mechanical testing: 132
Figure 44: Experimental set up for scaled concrete sandwich panels under uniaxial loading. .. 134
Figure 45: Force deflection curves for small scale concrete sandwich panels. 137
Figure 46: Failure of scaled down concrete sandwich panels 138
Figure 47: Failure of fiber reinforced concrete wythe: 141
Figure 48: Conceptual design showing strategically placed thermal energy storage enabled by 3D printed cementitious materials charged with microencapsulated PCM (MEPCM). 145
Figure 49: Illustrative figure showing the mixing and printing process of cementitious composites charged with MEPCM. 146
Figure 50: Printer System: 149
Figure 51: Material flow effects: 152
Figure 52: Visual representation of print quality for different extrusion rates and print head velocity: 155
Figure 53: buildability properties of printed material: 156
Figure 54: Differential scanning calorimetry (DSC) results obtained on cement paste and M68 mortars with Micronal® MEPCM: 160
Figure 55: Transient plane source (TPS) test setup for thermal conductivity measurement: 161
Figure 56: Thermal properties of printed LWCC tested through Transient Plane Source (TPS) method: 164
Figure 57: SEM images of cast vs. printed cementitious composite (M68) samples: 166
Figure 58: Mechanical property testing of printed LWCC: 169

Figure 59: Mechanical properties of printed LWCC: 172
Figure 60: Failure mode of printed sample with Mic6: 173

Chapter 1. Introduction and literature review

1.1 Background

The global energy consumption has increase roughly 92% between 1971 and 2014 [1] With the building sector consumes approximately 40% of all energy produced within the United States, of which 43% is attributed to heating, ventilation, and air conditioning (HVAC) [2]. It is projected that an annual average increase of 0.4% and 0.5% for the next 30 years in the residential and commercial sectors respectively [3]. Curbing energy demand and use trends is essential going forward with growing populations and limited natural resources. High energy costs and the need to reduce greenhouse gas emissions can be mitigated with higher qualities of thermal management to reduce a building's operational energy and the associated greenhouse gas emissions is critical for its life-time sustainability. Since energy consumed in space heating and cooling constitutes a major portion of a building's total energy consumption [4], minimizing the heat loss through the building envelope is critical to increase energy efficiency while maintaining acceptable structural, environmental, and occupant comfort performance.

In recent years, development of energy-saving technologies for buildings have continued to grow. With many of these researches focused on building materials like low carbon footprint construction materials [5–9], high-performance thermal insulations [4, 13, 10] high-performance façade [16–19], and thermal energy storage [20–26]. In addition, advanced construction techniques include concrete 3D printing (C3DP) [27] have also been actively investigated to lower the energy demand and reduce material waste during the construction process.

Cementitious materials, including concrete, occupies 664 billion USD worth of the global construction market and is one of the most important sections in the construction materials sector [28]. Cementitious and concrete composites are generally referred as to composite material systems with cementitious binders. The word cement is interpreted in a wide sense, including not only Portland cement but also blended cements and other binding materials such as alkali-

activated binders. In addition to conventional concrete materials, cementitious composites cover a wide range of composite materials such as fiber-reinforced cement composites, polymer impregnated composites, and cement composites containing special functional inclusions, special aggregates, or waste materials. The versatility of their material composition gives rise to numerous special properties and functionalities to cementitious composites that are promising for building and infrastructure applications, including high ductility (strain hardening [29–34]), lightweight (ultra-lightweight [15–19]), self-healing [38,39], thermal energy storage [10-15], and good thermal insulation [43–46] .

In particular, a specific type of micro-sized functional fillers, core-shell particles (CSPs), have been increasingly studied for functional cementitious composites and concretes. More specifically, hollow fly-ash cenosphere (FAC) and hollow glass microspheres (HGM) have been used to develop lightweight and ultra-lightweight cementitious composites (LCC/ULCC) [47–51] that have the potential to be used in load-bearing structural components [47,48]. The particles are typically hollow with a nearly 70-90 vol% air core and a thin rigid shell. This has allowed CSPs to be explored as new micro-encapsulation methods for functional additives and catalysts in cementitious composites. For example, micro-encapsulated phase-changing materials (MEPCMs) have been mixed into cement mortar/ concrete for saving building operational energy [52,53] through the use of thermal energy storage. In such applications, organic PCMs (e.g., paraffin) are typically encapsulated in microcapsules with medium diameter of 1 to a few hundred microns and a capsule thickness of a few microns, to prevent the leakage of liquid PCM and the reaction with the cementitious matrix [52,53]. Other applications of CSP in cementitious materials include self-healing concretes that contain microcapsules filled with healing agents such as mineral compounds and bacteria [38].

For materials that are used as thermal insulation or when the cooling/heating rate is critical for their functionality (e.g., PCM), the heat transfer in cementitious material containing CSP is of great interest [48,54]. Moreover, the mechanical properties (e.g., elastic modulus and strength) rely heavily on the shell properties of the encapsulation materials which can lead to an inferior cementitious matrix, thus the inclusion of soft shelled CSPs into the matrix could result in substantial degradation of mechanical properties [55,56]. Whereas studies indicated that using rigid shell encapsulation materials such as FAC may circumvent the strength and stiffness loss [50,51,57]. Thus, for functional cementitious composites that also bear mechanical stress, it is essential to understand how the inclusion of CSPs would influence their mechanical properties.

1.2 Literature review

1.2.1 Lightweight functional cementitious composites for reduced self-weight

Traditionally, lightweight concretes are produced by incorporating lightweight course aggregates (LWA) such as expanded perlite [10–12], shale [13,58,59], and expanded clay [60] into concrete. Due to its advantageous properties including low density, good thermal insulation and fire resistance, lightweight concrete (LWC) has been widely studied both as structural and nonstructural building material [60]. The density of structural LWAC normally varies between 1500 to 2000 kg/m3 depending on the type and volume fraction of LWA used. While the unit weight of conventional LWAC materials has been successfully achieved within the stipulated guidelines [14,15], traditional LWAC has shown lower mechanical strength and reduced performance such as impaired durability [60] and brittle failure [61]. While the goal of lightweight concretes is to reduce the total self-weight of concrete structures/ components, most is only applicable to non-load bearing areas/members. In order to circumvent the drawbacks presented by traditional lightweight aggregate concrete, more recently, millimeter and

micrometer size lightweight functional fillers (LWFs) including expanded polystyrene beads, expandable thermoplastic microspheres [61], hollow glass microspheres [35–37], and fly-ash cenospheres [47,62–64] have been exploited to produce high performance LWCC for structural application in buildings. This research demonstrates lightweight concrete that achieve the main goal while also trying to maintain performance levels for load bearing applications.

One of the prominent advantages of including micro-sized functional fillers into cementitious composites is its lightweight. To this end, Fly-ash cenospheres, micro-size hollow expandable thermoplastic microspheres, hollow glass microsphere (HGM), and EPS beads were used in cementitious composites. Fly-ash cenospheres, or FACs, are an alumino-silicate based by-product of coal combustion at thermal power plants [65]. The coal burning process in the thermal power plants produces fly ash in both solid and hollow (cenosphere) particulate forms. Most cenosphere particles have spherical shape and hollow interior covered by a thin shell with typical shell thickness of about 5-15% of its diameter. Due to its hollow structure, FAC have low particle density (400-900 kg/m^3) and low thermal conductivity. Xi et al [66] and Hanif et al [64] both evaluated FAC performance when nano silica is present. Compressive strength and microstructural evaluations were carried out by both with Xi also evaluating tensile properties. Both studies drew similar conclusions that the inclusion of FAC and nano silica resulted in lower amounts of calcium hydroxide and higher levels of CSH gel leading to better bonding of the FAC to the cement paste. Extensive mechanical testing was carried out by Chen et al [] to evaluate compressive strength, bending properties, fracture toughness, tensile ductility, and shrinkage strain. Microstructural and environmental analyses were carried out as well, but no thermal property evaluation was performed. The composition of FAC is mostly compatible with

cementitious binders. Due to its partial pozzolanic reactivity, together with the rougher surface of FAC, it provides good interfacial bonding within the mortar system.

In addition, Aglan et al. [61] incorporated micro-size hollow expandable thermoplastic microspheres (ETM) with average particle size around 35-55 micrometer into cement paste. Their study showed improvements in tensile strength and fracture toughness for cement pastes having 0.1 – 0.4 wt. % of ETM.

Expanded polystyrene (EPS) beads are artificial ultra-lightweight aggregate (typical density < 30 kg/m^3 [67]) with rounded shape and smooth surface. Earlier research on expanded polystyrene (EPS) concrete incorporates millimeter-size EPS spheres into mortar or cement paste to reduce density and thermal conductivity [67]. In comparison to regular lightweight aggregate concrete (LWAC), EPS concrete has shown better workability and volume stability [68]. It has been used for the fabrication of lightweight concrete bricks [69] and even load-bearing structural components [70].

Many researches have been performed on the mechanical properties of lightweight engineered cementitious composites containing glass microspheres. Wang et al. [71], and Al-Gemeel et al. [72] both used HGMs as a replacement of fly ash and/or cement. Both projects reported a decrease in the compressive strength of the LWCC that were tested, however neither project addresses the question if the strength lose is due solely to the added HGM or if the decreased pozzolanic material contributes to that decrease. Both performed flexural testing as well, with Wang et al. showing that the flexural strength is a function of both HGM type as well as percentage inclusion, while the effects of the HGM from Al-Gemeel et al. is unclear as fiber testing was being performed. In addition, the spherical shape and smooth surface of HGM can be

utilized to alter the rheological property of fresh cement mortar, which has led to their applications in oil well cement slurry [73].

1.2.2 Lightweight functional cementitious composites for increased thermal insulation.

A significant portion of energy is consumed every year by the building sector. According to a 2015 DOE report [74], 35% of energy was consumed by buildings. Though this is an improvement from a similar 2009 DOE report where 39% [75] was consumed, the building envelope is still a major area for saving the energy consumption of buildings. Building envelopes separate the outdoor environment from the controlled indoor environment and ensure indoor thermal comfort, and it mainly includes exterior walls and fenestrations. Therefore, the improvement of the thermal properties of the exterior walls are desired. For wall sections, there are four major categories: (1) lightweight insulative walls, (2) ventilated (double skinned) walls, (3) walls with latent heat storage capacity, and (4) and active building envelopes.

For cementitious composites, lightweight also usually indicates a decrease in thermal conductivity. Though the use of lightweight insulative concrete (LIC) is not going to be able to replace existing rigid and spray foam insulations they can be leveraged to improve existing systems. By using LIC that can withstand structural loads thermal bridging effects can be reduced increasing overall U-values of building façades. Real et.al. showed that the use of LIC reduced the overall U-values by as much as 20% depending on the specific concrete mixture [45].

FAC have been extensively studied to create cementitious composites that have low thermal conductivities. Huang et al. [47], Wu et al. [62], and Rheinheimer et al. [76] all tested and reported mechanical and thermal conductivity results for lightweight cementitious composites containing FAC with all reporting decreased strength and thermal conductivity.

Huang et al. and Rheinheimer et al. tested multiple inclusion percentages but did not evaluate the effect of different types of FAC, while Wu et al. tested one FAC type thoroughly and a second type simply, i.e., two of the twelve mixes with FAC. Huang evaluated the effect of replacing fine aggregates (iron ore tailing) with FAC at different percentages, while Wu et al. did not explore the relationship between FACs when other aggregates are present.

Thermally insulated building envelopes has also gained attention. Priyanka et al. [77] evaluated the effect of EPS beads on the thermal performance of foamed concrete wall panels. Three different volume fractions of EPS beads were added. For thermal testing, the panels were placed in a guarded hot plate apparatus and the heat flow was recorded. Panels were also tested mechanically in bending. The addition of the EPS beads resulted in a decrease in thermal conductivity of 31% but also a decrease in bending strength of 47%. This testing demonstrates the tradeoff that is generally required when decreasing density to maximize thermal insulation of a sample. Cavalline et.al demonstrated with both lab scale and through modeling that the use of LIC can reduce overall energy savings in a range of 0.2%-6.4% depending on the amount of normal weight aggregate replaced by lightweight aggregate [78]. This study plans to build on these finding to develop LIC with the use of micro-sized functional additives by themselves or along with lightweight aggregates.

1.2.3 Thermal energy storage

Phase change material (PCM) (e.g., paraffin wax) can be incorporated into cement-based materials through direct immersion [79,80], form-stable composite PCM [40–42], and encapsulation [53,81–84]. The direct immersion method directly immerse construction elements (e.g., concrete blocks) into liquid PCM and absorbs the PCM by capillary action [80]. Even though it can be easily incorporated into cement-based materials and can be implemented at a

low cost, this method suffers from the drawbacks of poor stability of the PCM and deterioration of mechanical and thermal properties caused by the direct contact of paraffin wax with the highly alkaline cementitious environment [85]. The form-stable composite PCM method first absorbs liquid PCMs into lightweight porous media, e.g., pumice and expanded shale/clay aggregates; and then, the PCM filled porous materials are mixed into cementitious composites [42]. This allows the PCM to be incorporated into construction materials at higher volume fraction. But this method raises the issue of leakage of the PCM from the porous media, both during mixing and after curing. The leaked PCM in contact with the cementitious binder may interfere with the hydration reactions [86–88] and affect the mechanical and durability properties of concrete elements; it may also cause the corrosion of reinforcing steel (especially for inorganic salt hydrates) that adversely affects the service life of the concrete structure [89].

To overcome these deficiencies, macro- and micro- encapsulation methods have been widely adopted and studied [53,81–84]. The main difference between macro-encapsulation and micro-encapsulation lies in the size and shape of shells. Macro-encapsulation usually has a shell size with diameter larger than 1 mm or 1 cm [83], whilst micro-encapsulation is usually 1-300 μm in size [57]. The macro-encapsulation method stores PCM into a relatively larger container (e.g., tubes [90], spheres [91]). It permits a high encapsulation ratio of PCM and a high content fraction of PCM incorporated into cement-based material. However, macro-encapsulation suffers from the drawbacks of leakage issues, poor heat transfer characteristics and thermal stratification [92]; and specific latent heat devices or heat exchanger surfaces are needed which increases the thermal resistance between PCM and environment [57]. Therefore, the micro-encapsulation method, as a potential solution to macro-encapsulation shortcomings, has attracted great research interest during the last two decades. Due to its smaller size compared with macro-encapsulation,

micro-encapsulation phase change material (MEPCM) has the advantages of good control of volume change when phase change occurs; easily incorporated into conventional building materials; and enhanced conductive heat transfer between PCM and the surrounding material [92]. The most commonly used encapsulating medium are polymer shells that can be physically or chemically created, generally controlled by the desired particle size (i.e. microcapsules smaller than 100μm cannot be created using physical methods) [81] . While polymer-based encapsulation is widely studied, it may be associated with very high production costs. It also suffers drawbacks including [57]: (1) its low mechanical stiffness and strength which leads to a significant reduction of mechanical performance for construction materials including concrete [93,94]; (2) leakage of PCM during mixing of concrete due to its low mechanically performing shell; and (3) poor thermal conduction performance due to the low thermal conductivity of polymer material.

Micro-encapsulation phase change material (MEPCM) has the advantages of good control of volume change when phase change occurs; easily incorporated into conventional building materials; and enhanced conductive heat transfer between PCM and the surrounding material [92]. Djamai et al. [95] performed a series of tests that included thermophysical analysis, microstructural analysis, and mechanical performance in compression. The reported findings demonstrate that the mechanical strength lose is not only due to the weak material properties of the polymer shell, but also due to a loss of hydration due to the MEPCM creating barriers between the water and the cement particles. They also reported the formation of macro voids created by the agglomeration of MEPCM particles in the matrix.; (2) leakage of PCM during mixing of concrete due to its low mechanically performing shell; and (3) poor thermal conduction performance due to the low thermal conductivity of polymer material. Hunger et al.

[96] evaluated both mechanical properties and thermal properties of cementitious composites containing MEPCM. There was agreement with Djamai et al. [95] that there was an increase in the porosity of the composite with increased volume loadings; however, the authors evaluated this as a positive side-effect due to it creating a mortar insulative material for energy savings since the compressive strengths that were achieved were very acceptable. It should be noted that the authors stated the MEPCM had no effect on the fresh properties of the mixtures, but that water was increased as MEPCM was increased in the mixture, which lead to a notable change in the fresh properties. In the review papers by Konuklu et al. [53] and Drissi et al. [81] both demonstrated that the inclusion of MEPCM into cementitious materials results in a decrease in mechanical strength and thermal conductivity, while increasing thermal heat storage. These two major draw backs are partially addressed by Liu et al. [57] by combining PCM with fly ash cenosphere micro-encapsulation. First the FAC are acid etched then the liquid PCM is infused into them through vacuum pressure. Once this is done the FAC MEPCM is allowed to cool and then washed to remove residue. When included into cement mortar at 3% weight of PCM the strength lose was only 5.6%. the FAC have an alumino-silicate based shell which has a higher thermal conductivity than that of the common polymer shell, this allows for more effective heat transfer into the PCM itself.

The use of phase change materials has been studied in building envelopes. Cabeza et al. [97] tested two concrete cubicles that were fully exposed to the climate of Spain. One cubicle contained 5% PCM by weight and the other another one was used as a reference concrete structure. They explored the effects of PCM on the indoor temperature in three different settings of fenestrations, i.e., closed windows, open windows, and windows open at day and closed during the night. The results show that the peak temperature was decreased by 2 degrees and the

time was shifted by 2 hours in the first case, whilst the effect of PCM was not obvious for the cases of opening windows. This was mainly due to the freezing thermal inertia being less obvious in the open window cases. Hunger et.al. used microencapsulated PCM in self-consolidating concrete and showed that energy savings of up to 12% can be achieved with the incorporation of 5% PCM into the mix [96]. They go on to explain draw backs of the micro-encapsulation method that is used in the experiment on the strength of the resulting concrete, i.e., about 3% inclusion it becomes too weak for a structural application. Gencel et. al. used shape stabilized PCM inside rice hull ash at a 50% aggregate volume replacement to develop a PCM mortar [98]. Based on small scale experimental tests on small box "rooms" it was estimated that a 3m x 4x 0.2m wall made from the developed PCM mortar would result in 14.3 kWh per day.

Further it has been shown that the passive use of active charging/discharging of PCM inside building materials can increase the effectiveness of the PCM and broaden the range at which they are applicable. Rucevskis et. al. showed that there was an average decrease of 6.8℃ decrease in room temperature, with a maximum of 10.5℃, when using an active thermal energy storage system over a passive system [99].

1.2.4 Cementitious composites for additive construction (3D printing)

3D concrete printing has been advanced as a feasible means for both precast and in-situ constructions due to the recent break throughs of contour crafting [93] and the development of D shape printing [94]. Over the last decade, the addition of functional additives into cementitious composites has gained increased attention and is well developed in standard cast concrete; however, it has not yet been fully applied to 3D printing. The hydration kinetics, rheology, and structuration rate are well studied [95,96] which provides the basis for the addition of functional additives into a 3D printing mixture.

In recent years, the ways to create resource efficient construction processes have increased such as the “resource efficient Europe” project [97]. One of the goals of this project was to decrease the weight of 3D printed cementitious composites. This was achieved by mixing aluminum powder and lime to create hydrogen gas within the mixture [98], by dispensing aluminum solution to create specific hole patterns [99], and by other topological optimization techniques [100]. Alternatively, the use of functional fillers, such as FACs, also can achieve this goal, possibly even more efficiently, since FAC are a biproduct of the coal industry. The use of FAC in 3D printing applications would achieve not only the resource efficient goal but also remove the storage requirement for an industrial waste product. Researchers at Oak Ridge National Laboratory [101] conducted experiments to study the effect of the including FACs in a 3D printed mortar. They concluded that not only did the resulting mortar have satisfactory strength development, but it also improved the overall printability of the mixture. Compared with a pure sand mixture, it reduces the mixing water requirement, increases plasticity, lowers extrusion force, and improves surface finish. Lu et. al. [102] developed a mixture proportion for spray-based 3D printing of cementitious composites using cenospheres and an air entraining agent for optimum delivery and deposition of the material. This 3D printing method is introduced to give large degrees of freedom for vertical and overhead construction. Their findings show that the inclusion of both cenospheres and air entrainer was able to lower the slump and spread diameter of the material, which allows the materials to retain its shape better during the printing process. The authors concluded that the 100% replacement of sand with FAC and a dosage of 0.1g/L of air entrainer was the optimum mixture design for rheological and deposition properties.

Further research has been expanded into the development of 3D printed cementitious composites containing MEPCM materials for thermal energy storage. Kurt et al. [103] demonstrated the feasibility of incorporating MEPCM material into 3D printed cementitious materials at a volume fraction of 2%. This inclusion resulted in a 30% decrease in the compressive strength of the material and a 9% decrease in flexural capacity at 7 days. The inclusion of 2% MEPCM, however, did not change the printability of the material.

Chapter 2. Problem statement and Research objective

2.1 Problem Statement

Despite the individual researches that have been conducted for each type of the aforementioned functional aggregates/ filler materials, there still lacks a comprehensive investigation on the mechanical and thermal performance of cementitious composites containing these emerging micro-sized functional fillers/ additives. Unlike most lightweight coarse aggregates with irregular shape and porous surfaces (e.g., expanded shale clay), the lightweight particulate aggregates/ fillers discussed in this paper have much smaller particle size and are mostly spherical in shape (or have a core-shell configuration). This will allow the fine-tuning of material properties by varying material parameters of the filler particles such as particle size, shell thickness (stiffness), and volume fraction.

The thermal and mechanical properties of functional cementitious composites depend largely on their hierarchical microstructure [100], see Figure 1. At dimensional scale of sub-micron to a few microns, a single CSP is typically comprised of a functional core (air, PCM, or other functional agents) and a soft (e.g., polymers) or rigid (e.g., glass or ceramic) shell interacting with the surrounding cementitious matrix. Since most CSP shells are not reactive to cement, an interfacial transition zone (ITZ) is developed between the surface of CSP inclusions and the cementitious matrix [101]. The ITZ within cementitious composites containing micro-sized CSP inclusions may have substantial accumulative impacts on the material's thermal and mechanical properties – i.e., due to the small particle size of most micro-CSP inclusions, their total surface area is typically large; secondly, the thickness of ITZ around micro-size inclusions may be comparable to their particle size, although few study has been conducted for micron- and

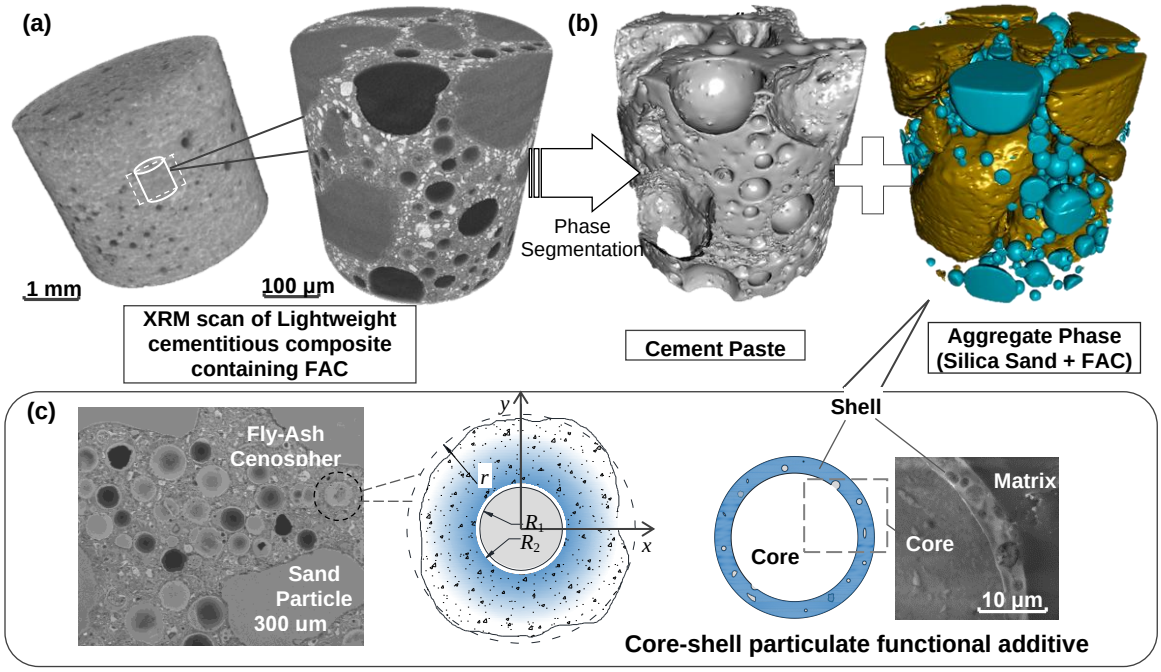

Figure 1: The hierarchical microstructure of lightweight cementitious composite materials containing fly-ash cenosphere (FAC) fillers
(a) X-ray micro-tomography (XRM); (b) 3D reconstruction of the cementitious matrix and aggregate phases; and (c) Scanning electron microscopy (SEM) images showing the embedded FAC and its hollow interior

sub-micron size inclusions [56]. At mesoscale (i.e., dimension from a few hundred microns to millimeters range), the entrapped air bubbles, fine and coarse aggregates are incorporated as if the cementitious matrix containing micro-CSP is a homogenized medium [100]. The homogenized mechanical (elastic) and thermal properties of cementitious composites are dictated largely on the properties of both the inclusion phases (i.e., functionally fillers and aggregates) – including its particle size distribution, shell property (soft vs. rigid shell) and its thickness, the binder (cementitious matrix) phase, as well as interaction among them (i.e., the ITZ). Figure 2 shows the interactions between MSFA, material properties, and the tunability for specific applications of cementitious composites containing MSFA.

In addition, there is a lack of understanding how micro-size functional fillers interacts will other phases in concrete such as aggregates (i.e., both fine and coarse aggregates), which may fundamentally influence both fresh and hardened properties of the final composite materials. Lastly, there is very little (almost none) studies on the behavior – both structurally and thermally, of building components constructed from these categories of materials, despite the quickly increasing research at material level.

2.2 Research objectives

The overarching goal of this research is to study the synergistic role of micro-size functional additives (MSFA) in developing functional cementitious composites that can be used in buildings to enable structural and architectural functionalities that make buildings more energy-efficient, resilient, and agile to the changing environment. Specifically, the effects of MSFA on the mechanical and thermophysical properties of cementitious composites are comprehensively studied in relation to the properties of the MSFA inclusion phase including particle-size, shell properties and material, as well as its interaction with other material phases including

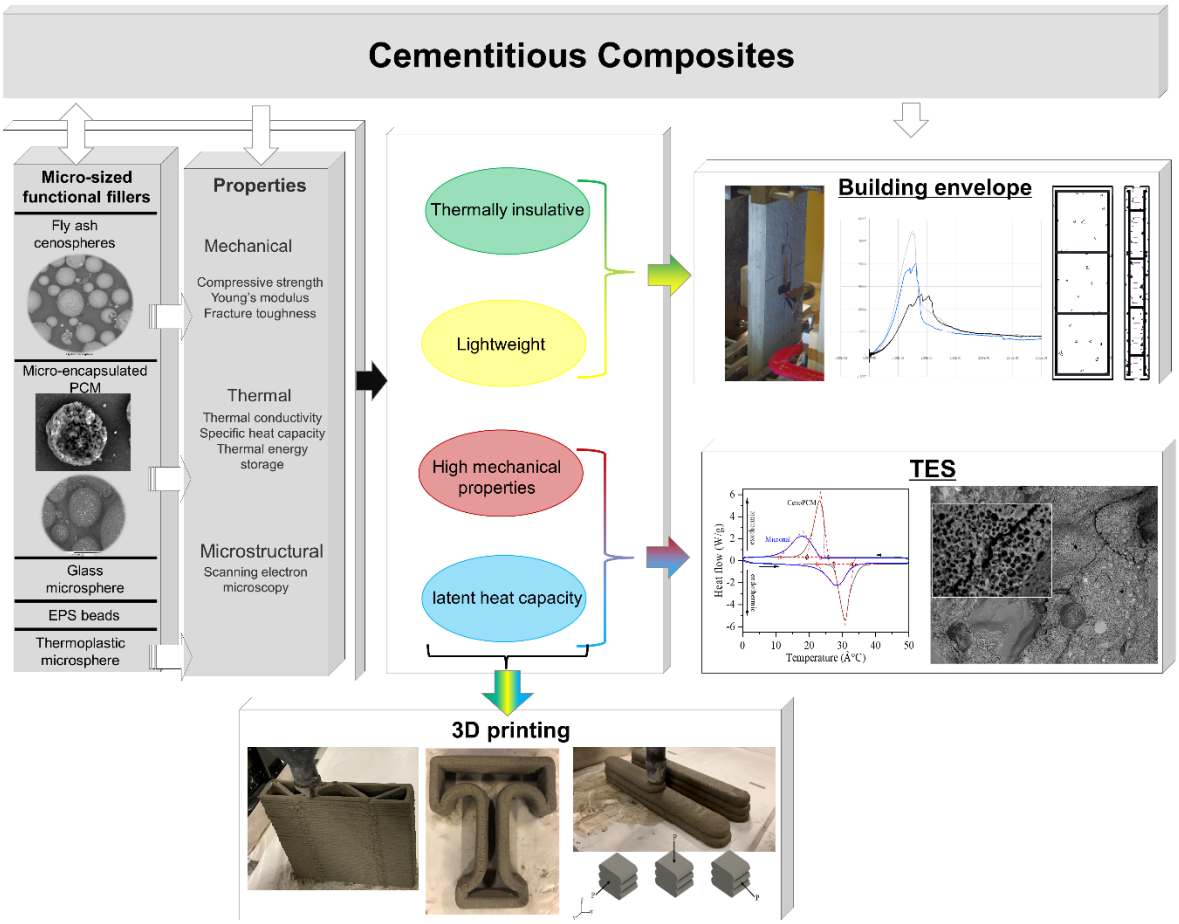

Figure 2: Interactions between MSFA, material properties, and structural and building application.

cementitious binder phase and aggregates. The scalability of functional cementitious composite containing micro-sized fillers towards the construction of building components is studied through component level prototyping and testing. In addition, functional cementitious composites will also be explored to facilitate emerging construction techniques including additive construction (concrete 3D printing).

Specific research objectives of this dissertation include:

1) Perform a comprehensive evaluation on the thermal and mechanical properties of cementitious composite materials with various types of micro-sized functional inclusions fillers. The influence of particle properties (i.e., particle size distribution, shell stiffness and thickness), volume loading, and distribution on the microstructure (as it relates to engineering properties), material properties, and functional performance of cementitious composites will be elucidated.
2) Investigate the interaction between micro-size functional particulate inclusions with the other phases within cementitious composites (i.e., cement-based binders with various water/cement ratio and mineral additives, and both normal and lightweight aggregates).
3) Establish the linkage of the properties defined at the material scale to the behavior of structural components and systems through scaled building component prototyping and testing.
4) Experimentally study the thermal performance and energy-saving potential of building envelope components constructed from functional cementitious composites.
5) Explore cementitious composites as a feasible and high-performance pathway to enable future additive construction (3D printing).

The organization of the dissertation will be as follows: Chapter 1 presents the background and literature review which discusses the current state of existing research; Chapter 2 contains the problem statement description and the specific research objectives of this dissertation; Chapter 3 presents the results of two studies on the mechanical and thermal performance of cementitious composites containing MSFA. Specifically, it explores the effect of particle size and volume fraction of CSP for lightweight and thermally insulative cementitious composites, and further studies the performance of MEPCM CSP with both soft and rigid shell materials; Chapter 4 explores the relationship between the inclusion of MSFA with different binder matrixes (cement, cement + silica fume, cement + silica fume+ steel fibers)and in the presence of different types of aggregate (normal weight and lightweight), mechanical and thermal tests were performed; Chapter 5 presents the results of scaled down concrete sandwich panels tested on a small scale guarded hot bow as well as in compression to evaluate the effect of MSFA on building envelope performance; Chapter 6 explores the effect that MSFA have on the workability, printability, constructability, mechanical and thermal properties of 3D printed cementitious composites to evaluate the feasibility of their use to maximize thermal energy storage possibilities; Chapter 7 discusses the conclusions of this dissertation.

Chapter 3. Cementitious composites containing functional micro-sized fillers

A version of this section was originally published by Adam Brooks, Hongyu Zhou, and Dominic Hanna:

Brooks, Adam & Zhou, Hongyu & Hanna, Dominic. (2018). *Comparative study of the mechanical and thermal properties of lightweight cementitious composites.* Construction and Building Materials. **159**. 316-328.

A version of this section was originally published by Adam Brooks, Yi Fang, Zhenglai Shen, Jilai Wang, and Hongyu Zhou:

Brooks, Adam & Fang, Yi & Shen, Zhenglai & Wang, Jialai & Zhou, Hongyu. (2021). Enabling high-strength cement-based materials for thermal energy storage via fly-ash cenosphere encapsulated phase change materials. Cement and Concrete Composites. 120. 104033.

3.1 Effects of micro-sized fillers on the mechanical and thermal performance of functional cementitious composites

In this section, a comparative study is conducted on the properties of lightweight cementitious composites (LWCCs) mixed with four types of lightweight aggregates/ filler particles – i.e., EPS beads, dry-expanded plastic microspheres, hollow glass microspheres, and fly ash cenospheres. The materials' thermophysical (e.g., density, thermal conductivity) and mechanical (compressive strength) properties are investigated with respect to the particle type, size distribution, as well as their volume concentration. Key parameters governing the material thermal and mechanical properties are discussed, and the composition-property relationships are deduced from both experiment results and predictive models. The results will provide valuable insights into the quantitative design of concrete and cementitious composites containing micrometer and millimeter size lightweight particle fillers.

3.1.1 Material preparation and mix design

The constituent materials used for preparing the lightweight and ultra-lightweight cementitious composites in this study include ASTM Type I-II Portland cement, silica sand (*US silica*), water, superplasticizer (*Sika Corp.*), and lightweight fillers (LWF). The water to cement

ratio (w/c) was selected at 0.43 for all mixtures. The mass of cement, sand, and water used for each cubic meter of the reference mortar (without LWF) are 530.64 kg/m^3, 1367.67 kg/m^3, and 228.18 kg/m^3, respectively. The LWF used in this research include expanded polystyrene (EPS) beads, expanded thermoplastic microsphere (ETM), hollow glass microspheres (HGM), and fly ash cenospheres (FAC). For each type of LWF, different particle properties (i.e., size, density, crushing strength, and volume fraction etc.) were studied with respect to their influences on the mechanical and thermophysical properties of LWCC. For each group of LWF tested herein, four LWF volume fractions (v_f) – i.e., namely 7%, 14%, 21%, and 28% of the total volume were tested and for each volume fraction the equivalent volume of regular fine aggregate (i.e., silica sand) was deducted from the mix (i.e., the amount of silica sand used for v_f = 7%, 14%, 21%, and 28% are 1138.37 kg/m^3, 937.38 kg/m^3, 715.83 kg/m^3, and 533.71 kg/m^3, respectively). The air content of fresh cement mortar was measured at 2-5% according to ASTM C185 – 15a, which does not account for the air contained within the LWF. The properties of lightweight micro-fillers (LWF) used in this research are listed in Table 1 and are briefly introduced as follows.

EPS beads and ETM

Two types of EPS beads with average particle size of 2.5 mm (noted as "medium") and 1 mm (noted as "small") are used in this research. The particle size of EPS beads was analyzed using an air jet sieve. The densities of medium and small EPS beads were tested at 0.013 g/cm^3 and 0.031 g/cm^3, respectively. The thermoplastic microspheres are produced by *AkzoNobel* (*Expancel*^{TM} 461 DET 40 d25) with average particle size of 35-55 μm as reported by the manufacturer's material datasheet [102]. The density of ETM particles were tested at 0.025 g/cm^3 by gas pycnometry.

Table 1. Properties of the lightweight particle filler (LWF) materials used in this research

Group ID#	Material	Particle Size (μm)*			Wall Thickness - t (μm)**	t/D_{50}	Density (g/cm^3)	Crush Strength (MPa)***
		D_{10}	D_{50}	D_{90}				
EPS-M	EPS beads (2.5mm)	--	250	--	--	--	0.013	--
EPS-S	EPS beads (1mm)	--	100	--	--	--	0.031	--
TPMS	Thermoplastic microsphere	--	35-55	--	--	--	0.025	--
HGM K25	Hollow glass microsphere (HGM)	25	55	90	0.85	0.015	0.25	0.75
HGM S32		20	40	70	0.88	0.022	0.32	2
HGM S38HS		19	44	70	1.20	0.027	0.28	5.5
HGM H50		15	35	50	1.70	0.049	0.50	10
HGM S60		12	29	48	1.49	0.051	0.60	10
FAC E106	Fly ash cenosphere (FAC)	42.6	81.3	125.2	4.8	0.059	0.91	1.6-3.2
FAC E160		44.9	90.6	155.4	6.0	0.066	0.76	1.6-3.2
FAC E200/600		81.3	349.1	457.2	16.5	0.047	0.82	1.6-3.2

* Particle size data for the thermoplastic microspheres and hollow glass microspheres (HGM) were reported by the manufacturer. The particle size of FACs was tested using laser diffraction and those of EPS beads were analyzed using an air jet sieve.

** The wall thickness of LWF was tested using SEM microcopy where the particles are dispersed within an epoxy matrix. Then the samples were grinded and polished to expose the section of shell.

*** The crush strength was determined using an isostatic method for the tested bubbles to have 90% survival rate.

Glass microsphere bubbles

Five types of hollow glass microsphere (HGM) bubbles with density ranging from 0.25 g/cm^3 to 0.6 g/cm^3 were used for the mixes. The HGMs used in this research are produced by 3M^{TM} . The average particle densities tested by gas pycnometry for HGM K25, S32, S38HS, H50, and S60 are 0.25 g/cm^3, 0.32 g/cm^3, 0.38 g/cm^3, 0.50 g/cm^3, and 0.60 g/cm^3, respectively. The microspheres also have different particle size (in descending order), wall thickness, and isostatic crush strength as listed in Table 1. The particle sizes were tested by laser diffraction and reported by the manufacture. The isostatic crush strength refers to the pressure at which an average lot of material has 90% or higher survival [103]. The HGM H50 bubbles also have a layer of saline-epoxy coating to enhance the interfacial bonding between the glass microsphere and the cementitious matrix.

Fly-ash cenospheres (*FAC*)

Three types of cenospheres (*CenoStar*) with particle sizes up to 106 μm (E106), 160 μm (E160), and 600 μm (E200/600) are studied in this research. X-ray Diffraction (XRD) analysis performed on the FACs (Figure 3 (a)) indicated that the cenospheres are comprised primarily of SiO_2 and Al_2O_3, and there is a large amount of amorphous materials with small amounts of mullite and calcite. The E200/600 also contains small amount of quartz (Figure 3 (a)). The particle size distributions were tested using a Laser Diffraction particle size analyzer (Horiba LA-950) and the results are plotted in Figure 3(b). The particle shell thicknesses were measured using scanning electron microscopy (SEM) imaging where the particles were embedded in epoxy and grinded using a Buehler EcoMet^{TM} grinder/polisher to expose the section of the FAC shell. Figure 3(c) presents the SEM images showing the surface morphologies of each type of FAC particles studied herein.

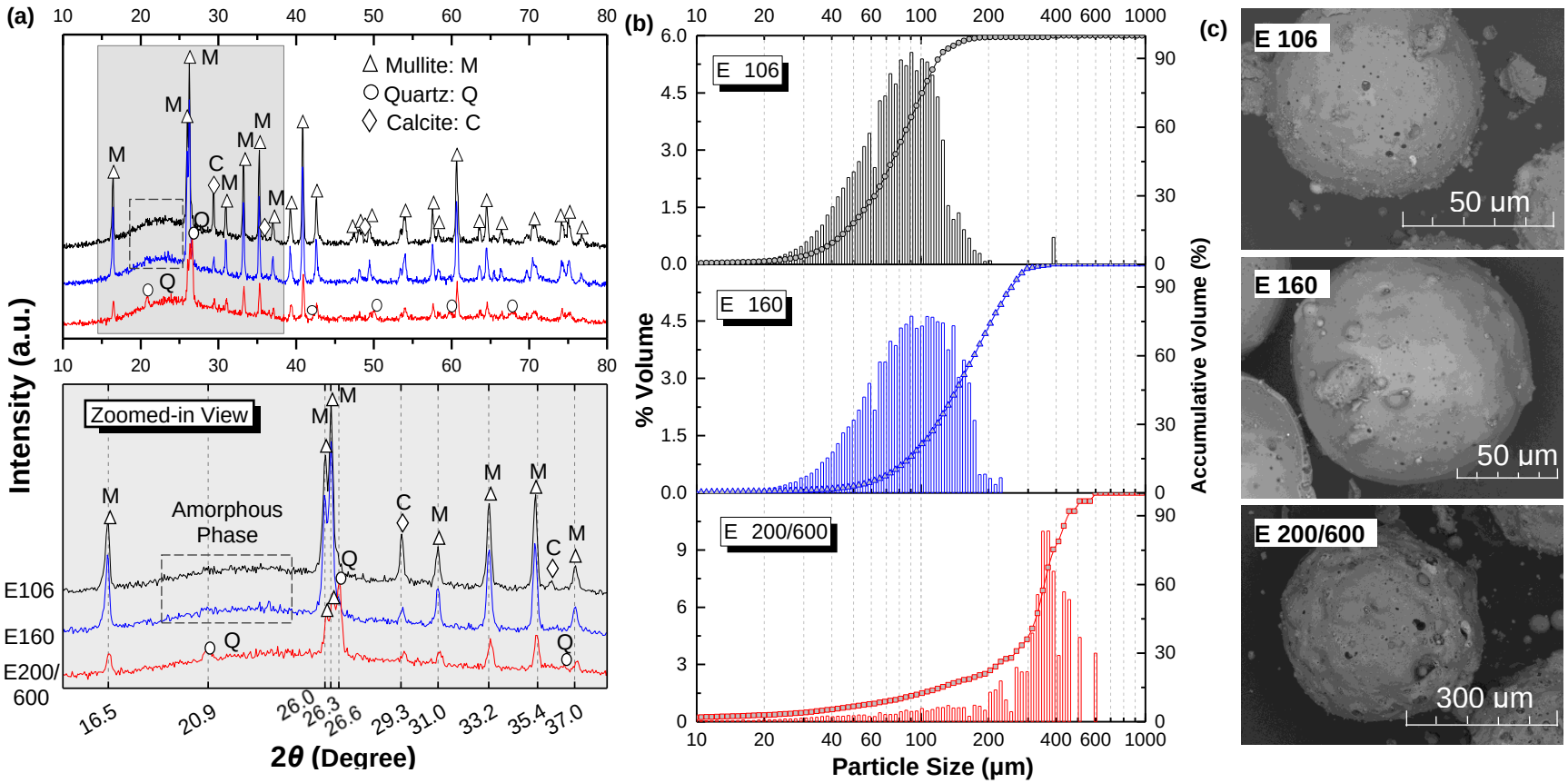

Figure 3: Characterization of fly ash cenospheres (FAC):
(a) XRD-analysis result and phase chart; (b) and particle size distribution of the fly-ash cenospheres (FAC), and (c) surface morphology of the FACs

For testing the mechanical and thermal property of LWCC, eleven (11) groups (a total of 55 mixtures) of mortar samples were tested. For each group, five 50mm (2-inch) by 100mm (4-inch) cylinders were made for compression tests and three 50mm×50mm×50mm cubic specimens were made for thermal property tests.

3.1.2 Thermal property test using Transient Plane Source (TPS) method

The thermal properties (i.e., thermal conductivity and volumetric heat capacity) of LWCCs were tested using the Transient Plant Source (TPS) method [104] (*HotDisk TPS-1500*). The TPS method uses a conducting pattern with negligible heat capacity acting simultaneously as the heating element and temperature sensor (e.g., the Kapton supported double spiraled nickel metal sensor as shown in Figure 4(a)). To solve for the thermal constants of the tested material, the hot disk sensor is assumed to consist of a series of concentric ring heat sources located in an infinitely large sample. When the double spiral sensor is electrically heated, its increase in resistance is measured as a function of time:

Equation 1:

$$R(t) = R_0\left[1+\Omega\left(\Delta T_i + \Delta T_{avg}(\tau)\right)\right]$$

where R_0 is the initial resistance of the sensor prior to the heating; Ω is the coefficient of resistivity; ΔT_i is a measure of the thermal contact between the sensor and the test sample, and it becomes a constant momentarily after the heating starts. The time-dependent temperature increase, $\Delta T_{avg}(\tau)$, is recorded and the thermal conductivity k and thermal diffusivity α of the tested material can be simultaneously obtained through a process of iteration. The TPS method provides a fast yet accurate method to measure thermal conductivity and thermal diffusivity of materials [105]. The test time for each measurement normally ranges from tens of seconds to several minutes, which is substantially shorter than those of steady-state test methods such as the

guarded hot box (GHB) tests [106]. The TPS method can also use different sensor sizes to accommodate different sample types. The optimal sample sizes are usually determined by the material homogeneity [105].

For the TPS tests, the LWCC cubes were cut into two identical halves (50×50×22mm), see Figure 4(b). Then, the samples were dried in a convection oven for 24 hours and cooled down to room temperature in an air-tight desiccant cabinet to prevent condensation. The TPS tests were then performed using a HotDisk TPS-1500 thermal constant analyzer according to the ISO22007-2 specifications [104]. The applicable thermal conductivity testing range of the equipment was 0.01-400 W/m K. Three repeated measurements were taken on each tested sample to ensure the consistency of the test results.

3.1.3 Mechanical testing

Mechanical properties of the LWCC mortar mixtures were tested using a MTS-810 servo-hydraulic universal testing system. The loading was carried out in a displacement-control mode at the loading rate of 0.01 mm/min. Five 50 mm diameter by 100 mm tall cylinders were tested for each mixture group. A high resolution CCD camera was staged to record the damage and failure of the specimens. The mechanical test setup is shown in Figure 5. The tested specimens were preserved for further morphological analysis.

3.1.4. Thermal test results

The experimental test results for density, thermal and mechanical properties of the lightweight cementitious composites (LWCC) are summarized in below. The density of LWCC mortar samples was determined under both wet and oven-dry conditions. The wet density of mortar mixes was measured immediately after the cylinders were made. The oven dry density of

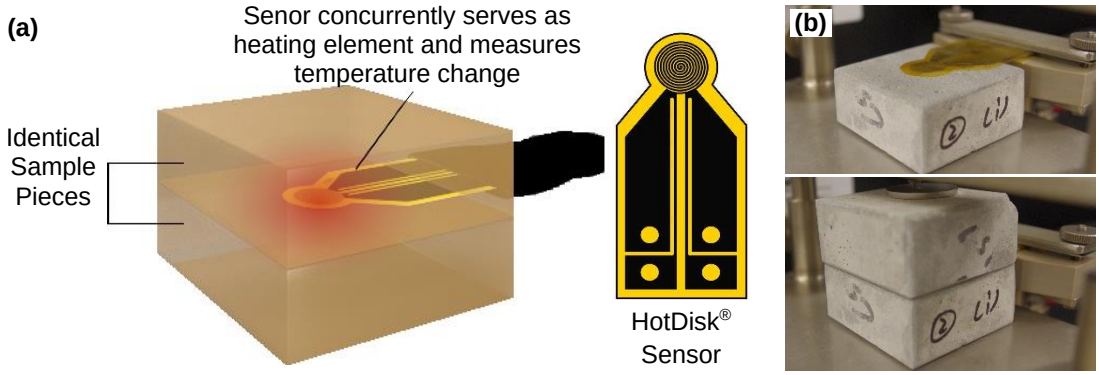

Figure 4: The Transient Plane Source (TPS) tests for determining thermal properties: (a) illustrative of the test setup; (b) pictures showing the LWCC being tested

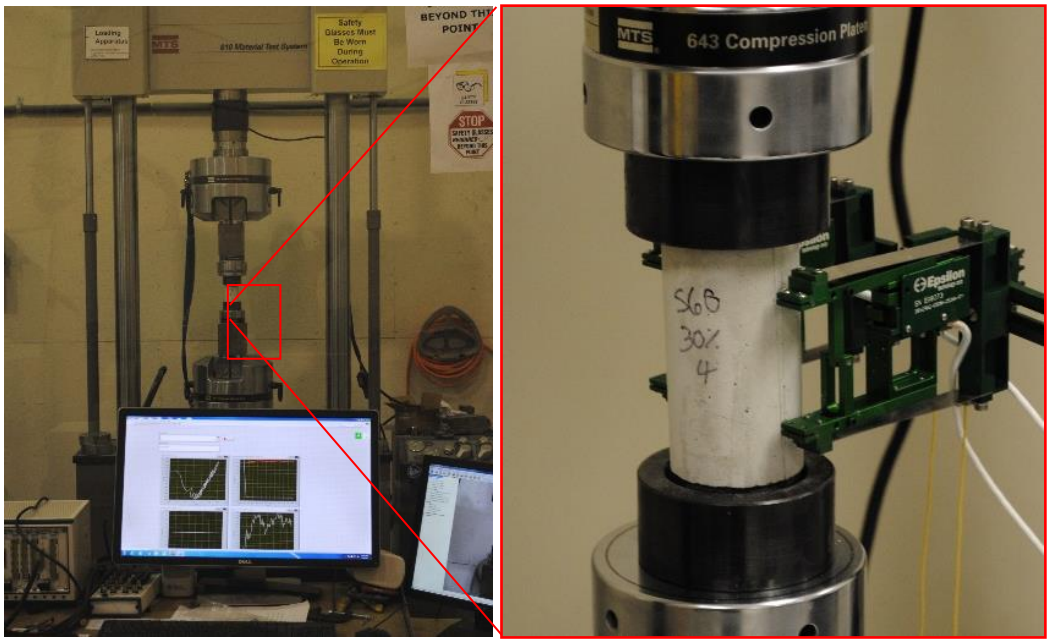

Figure 5: Picture showing the mechanical test setup.

LWCC was measured after 28 days curing and the samples were dried in a convection oven at 110℃ for 48 hours. The oven dry density of the LWCC mixtures in this research ranges from 1300 kg/m3 to 1940 kg/m3 depending on the volume fraction and type of lightweight micro-filler aggregates used. The highest LWF volume fraction tested was about 28% with realistic consideration of the material costs.

In general, the thermal conductivity of LWCC mortar decreases with the increase in LWF volume fraction v_f. For the control mortar samples (without LWF), the thermal conductivity was tested between 2.1-2.2 W/m K. The thermal conductivities of LWCCs are significantly lower than that of normal weight cement mortar and concrete due to the incorporation of hollow (or porous) lightweight particulate fillers. It should be mentioned that since the LWFs were used to replace the regular fine aggregate (i.e., silica sand) by its equivalent volume. The decrease in thermal conductivity is partially attributed to two factors: (1) the inclusion of low conductivity LWFs in cement paste, and (2) the decreased volume fraction of silica sand (i.e., silica sand, which is primarily quartz, has substantially higher thermal conductivity than cement paste. The thermal conductivity of cement paste at w/c = 0.43 was tested at 0.662 ±0.0081 W/m K by transient plane source (TPS) method.) The contributions from sand and the LWF to the overall thermal conductivity of the LWCC composite mortar will be quantitatively discussed in later sections of this paper.

It was observed that the thermal conductivity of LWCC is relatively insensitive to the type and size of LWF used; rather, it is primarily dictated by the LWF volume fraction, see Figure 6(a)-(c). As the LWF volume fraction v_f increases the equivalent thermal conductivity of

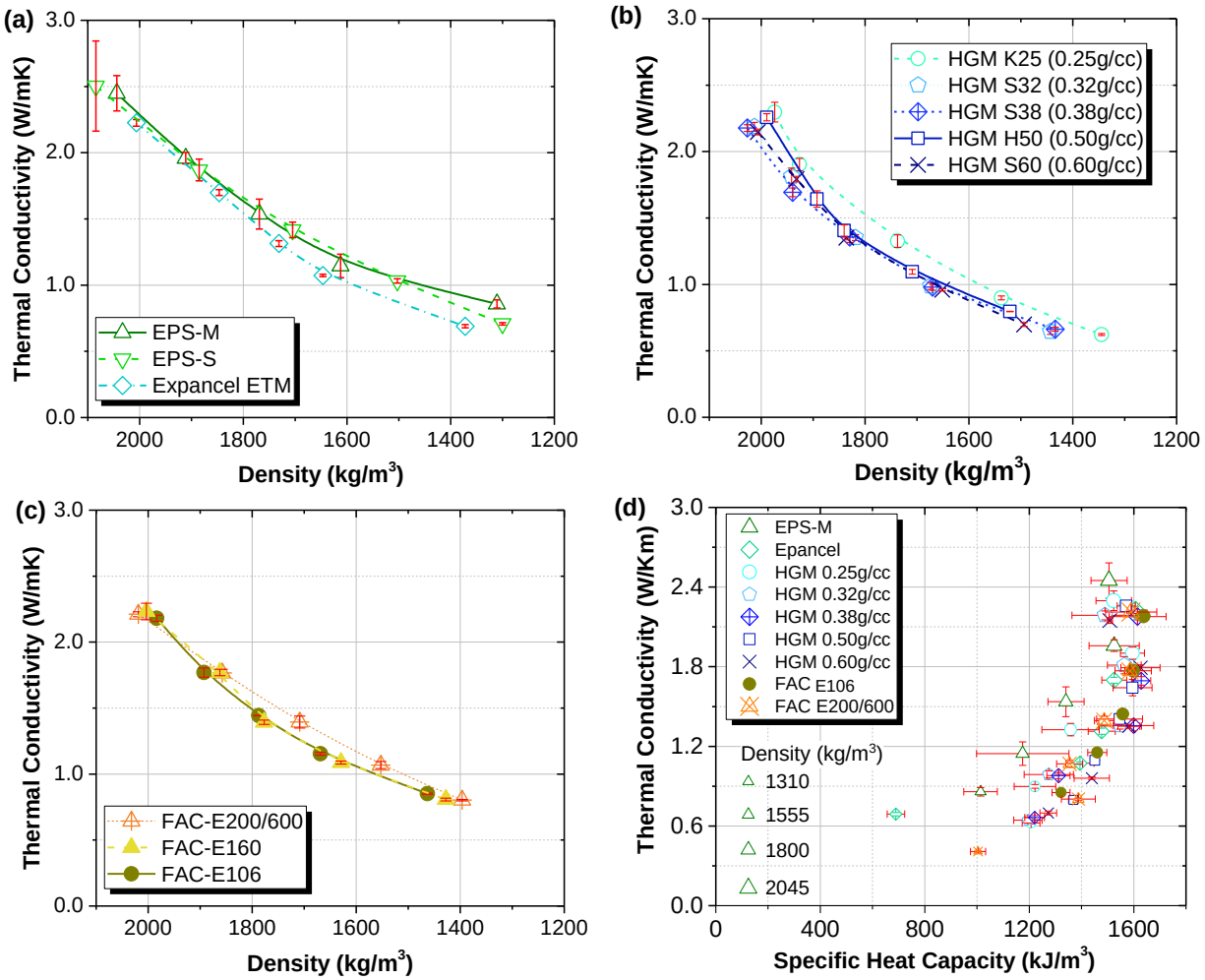

Figure 6: Thermal properties of LWCC tested through Transient Plane Source (TPS) method: (a) LWCC with EPS beads and expandable thermoplastic microspheres (ETM); (b) LWCC with hollow glass microspheres (HGM); (c) LWCC with fly ash cenospheres (FAC); and (d) thermal conductivity vs. volumetric specific heat capacity tested through TPS

LWCC mortar decreases notably, i.e., when 7%, the thermal conductivity reduces by about 30%; as approaches 28%, the thermal conductivity of LWCC decreases to 0.65-0.8 W/m K only 35% of the control mortar group. For the LWF materials studied herein – i.e., EPS beads/ETM, HGMs, and FAC, the particle size and shell property have very limited effects on the thermal conductivity of LWCC mortar. While LWCC containing larger particles (i.e., EPS-M, GHM K25, and FAC E200/600) has shown slightly higher thermal conductivity than other groups, see Figure 6(a)-(c). This is mainly due to the greater air cell size induced within the mortar system by the larger size particles – i.e., the convective heat transfer through air enclosed in the cells reduces as the pore size becomes smaller [107]. Through the TPS method, the volumetric heat capacity of LWCCs can also be calculated from the thermal conductivity and thermal diffusivity tested. Generally, the volumetric heat capacity (VHC) of LWCC decreases as ν_f increases and it ranges from 690 kJ/m^{3}K to 1680 kJ/m^3. The VHC is roughly proportional to the materials' dry density, see Figure 6 (d).

3.1.5 Compressive strength

Unlike thermal properties, the compressive strength of the LWCC depends largely on the type and size of LWF included. The average 28-day compressive strength of LWCC mixtures with different lightweight functional fillers and volume fractions (ν_f) are summarized in Figure 7, where the compressive strength is plotted against dry density of the materials. For LWCCs with EPS beads and expandable thermoplastic microspheres (ETM), the compressive strength decreases quickly as ν_f becomes higher, see Figure 7(a). The decrease in strength is primarily due to the introduction of the weak aggregate phase which promotes stress cracks to initiate and

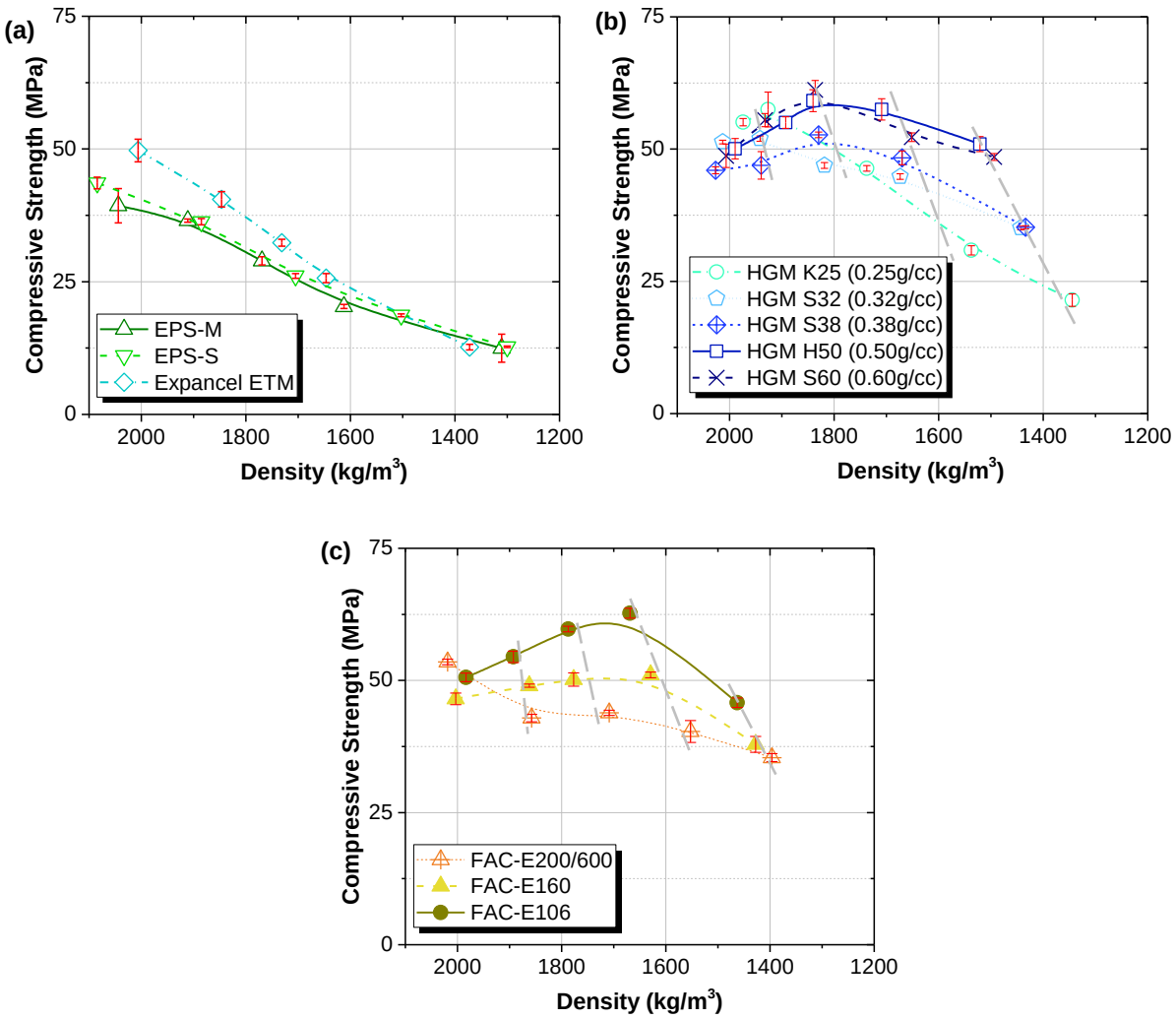

Figure 7: Compressive strength vs. dry density of LWCCs containing: (a) EPS beads and ETM; (b) hollow glass microspheres (HGM); and (c) fly-ash cenospheres (FAC)

propagate within the materials under mechanical loading. While previous studies by Roy et al. on EPS concrete [108] indicated that smaller particle size normally yields higher strength, the difference in compressive strength between two different size EPS mortar groups (i.e., 2.5 mm and 1 mm) is not noticeable, see Figure 7(a). However, it was observed that when ν_f is small the compressive strengths of LWCC mixtures with ETM are about 15% higher than those of their EPS counterpart. This is believed to be caused by the reduction of air content due to the inclusion of ETM particles.

The compressive strength of LWCC mortars containing HGM and FAC, on the other hand, depends highly on the particle size and shell property (e.g., thickness) of the LWF included. When ν_f is small (<15%), the compressive strength of LWCC mortars increases with higher HGM concentrations, see Figure 7 (b). This is believed to be due to the spherical shape of HGM, which improves the rheological property (i.e., flowability) of fresh mortar mixes and reduces the air content (Table 2). The compressive strength starts to decrease when the volume fraction of HGM becomes higher (> 15%) – i.e., the hollow structure of HGMs allows the stress cracks to propagate through the particle shell to cause damage and material failure. It is noted that with the same LWF volume concentration (or density), mortars having smaller size HGM particles and thicker shell yield higher mechanical strength, see Figure 7 (b). This trend becomes more notable when LWF volume fraction ν_f is high. At ν_f = 7%, the HGM S60 mortar is 32% (15 MPa) stronger than the mortar containing K25 particles; whereas at ν_f = 28%, S60 mortar is about 125% (27 MPa) stronger than the K25 mortar. It is worthwhile mentioning that the compressive strength of LWCC mortars mixed with nearly 30% (total volume fraction) of H50 and S60 HGM particles are almost the same as the reference mortar while their densities were

Table 2. Density, mechanical, and thermal properties of the tested mixture groups

Mix ID	LWMI Material Type	LWF Fraction	Air Content	Wet Density	Oven Dry Density	Compressive Strength	Thermal Conductivity	Volumetric Heat Capacity
		v_f (%)*	(%)**	(kg/m^3)	(kg/m^3)	(MPa)	(W m^{-1}K^{-1})	(KJ/m^3)***
EPS-M-0	EPS beads (2.5mm)	0	4.25	2351.61	2044.15	39.31	2.45	1505.2
EPS-M-1		6.75	-	2194.09	1911.09	36.51	1.96	1525.2
EPS-M-2		13.75	-	2041.36	1769.32	28.91	1.54	1340.7
EPS-M-3		21.00	-	1847.74	1612.15	20.32	1.15	1175
EPS-M-4		28.50	-	1498.13	1310.72	12.47	0.86	1013.6
EPS-S-0	EPS beads (1mm)	0	3.75	2343.11	2084.49	43.59	2.50	1472.4
EPS-S-1		6.75	-	2131.78	1885.19	36.29	1.87	1498.3
EPS-S-2		13.75	-	1922.17	1704.75	26.09	1.42	144369
EPS-S-3		21.00	-	1697.49	1502.72	18.67	1.03	1308.0
EPS-S-4		28.50	-	1486.55	1300.15	12.73	0.71	1146.2
TPMS-0	Thermoplastic microsphere (Expancel™)	0	4.25	2260.74	2006.28	49.71	2.23	834.1
TPMS-1		6.75	-	2142.79	1846.30	40.52	1.70	1525.1
TPMS-2		13.75	-	1995.89	1731.07	32.35	1.31	1477.3
TPMS-3		21.00	-	1960.71	1646.53	25.68	1.07	1394.2
TPMS-4		28.50	-	1609.34	1372.05	12.68	0.69	689.5
K25-0	Hollow glass microsphere (3M) K25	0	5	2277.64	1974.11	55.10	2.30	1523.4
K25-1		7.1	3	2235.54	1926.16	57.50	1.90	1595.2
K25-2		14.5	2	1984.32	1737.42	46.36	1.33	1358.2
K25-3		22.1	2.5	1737.39	1537.40	30.86	0.90	1222.1
K25-4		29.3	3.5	1588.65	1344.25	21.46	0.62	1207.3
S32-0	Hollow glass microsphere (3M) S32	0	4.5	2311.05	2013.08	51.33	2.19	1489.3
S32-1		6.87	2	2238.87	1941.67	51.98	1.81	1564.0
S32-2		13.92	2.25	2067.02	1818.62	46.91	1.35	1547.5
S32-3		21.51	1.75	1901.02	1673.73	44.80	0.99	1274.8
S32-4		28.82	2	1664.36	1442.62	35.09	0.64	1194.9
S38HS-0	Hollow glass microsphere (3M) S38HS	0	3.25	2297.85	2026.87	45.99	2.18	1614.8
S38HS-1		6.71	2.25	2218.99	1939.33	46.91	1.69	1628.6
S38HS-2		13.69	2	2058.28	1829.67	52.69	1.36	1599.3
S38HS-3		21.30	1	1871.48	1670.00	48.35	0.98	1311.7
S38HS-4		28.59	1.25	1654.59	1433.95	35.23	0.66	1220.7
H50-0	Hollow glass microsphere (3M) H50	0	4.25	2299.56	1989.22	50.07	2.26	1571.1
H50-1		5.61	2.25	2173.20	1892.79	55.02	1.62	1595.7
H50-2		11.65	1.75	2127.71	1840.53	59.14	1.41	1545.8
H50-3		18.14	2	1943.72	1709.03	57.50	1.09	1451.2
H50-4		24.73	2	1773.87	1521.09	50.94	0.80	1369.3
S60-0	Hollow glass microsphere (3M) S60	0	4.75	2297.53	2006.69	48.72	2.15	1508.6
S60-1		7.07	3.25	2208.98	1932.18	55.48	1.79	1625.8
S60-2		14.60	1.25	2088.87	1836.35	61.18	1.35	1581.2
S60-3		22.09	2.5	1903.32	1651.29	52.24	0.96	1439.4
S60-4		29.20	3.75	1697.20	1493.66	48.50	0.70	1272.8

Table 2 cont. Density, mechanical, and thermal properties of the tested mixture groups

Mix ID	LWMI Material Type	LWF Fraction	Air Content	Wet Density	Oven Dry Density	Compressive Strength	Thermal Conductivity	Volumetric Heat Capacity
		v_f (%)*	(%)**	(kg/m^3)	(kg/m^3)	(MPa)	(W m^{-1}K^{-1})	(KJ/m^3)***
E106-0	Fly-ash cenosphere E106	0	3.75	2288.17	1983.71	50.59	2.18	1638.0
E106-1		6.75	2.25	2178.57	1892.50	54.47	1.77	1597.9
E106-2		13.75	2.75	2054.27	1787.17	59.74	1.44	1557.9
E106-3		21.00	2.75	1910.69	1668.56	62.75	1.15	1460.4
E106-4		28.50	4.25	1705.88	1462.83	45.78	0.85	1321.7
E160-0	Fly-ash cenosphere E160	0	3.75	2296.20	2003.09	46.53	2.23	1648.4
E160-1		6.61	2.25	2145.89	1862.21	40.02	1.77	1444.2
E160-2		13.28	2.75	2039.50	1776.83	50.17	1.39	1519.9
E160-3		20.62	2.75	1870.99	1629.28	51.06	1.09	1420.9
E160-4		27.18	4.25	1656.77	1427.42	37.90	0.81	1188.9
E200/600-0	Fly-ash cenosphere E200/600	0	3.5	2333.19	2019.02	53.50	2.21	1590.0
E200/600-1		5.77	4.75	2160.37	1857.67	42.88	1.77	1585.4
E200/600-2		11.81	4.25	1991.62	1708.45	43.86	1.39	1486.9
E200/600-3		18.21	5.75	1840.96	1552.83	40.36	1.07	1354.3
E200/600-4		24.51	6	1654.94	1396.15	35.40	0.80	1387.9

***** The LWF volume fraction is calculated as the ratio between the volume occupied by LWF over the total volume;

****** The air content is measured on fresh LWCC mortars according to the ASTM 185 – 15c specifications;

******* The specific heat capacity is calculated based on the thermal diffusivity measured through the TPS method.

and S60 HGM particles are almost the same as the reference mortar while their densities were about 25% lower than the reference mortar, see Table 2 and Figure 7 (b). This provides significant potential for the design of high strength lightweight cementitious composites and concretes for structural applications.

A similar trend was observed for LWCCs containing FACs. Generally, LWCC containing larger FAC particles (i.e., E200/600) have lower strength for given FAC volume fraction (or density). For the LWCC group having E200/600 cenospheres, the compressive strength shows a continuously descending trend as ν_f becomes higher. For both E106 and E160, the mortar strength peaks at ν_f = 21% and it decreases rapidly (by about 25%) when ν_f approaches 28%. For LWCCs modified with E106 and E160 FAC, the compressive strength is similar or higher than the reference mortar when the ν_f is less than 20-25%, see Figure 7 (c). It is noted that the E200/600 mortars have higher air content than the other FAC groups (Table 2). This is likely due to the surface pores on the cenospheres (Figure 3 (c)) as well as the larger particles size that made the fresh mortar less flowable.

3.1.6 Microstructures and fracture topography

The microstructural characterization was carried out using scanning electron microscopic (SEM) imaging. The LWCC mortar samples for microstructural analysis were resin-impregnated using epoxy, and the resin mounted samples were then ground and polished using a Buehler EcoMet grinder/polisher to 0.3 μm diamond paste. Some polished samples were then carbon-coated to a thickness of approximately 10 nm to prevent charging under the electron beam. SEM imaging was conducted using a Hitachi TM1000 at accelerating voltage of 15 kV. For analyzing

the fracture surfaces of LWCC, fragments of the tested compression cylinders were preserved and placed on a sample holder for SEM imaging analysis.

Figure 8 presents the SEM micrographs of four different LWCCs having E 200/600, E160 FACs and K25, S60 HGMs as the lightweight filler. The volume fractions of LWF for the four LWCC groups presented in Figure 8 were nearly the same, i.e., approximately 14% of the total volume. It is noted that the E200/600 FAC have similar particle size with silica sand and the cenospheres were scattered across the mortar material (Figure 8 (a)). The shell thickness of E200/600 FAC is around 15 μm (5-10% of the particle diameter) and the shell has a microporous structure. On the other hand, the smaller FAC particles (E160) are well distributed within the cementitious binder, see Figure 8 (b). The denser, more compacted, and uniform microstructure in the E160 modified LWCC influenced its mechanical strength (Figure 7 (c)) and certain other properties of the composites including the post-crack behavior [48]. It was also observed in the experiments that the spherical shape and smooth surface of E106 and E160 FAC (see Figure 3 (c)) improved the rheological behavior of the fresh mortar mix and reduced the air content. The K25 and S60 HGMs have similar particle size as the E160 FAC and they were both well distributed within the cementitious binder. While the low density K25 particles have greater particle size and thinner shell wall than S60 (see Table 1 and Figure 8 (c) and (d)). It is evident that most of the K25 and S60 HGM particles survived the mortar mixing process and breakage of LWF particles during concrete mixing are minimal.

The fracture surfaces of the compressive cylinders used for the mechanical testing were also examined using SEM. Figure 9 presents the fracture topographical images of six different LWCC mixtures including EPS-small, expandable thermoplastic microsphere (ETM), FAC200/600, FAC160, HGM K25 and HGM K60. It is evident that the damage modes of

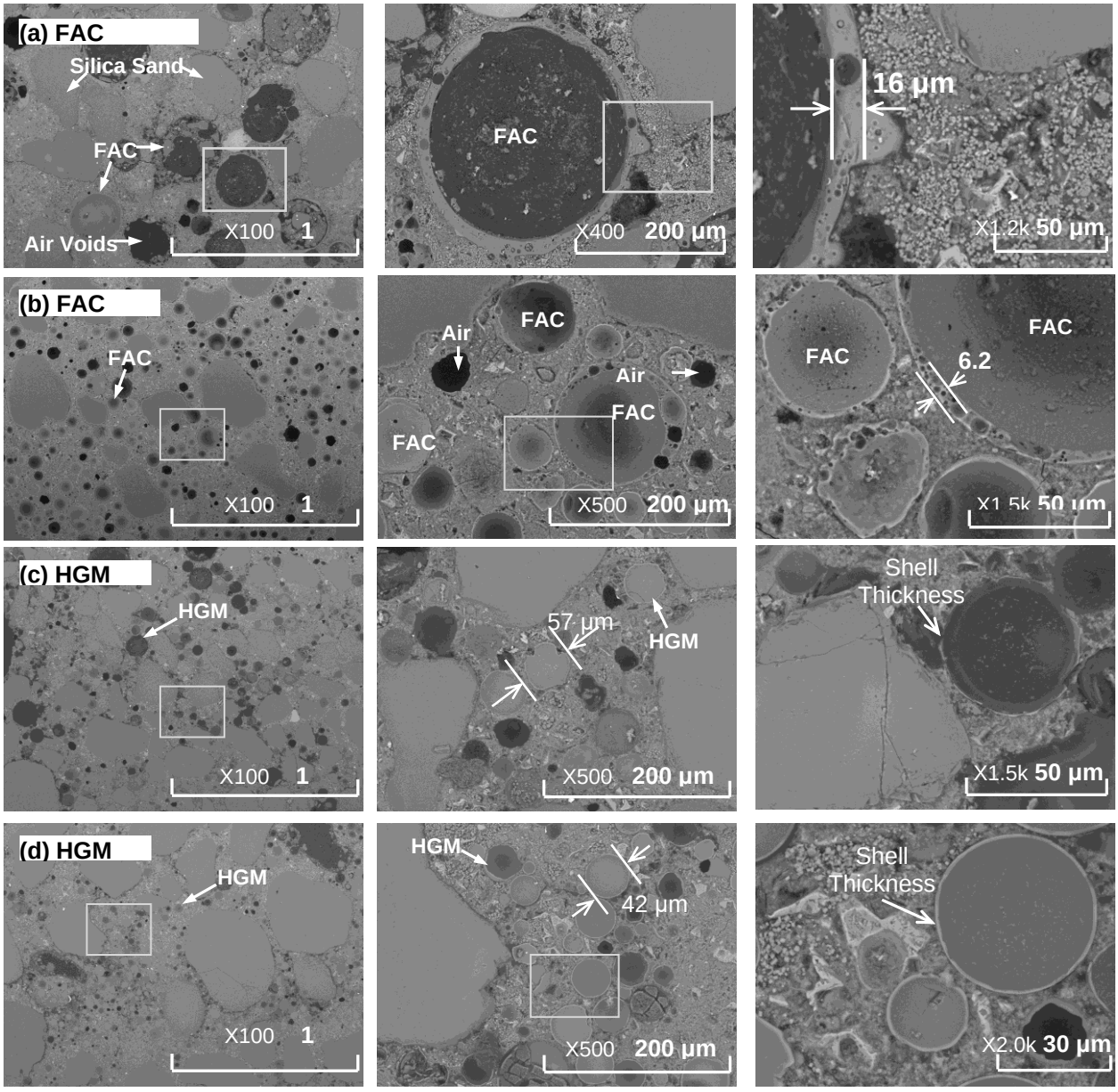

Figure 8: SEM images showing the microstructure of LWCC containing: (a) E200/600 fly ash cenosphere (FAC); (b) E160 FAC; (c) K25 HGM (0.25 g/cm^3); and (d) S60 HGM (0.60 g/cm^3)

materials at microscopic scale are different for the various LWF types used in this research. For LWCC containing EPS beads, the lightweight aggregates mostly act as weak points within the mortar system which promote the initiation and percolation of stress cracks, see Figure 9(a). Similarly, the ETM particles within the LWCC are too weak to resist the micro-cracks developed within the material even though its particle size is much smaller than that of EPS, see Figure 9(b). Therefore, as the LWF volume fraction v_f increases, the strengths of both EPS and ETM groups decrease continuously, see Figure 7(a), even though the LWCC containing ETM has shown marginally higher strength when v_f is low. This is believed due to the lubrication effect of ETM particles which reduced the air content of the mortar.

The fracture surface of HGM K25 modified LWCC have shown a large amount of particle breakage inside the tested mortar. The low shell thickness to particle size ratio (*t*/*D*) leads to its relatively low crush strength (Table 1). The low mechanical strength of these particles could not resist the stresses within the LWCC composites [48] and the stress cracks mostly propagated through the K25 HGM particles, see Figure 9(c). On the other hand, the LWCCs incorporating HGM S60 particles showed a different behavior. The S60 particles are generally smaller in size (with average particle size around 30 μm) and have thicker shell (about 1.5 μm in thickness) as compared to the K25 particles. As a result, the S60 HGM has much higher isostatic crush strength as noted in Table 1. The higher mechanical strength of LWF particles would alter the damage mode within the LWCC material, where it can be observed that the crack growth was resisted by the HGM S60 particles by hindering its path. While some S60 particles did break, many particles within the mortar have shown pull-out instead of shell breakage, see Figure 9(d).

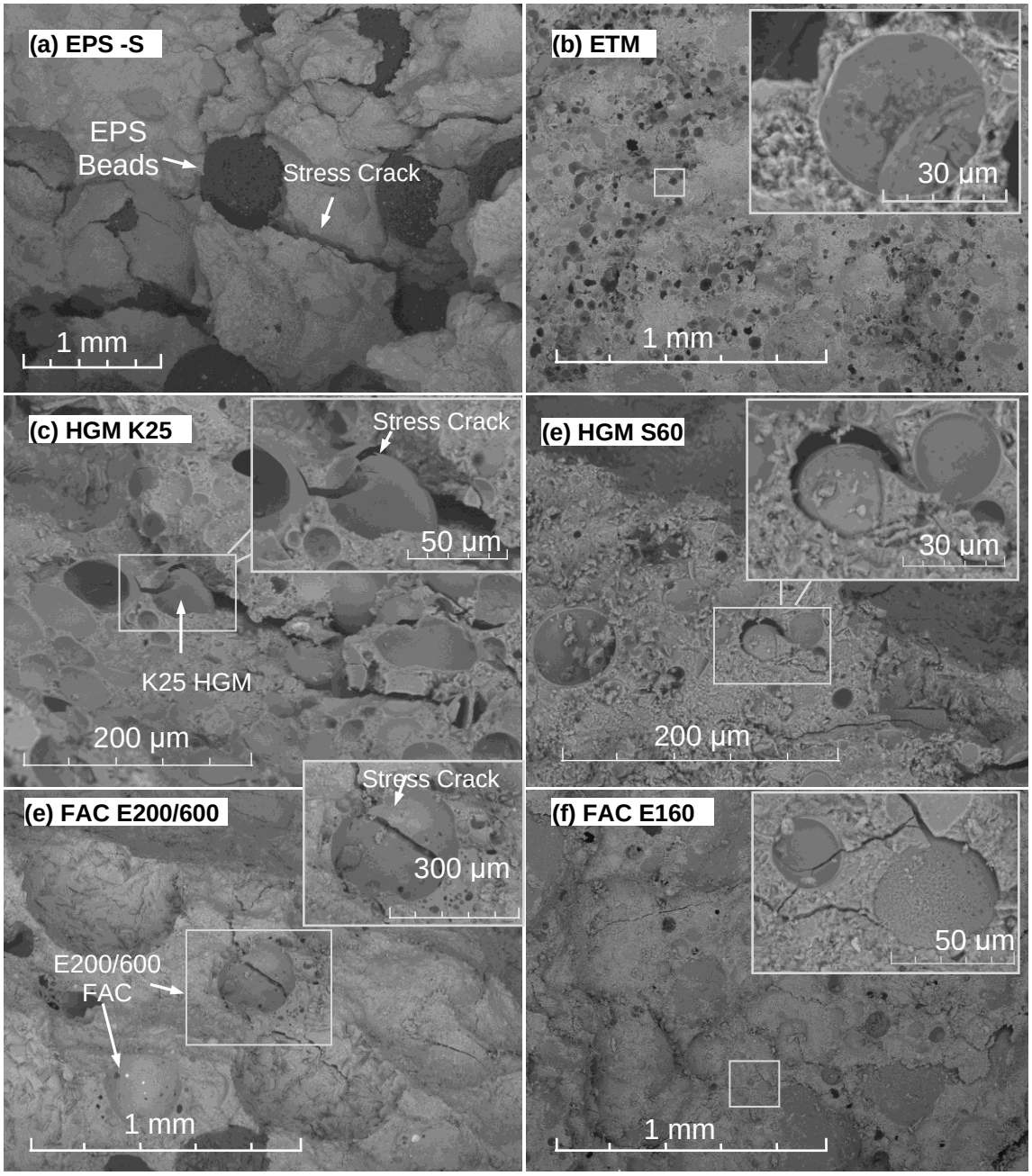

Figure 9: Fracture topography showing the fracture surfaces of LWCCs containing: (a) EPS beads (1 mm); (b) ETM plastic microsphere; (c) K25 and (d) S60 glass microspheres; and (e) E200/600 and (f) E160 FAC

Moreover, weak ITZ (interfacial transition zone) characteristics and debonding were also observed for HGM particles.

The LWCC containing fly ash cenospheres (FAC) generally exhibit good mechanical performance, see Figure 7 (c). For all three types of FACs studied in this research, the FAC particles bonded well with the cementitious matrix, owing to the micro-porous surface of FACs (Figure 3 (c)) as well as its partial pozzolanic reactivity [76]. It was revealed in the XRD analysis (Figure 3 (a)) that FAC particles contain amorphous silica which can react with the pore solution (i.e., calcium hydroxide) in the reacted cementitious binder. Similar to HGM, the larger FAC particles (E200/600) allow stress cracks to propagate through their shell (Figure 9 (e)) whereas the smaller E160 FAC may act as barriers to hinder the propagation of stress cracks (Figure 9 (f)).

3.1.7 Thermal conductivity of LWCC containing particulate LWFs

The effective thermal conductivity of lightweight cementitious composites (LWCC) containing hollow sphere particles can be calculated based on the equations proposed by Felske [109] as a function of the properties of each composing phase, their volume fractions, and the contact thermal resistance at the particle-to-matrix interface:

Equation 2:

$$k_{eff} = k_1 \frac{2\left(1-\nu_f\right)\Omega + \Gamma_N \beta}{\left(2+\nu_f\right)\Omega + \Gamma_D \beta}$$

where

Equation 3:

$$\Omega = \left(2 + \nu_{f3}\right)\frac{k_3}{k_2} - 2\left(1 - \nu_{f3}\right)$$

and

Equation 4:

$$\Gamma_N = \left(1 - \nu_f\right)\left[2\left(1 + 2\nu_{f3}\right) - 2\frac{k_3}{k_2}\left(1 - \nu_{f3}\right)\right] + \left(1 + 2\nu_f\right)\left[\frac{k_3}{k_1}\left(2 + \nu_{f3}\right) - 2\frac{k_2}{k_1}\left(1 - \nu_{f3}\right)\right]$$

Equation 5:

$$\Gamma_D = \left(2 + \nu_f\right)\left[\left(1 + 2\nu_{f3}\right) - \frac{k_3}{k_2}\left(1 - \nu_{f3}\right)\right] + \left(1 - \nu_f\right)\left[\frac{k_3}{k_1}\left(2 + \nu_{f3}\right) - 2\frac{k_2}{k_1}\left(1 - \nu_{f3}\right)\right]$$

where ν_f is the volume fraction of the LWF particles; k_1 is the thermal conductivity of the cement paste; k_2 is the thermal conductivity of the LWF shell; ν_3 and k_3 are the volume fraction and thermal conductivity of the cavity (air), respectively; and β is the interfacial thermal resistance, see Figure 10(a). Note that:

Equation 6:

$$\nu_{f3} = \frac{\nu_f}{\nu_3} = \left(\frac{r_2}{r_3}\right)^3$$

and the density of the LWF particle, u, is:

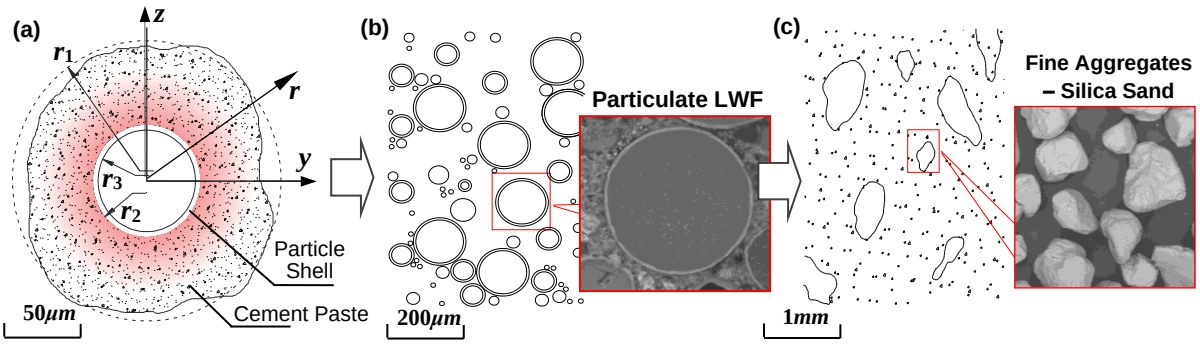

Figure 10: Microstructure and effective thermal conductivity of lightweight cementitious composite (LWCC):
(a) a RVE containing one single microsphere particle; (b) cement paste with polydispersed microsphere particles; and (c) LWCC mortar with fine aggregates (e.g., silica sand)

Equation 7:

$$u = \left(1 - \frac{r_3^3}{r_2^3}\right)\rho_s$$

where ρ_s is the shell density of the hollow spheres, and the mass of air in the cavity is neglected. From Equation 6 and Equation 7 and we simply have:

Equation 8:

$$v_{f3} = \frac{\rho_s}{\rho_s - u}$$

Thus, the effective thermal conductivity of LWCC filled with spherical LWFs, i.e., Figure 10(b), can be expressed in terms of the particle volume fraction, v_f, the thermal conductivities of each included phase, and the measured density of the LWF particle, *u*. Note that the density of LWF particles can be experimentally measured by methods including gas pycnometry [110] and is often reported in the particle manufacturer data sheets.

Since the thermal conductivity of air is notably lower than the other two solid phases – i.e., the cement paste and microsphere shell ($k_3 \to 0$) and assuming perfect thermal contact between the cement matrix and LWF ($\beta \to \infty$), then substitute Equation 8 into Equation 2 we have:

Equation 9:

$$k_{eff} = \left[\frac{(\eta + 2) + 2(\eta - 1)v_f}{(\eta + 2) - (\eta - 1)v_f}\right]k_1$$

where $\eta = 2k_{21}u/(3\rho_s - u)$, and $k_{21}=k_2/k_1$. Thus, the effective thermal conductivity of LWF filled cement paste can be simply calculated as a function of the thermal conductivity of the cement paste matrix, k_1, particle volume fraction, v_f, density, u, and the LWF shell properties, k_2 and ρ_s. It is worthwhile noting that for Equation 2 Equation 9, the thermal conductivity of micro-size LWF particles, which is proved to be difficult to experimentally obtain [62], is not required for calculating the equivalent thermal property.

It is noted that for LWF modified by phase changing materials (PCMs) [57], Equation 9 can be modified to account for the thermal conductivity and the temperature-dependent heat capacity of PCMs [111].

For LWCCs with fine aggregates (e.g., silica sand, Figure 10 (c)), the homogenized effective conductivity and specific heat capacity can then be calculated by treating the LWF filled cement paste as a homogenized matrix phase with regular fine aggregates dispersed in it (a two phase composite system as shown in Figure 10 (c)). Thus, many two-phase homogenization methods such as the Maxwell-Garnett model [40], Hashin and Shtrikman model [41] and generalized self-consistent method [114] can be used to calculate the equivalent thermal properties.

Figure 11 shows the comparison between the calculated thermal conductivities of HGM (i.e., K25, S32, H50, and S60) filled cement mortars versus the values measured by the TPS

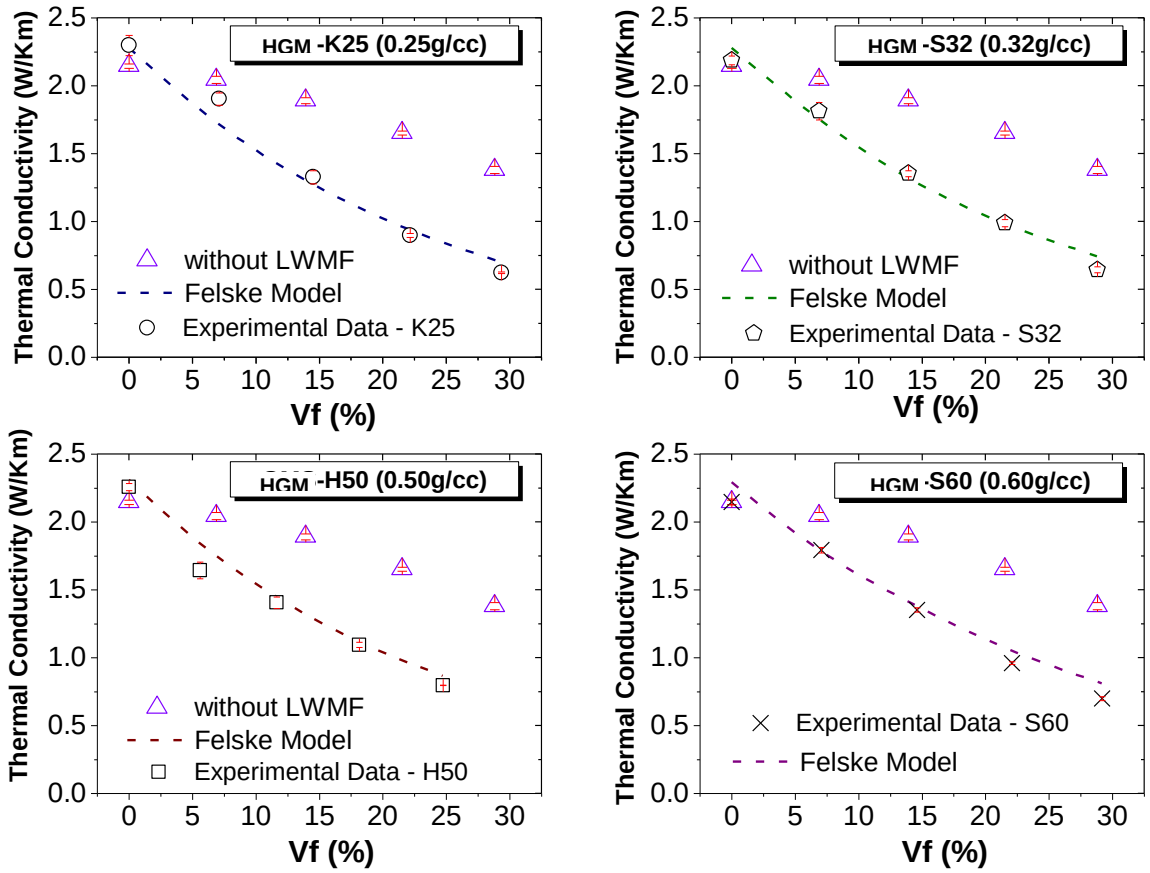

Figure 11: Comparisons between the predicted thermal conductivities as functions of the LWF volume fraction

method. At w/c=0.43, the thermal conductivity of cement paste matrix (k_1) was tested at 0.66 W/mK. The LWF particle properties involved in Equation 9– i.e., particle density, *u*, are listed in Table 2; the shell density, ρ_s, of TPMS, HGM, and FAC are 0.975 g/cm^3, 2.51 g/cm^3, and 2.03 g/cm^3, respectively; and thermal conductivity of shell material, k_2 for TPMS, HGM, and FAC are 0.15 W/mK, 1.05 W/mK, and 0.62 W/mK, respectively. The specific density and thermal conductivity of silica sand were taken as 2650 kg/m^3 and 7.5 W/mK. Since the decrease in thermal conductivity is partially due to the reduction of sand ratio, the thermal conductivities of cement mortars having the same sand to binder ratio (without LWMF) corresponding to each LWMF volume concentration are plotted in Figure 11 for the purpose of comparison. The experimental data and the predicted results for mortar samples with four types of HGMs are compared. It shows a close match between experimental tested data and the predicted results. Since the thermal conductivity is shown to be insensitive to the type of LWF by both the experimental results (Figure 6) and the Felske model predictions, the comparisons for all 55 mixture groups are not redundantly shown herein.

3.1.8 Thermal conductivity and strength: the implication on building structural and energy performance

Figure 12 presents the mechanical and thermophysical property map tested for the LWCCs, where the material's thermal conductivity is plotted against the compressive strength

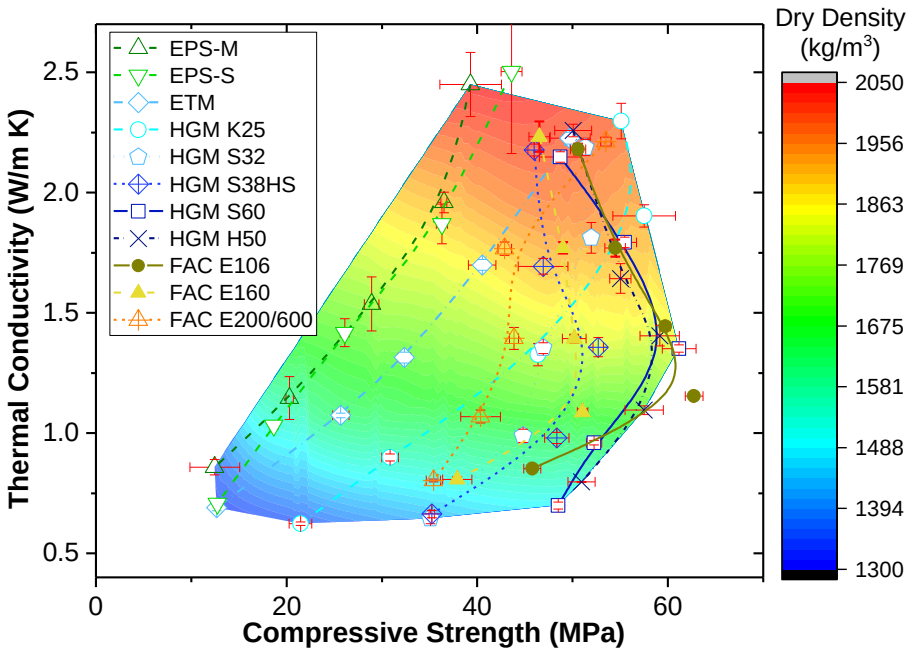

Figure 12: Thermal and mechanical properties map of LWCC.

and the color contour indicates dry density. Unlike the correlations between thermal and mechanical properties of traditional lightweight aggregate concrete [115], foamed cellulous concrete [116], and EPS concrete [67] where the strength is inversely proportional to the material's thermal resistance, the thermal-mechanical property map of LWCC containing micro-size LWF fillers has shown large design space. The material properties can be fine-tuned by varying the volume fraction, size, and shell property of LWF. Since the thermal conductivity and specific heat capacity are primarily functions of the LWF volume fraction, the dependency of the material's mechanical performance on the size and shell property of LWF provides opportunities to develop high performance structural materials that have high mechanical strength whilst possessing the desired thermophysical properties such as lightweight, low thermal conductivity, and even latent heat storage (e.g., the study on PCM loaded cenospheres by Liu et al. [57]). Figure 13 presents the correlations of strength and thermal resistance of four different LWCCs tested in this study as functions of the LWF volume fraction (i.e., R-value is calculated for a 15 cm wall made from such material). It can be seen that high strength and high insulation building/ structural material can be produced by incorporating smaller size LWF particles with strong shells.

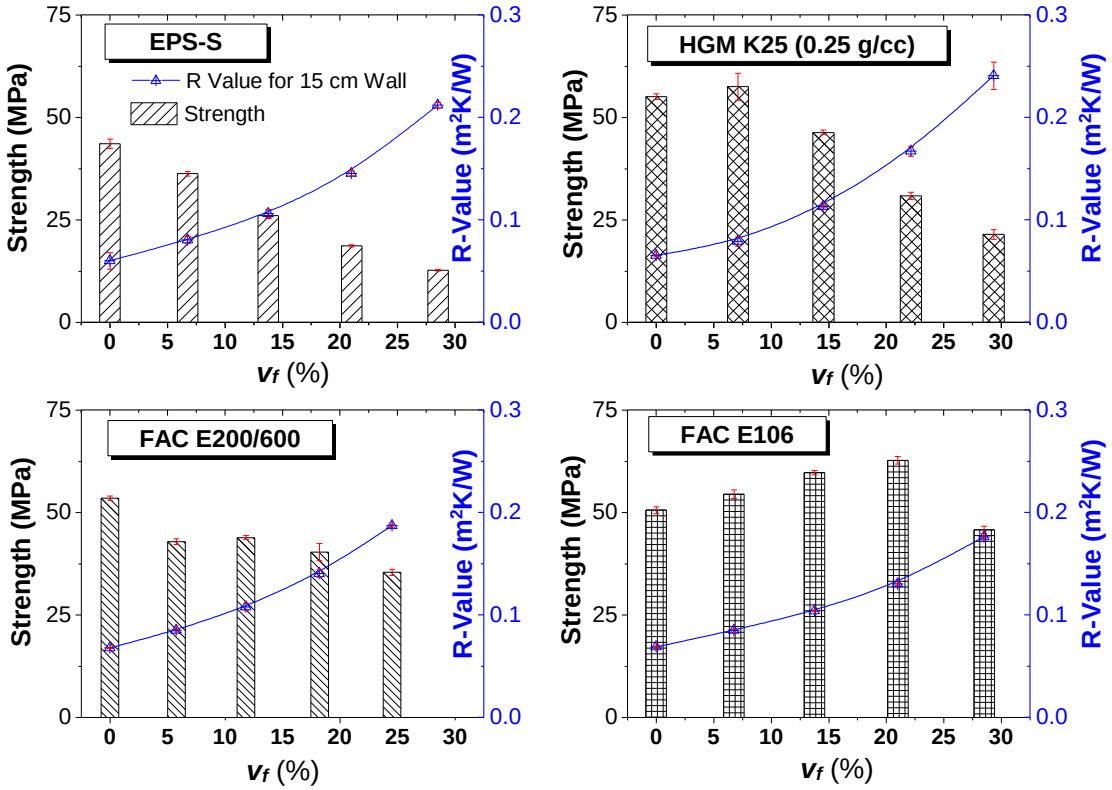

Figure 13: Correlations between compressive strength, thermal resistance (R-value), and the volume fraction of LWF particles

3.2 Thermal energy storage cementitious composites

The incorporation of phase change materials (PCMs) in cement-based materials opens pathways for large-scale thermal energy storage with tremendous opportunities for energy saving. However, traditional use of polymer micro-encapsulated PCMs (MEPCM) in cement-based materials lead to several well-known drawbacks (e.g., detrimental to mechanical performance, lower thermal conductivity, and high costs). In this research, a novel micro-encapsulation pathway is pursued, using fly-ash cenosphere to encapsulate PCMs for high volume use in cement-based materials. A comparative study was conducted to elucidate the effects of the cenosphere encapsulated PCMs (namely CenoPCM) and its polymer micro-encapsulated counterparts on the mechanical and thermal properties of functionalized cement-based materials.

3.2.1 Preparation of fly-ash cenopshere encapsulated phase change material (CenoPCM)

The production of fly-ash cenosphere encapsulated phase change material (or CenoPCM) follows the procedure outlined in one of the authors' earlier papers [57]. In this study, a fatty-acid derivative, i.e., PureTemp 29 (*Entropy Solutions, LLP*), was selected as PCM to be encapsulated because of its high heat of fusion (~200kJ/kg), cyclic stability, and good cost-performance for potential large-scale building applications. Cenospheres used in this research were obtained from CenoStar Corporation (USA). It has sizes between 10 and 160μm with

D_{10} = 44.9μm, D_{50} =90.6 μm and D_{90} = 155.4μm, as shown in Figure 14.

The three-step process outlined in [57] was used to encapsulate the PureTemp^{TM} fatty acid PCM in micro-sized fly-ash cenospheres, see Figure 15: (1) perforating cenospheres with acid etching; (2) loading melted PCM into perforated cenospheres, and (3) sealing the PCM

loaded cenospheres. Cenosphere particles are comprised of an aluminosilicate shell (typically a few micrometers thick) with high stiffness and strength [51]. The shell has a porous structure (Figure 14 (d)) covered by a glass-crystalline layer [117]. The hollow interior of cenospheres (typically over 80% in volume) makes it an ideal material to encapsulate functional agents such as PCM. To make the cenosphere interior accessible during PCM impregnation, acid etching technique is employed to open the pathway to load melted PCM. To this end, approximately 12 g of cenospheres were soaked into 250 mL of 1.0M NH_4F-1.2 M HCl-H_2O solution for 2 h with occasional stirring. The specific gravity of the cenospheres is about 0.75 g/cm3, thus 12 g of the cenospheres corresponded to a volume of 16 mL. This made the volume ratio of solid to liquid to 1:15 in this acid treatment, which was among the range adopted by other researchers [118,119]. Occasional stirring was applied instead of continuous one to prevent the possible damage of the cenospheres during stirring. To compensate for this mild stirring process, longer treatment time was used (2 h). After etching, the perforated cenospheres were vacuum filtered and rinsed with 1500 mL of water, followed by being dried in an oven at 150℃.

Following the acid etching, a vacuum impregnation process was employed to load melted liquid PCM into perforated Cenospheres, see Figure 15. The dry perforated cenospheres were placed in a flask with a vacuum pressure of approximately 80.5 kPa for ~2 h [120]. Melted PCM was then introduced into the flask before the vacuum was shutoff to allow air back into the flask to drive the liquid PCM into the hollow space inside the cenospheres. During the

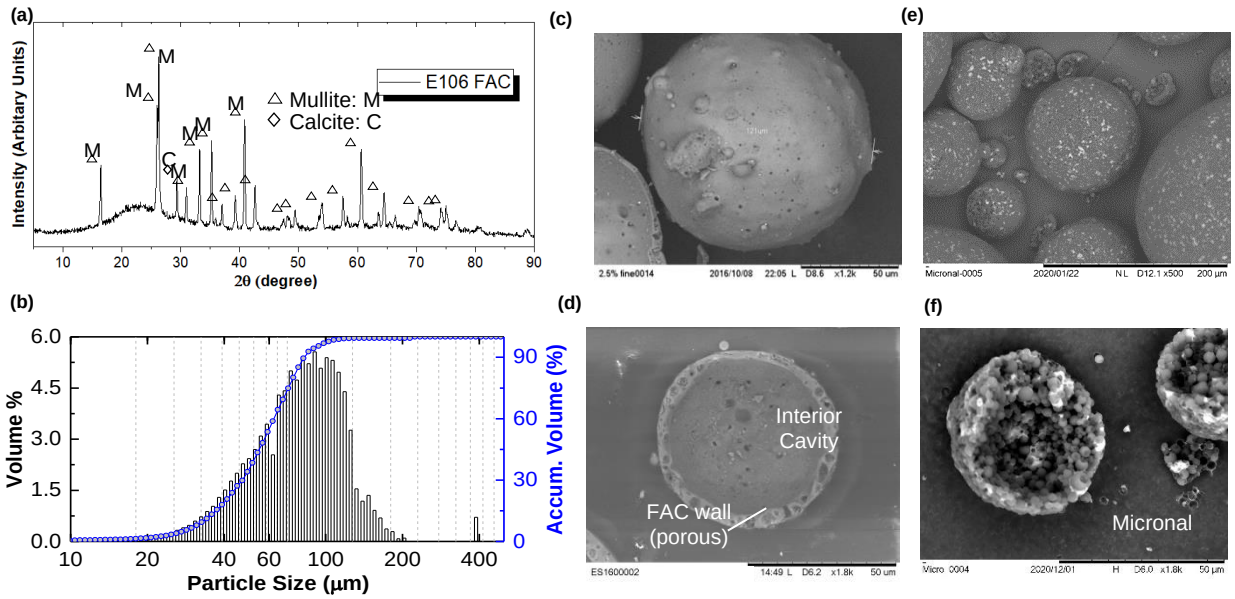

Figure 14: Properties of the fly-ash cenosphere (FAC) used for microencapsulation and the Micronal MEPCM:
(a) X-ray diffraction (XRD); (b) particle size distribution; (c) SEM image showing the FAC surface morphology; and (d) polished section showing the porous wall structure of FAC; (e) conglomerate of Micronal particles; (f) zoom-up view showing individual particles making up the conglomerate.

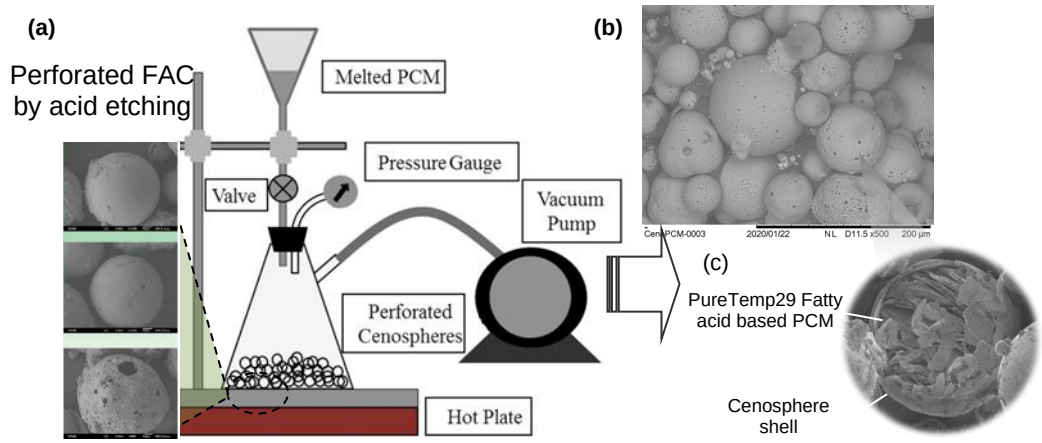

Figure 15: CenoPCM production:
(a) Illustrative figure showing the process to produce CenoPCM; (b) CenoPCM micro-capsules produced; and (c) an intentionally broken CenoPCM showing the interior of the CenoPCM micro-capsules successfully loaded with fatty-acid PCM

impregnation process, the flask was heated in a water bath at 60℃ to keep the PCM in the liquid state. At completion of loading, the flask was quickly removed from the hot water bath for the PCM loaded cenospheres to be filtered, washed in warm water to remove the PCM residuals on FAC surface. Then the loaded CenoPCM was rinsed with cold water and air-dried. Lastly, a thin layer of nano silica coating was applied on the cenosphere surface to seal the surface pores. The nano silica coating is applied by soaking the PCM loaded cenospheres into 25% silica sol. The volume ratio between cenospheres and silica sol was kept at around 1:3 during soaking with occasional mechanical stirring. Then the coated cenospheres were filtered and air dried to allow nano silica particles to precipitate on the cenosphere surface. It was noted that due to the nonhomogeneous surface of cenospheres, the silica sol coating on CenoPCM surface is not uniform. Further study is needed to develop more uniform and reliable coating for CenoPCM sealing/coating.

3.2.2 Thermophysical properties of CenoPCM

The thermophysical properties of CenoPCM is characterized through differential scanning calorimetry (DSC), thermogravimetric analysis (TGA), and gas pycnometry. The true density of the CenoPCM is characterized using a *Quantachrome UltraPYC 1200E* gas pycnometer. The density is measured using volume measurements by pressurizing the sample cell with Helium. A valve is then opened to a separate chamber, the pressure change within the chamber is measured and the sample's true volume is calculated based on Boyle's law. Table 3 lists the density tested for CenoPCM with and without silica-sol coating, and the true density of the Micronal® benchmark tested using gas pycnometry.

Figure 16 (a) shows the DSC results (*TA Instrument Q2000*, scanning rate 10℃/min.) performed on both the CenoPCM and the commercially available Micronal® (polymer

encapsulated PCM). The CenoPCM has around 125kJ/kg latent heat at phase change with phase change onset temperature of 27℃. The latent heat of the Micronal® benchmark was tested at 90.3kJ/kg with phase change onset temperature of 22℃, also see Table 3. Figure 16(b) presents the TGA results of CenoPCM containing fatty acid PCM core, showing that the thermal decomposition initiates at around 145℃ and the mass percentage remaining at 300℃ is 44.53%. Given the densities of the cenosphere shell and fatty acid core are 2.4 g/cm^3 and 0.91 g/cm^3, respectively, the volume percentage loading of PCM is estimated at around 76%. This result is also consistent with the density test data. It is noted that the particle size of Micronal listed in Table 3 references to the conglomerate particle of the Micronal®, which consist of many smaller particles clumped together by the manufacturer for handling safety, see Figure 14(e) and (f).

The effects of silica sol coating and cementitious matrix on the behavior of CenoPCM was studied by DSC. The thermophysical properties of silica sol coated CenoPCM including density, heat of fusion, and phase change onset temperature are listed in Table 3 in comparison with the uncoated samples, where the latent heat of silica sol coated cenoPCM reduced from 118.8 kJ/kg to 59.61 kJ/kg which indicates roughly 30 vol% of nano-silica coated on the cenoPCM particle surface. Then, the silica sol coated CenoPCM was mixed with cement paste to prepare mortar samples (without silica sand) according to. Silica sand was not included in the mix design due to the small sample volume required for preparing DSC samples – i.e., the particle size of silica sand makes it difficult to obtain homogenous and representative samples, while silica sand does not interfere with the interaction between the PCM microcapsules and the cementitious matrix. Figure 17(a) presents the hysteretic DSC scanning results of uncoated CenoPCM, silica sol coated CenoPCM and silica sol coated CenoPCM mixed in cementitious matrix at volume load of 10 vol%, 20 vol%, and 30 vol%. It can be observed that the heat of fusion, ΔH_m,obtained from DSC

Table 3. Properties of the MEPCM materials used in this research

Material	Particle Size (μm)*			True Density**	Crush Strength (MPa)***	Heat of Fusion, ΔH_m		Phase Change Temp, T_m
	D_{10}	D_{50}	D_{90}	(g/cm^3)		kJ/kg	kJ/L	
Micronal	62.3	192	308	1.005	<1 MPa	90.31	90.74	22°C
CenoPCM (uncoated)	44.9	90.6	155.4	1.383	5.51 MPa	118.76	164.24	27°C
CenoPCM (silica coated)		--		1.682	--	59.61	100.24	27°C
Silica Sand	300	600	1350	2.650	--	--	--	--
Quartz Flour	1.60	13.6	38.6	2.650	--	--	--	--

* Particle size distributions were obtained using dynamic light scattering. The particle size and crush strength of silica sol coated CenoPCM are assumed the same as those of CenoPCM

** The true densities of Micronal and CenoPCM were obtained using gas psychometry. Density value reported as the mean value of three measurements.

*** The crush strength was determined using an isostatic method for the tested bubbles to have 90% survival rate.

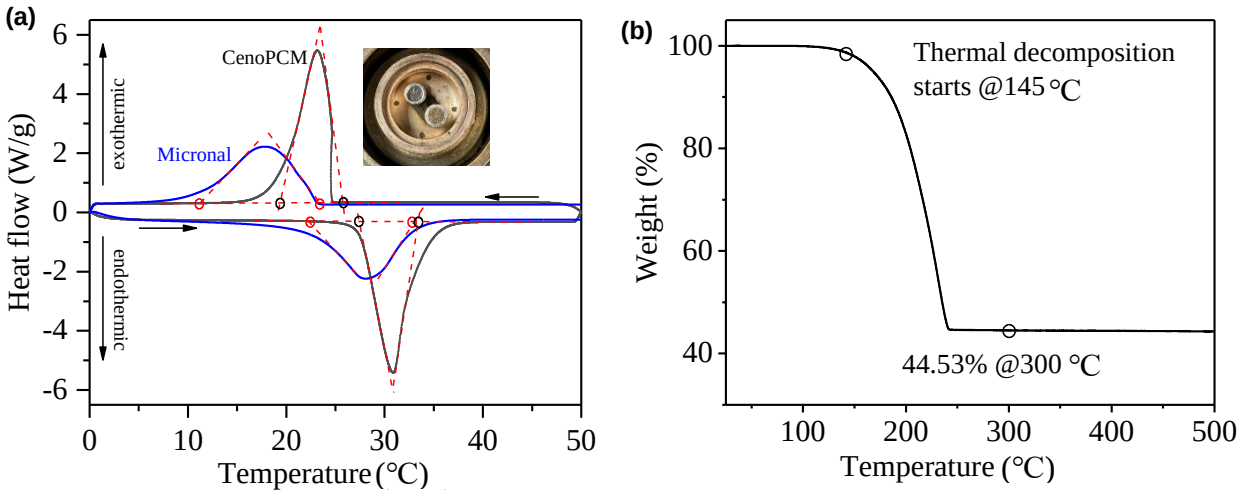

Figure 16: Thermophysical Properties of MEPCM:
(a) Differential scanning calorimetry (DSC) hysteresis of CenoPCM versus Micronal®; and (b) thermogravimetric analysis (TGA) performed on CenoPCM

Table 4. Mixture design of cementitious composites (no silica sand) containing CenoPCM

	Cement (g)	Water (g)	CenoPCM (g)	Cement (wt %)	Water (wt %)	CenoPCM (wt %)	ΔH_m (Theoretical)	ΔH_m (Tested)	Diff.
ref	45.8	5.1	0.0	90.0%	10.0%	0.0%	0.00	0.00	--
10vol% CPCM	14.2	4.5	1.7	69.6%	22.1%	8.3%	4.94	4.85	-1.9%
20vol% CPCM	12.6	4.0	3.4	63.1%	20.0%	16.9%	10.08	10.24	1.6%
30vol% CPCM	11.0	3.5	5.1	56.2%	17.9%	25.9%	15.44	14.43	-6.6%

scans matches well with the theoretical values calculated from the wt% of CenoPCM in the cementitious material system, indicating that the heat storage capability of CenoPCM are unaffected by the cementitious matrix, see. It is also observed from Figure 17 that the phase change onset temperatures of cementitious composite with CenoPCM are not affected by the cementitious matrix, see Figure 17(b).

3.2.3 Mix design and materials preparation

The constituent materials used for preparing the functional cementitious composite mortars in this study include ASTM Type I-II Portland cement, silica sand (*US silica*), water, superplasticizer (*Sika Corp.*), and micro-encapsulated PCMs (i.e., CenoPCM and Micronal®). The water to cement ratio (w/c) was 0.32 for all mixtures. The mass of cement, sand, and water used for each cubic meter of the reference mortar (without MEPCM) are 731 kg/m^3, 1219 kg/m^3, and 234 kg/m^3, respectively. Two types of micro-encapsulated PCM were used in this project, i.e., the CenoPCM with PureTemp 29 fatty-acid based PCM core and the commercially available Micronal® 24D (*Microtech Labs*). The Micronal® 24D was selected as a commercially available benchmark to compare the mechanical and thermophysical properties of cementitious composites containing different types of MEPCMs (i.e., soft polymer shell vs. rigid cenosphere shell). For cementitious composites containing Micronal®, or CCMi, six volume fractions (3.5%, 7.0%, 10.5%, 14.0% 17.5%, and 21.0%) were evaluated; for cementitious composites containing CenoPCM, or CCPCM, seven volume fractions (2.9%, 5.8%, 8.6%, 11.6%, 14.5%, 17.4%, and 20.3%) were evaluated. For each mixture with MEPCM added, the equivalent volume of sand and quartz powder (fine aggregate) was replaced by the MEPCM. Detailed mix design of all cementitious composite groups made in this study are summarized in Table 5.

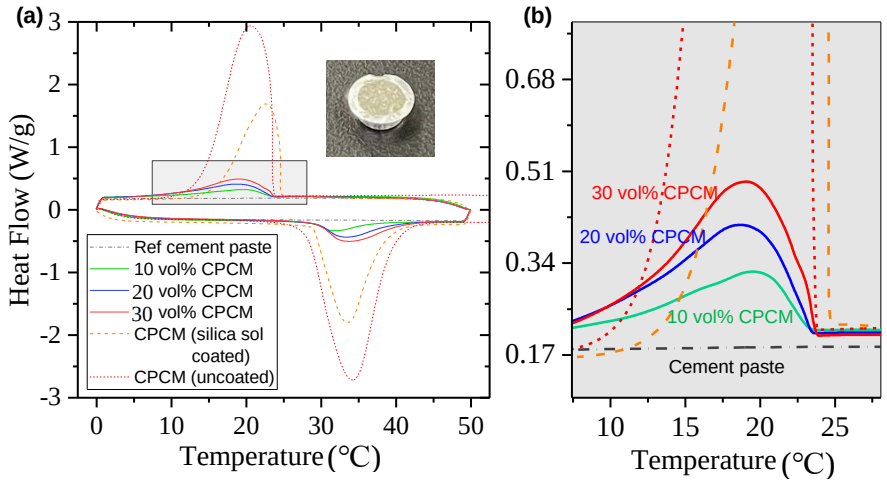

Figure 17: Effects of cementitious matrix on the CenoPCM properties: (a) DSC traces of silica sol coated/uncoated CenoPCM and cementitious composites (no silica sand) containing silica sol coated CenoPCM; and (b) the zoomed-in view of the DSC scan showing the exothermic process.

Table 5. Test matrix and mix proportions (by weight, kg of materials/m3 of concrete).

Mix ID	Cement	Water	w/c	MEPCM	Silica Sand	Quartz Powder	Air Content	MEPCM Vol%
Control	762	244	0.32	0	1270	62	0.010	0.0
CCMi-036	759	243	0.32	36	1170	56	0.016	3.6
CCMi-072	756	242	0.32	71	1069	52	0.021	7.2
CCMi-108	753	241	0.32	106	969	47	0.027	10.8
CCMi-144	751	240	0.32	141	872	42	0.031	14.4
CCMi-179	748	239	0.32	176	773	38	0.045	17.9
CCMi-214	743	238	0.32	210	674	33	0.066	21.4
CCPCM-029	760	243	0.32	48	1170	59	0.023	2.9
CCPCM-058	766	245	0.32	97	1083	54	0.025	5.8
CCPCM-086	767	245	0.32	145	987	49	0.033	8.6
CCPCM-116	770	246	0.32	194	894	45	0.038	11.6
CCPCM-145	772	247	0.32	244	798	40	0.046	14.5
CCPCM-174	774	248	0.32	293	701	35	0.054	17.4
CCPCM-20.3	769	246	0.32	341	578	29	0.077	20.3

3.2.4 Experimental method and setup

The transient plane source (TPS) method originally developed by Gustafsson [121] was applied to measure the thermal properties of the cementitious composites. The TPS tests were performed in triplicate for each sample type using a *HotDisk TPS-1500* thermal constant analyzer with a 6.403mm diameter TPS sensor according to the ISO22007-2 specification [122]. The TPS technique is based on the recorded temperature rise of a plane source that heats the surrounding material to be measured. In a TPS test, a conducting pattern with negligible heat capacity (e.g., Kapton supported double spiraled nickel metal sensor as shown in Figure 18(a) serves simultaneously as the heat source and the temperature sensor. The initial electrical resistance of the TPS element, R_0 (calculated for each individual test), is first balanced in a Wheatstone bridge and, during the measurements, the unbalanced voltage drop $\Delta V(t)$ is recorded as the function of time t (20-40 sec) using a high-impedance digital voltmeter, where $\Delta V(t)$ has the following expression [121]:

Equation 10:

$$\Delta V(t) = \frac{R_s R_0^2}{R_0 + R_s} \frac{I_0^3 \alpha}{\pi^{2/3} a} \frac{D(\tau)}{k}$$

where R_s is the standard resistance in the Wheatstone bridge circuit (6.788013Ω), I_0 is the heating current, α is the temperature coefficient of the TPS element, a is the outer radius of the heating element, k is the thermal conductivity of the material, and $D(\tau)$ is a function that can be tabulated for a particular TPS element as a function of the dimensionless parameter $\tau = (\kappa t/a^2)^{1/2}$, where κ is the thermal diffusivity of the material to be tested. Through a process of iteration, the thermal conductivity k and thermal diffusivity κ of the tested material can be simultaneously

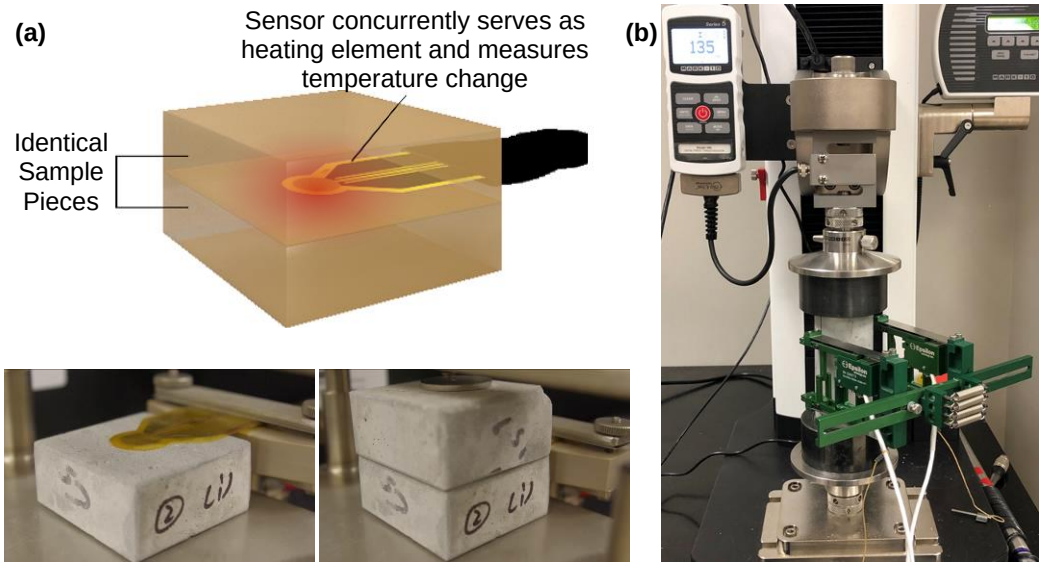

Figure 18: Experimental set-ups for mechanical and thermal testing.
(a) Thermal property measurement using Transient Plane Source (TPS) method; (b) setup for mechanical test of cementitious composite samples

obtained from one single transient recording [123]. For each test an input power and test time is selected, then based on the results of that trial, one or both are adjusted as needed to keep all parameters within the defined limits.

The mechanical tests were performed using a 500kN INSTRON servo-hydraulic universal testing system as shown in Figure 18 (b). For cementitious composite samples, five 50.8 mm (2 inches) diameter by 101.6 mm (4 inches) cylinders were tested for each specimen group listed in Table 5. The mechanical loading procedure was carried out in a displacement-control mode at the loading rate of 0.01 mm/min. The deformation (i.e., compressive strain) was measured using a pair of clamp-on extensometers (*Epsilon Tech*) with gauge length of 50 mm. The setup of extensometers are shown in Figure 18 (b). A high-resolution charged-coupled device (CCD) camera was staged to record the damage and failure of the specimens. The tested specimens were preserved for scanning electron microscopy (SEM) analysis.

The fracture toughness of cementitious composites containing both CenoPCM and Micronal® was evaluated using notched beam tests [124]. Figure 19 shows the experimental setup where flexural specimens (25mm × 50mm × 235mm) were cast using ABS molds. The beams were tested under three-point bending with the load point at the center of the 200 mm span. Each beam was notched at the center with a 5 mm deep notch using a fine diamond band saw and then speckle coated to allow for digital image correlation (DIC) processing. The crack mouth opening displacement (CMOD) was measured at the crack mouth location using a CMOD extensometer. Loading was carried out at a crosshead rate of 0.05 mm/min, and an LVDT was used to measure crosshead displacement. The sensors were conditioned using a *National*

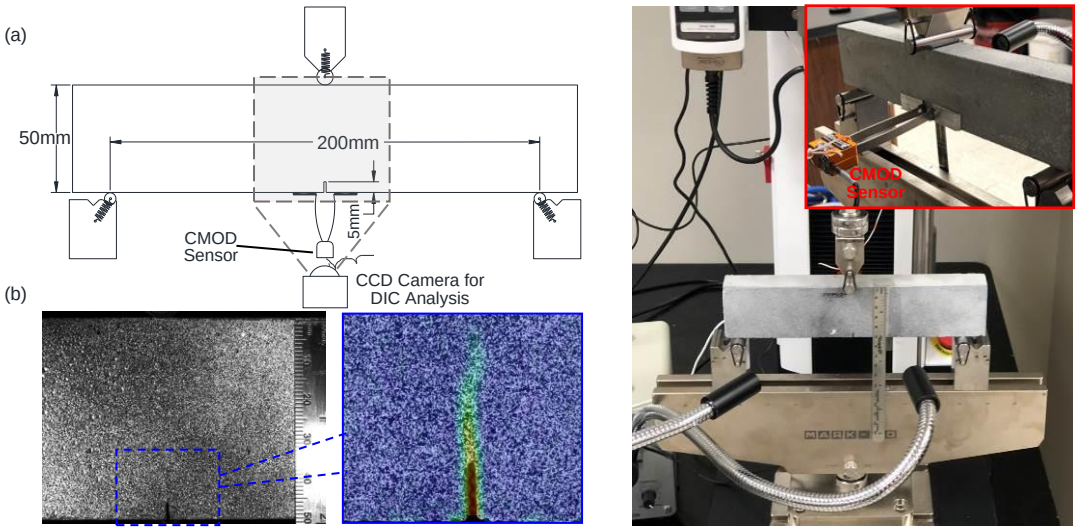

Figure 19: Fracture toughness:
(a) Illustrative figure showing the experimental setup to determine fracture toughness; (b) speckle pattern near the notch for digital image correlation (DIC) analysis and crack initiation detected by DIC; (b) pictures showing the notched beam tests

Instrument PXI-e data acquisition system at sampling rate set at 100 Hz. The data comprised of the applied load and the mid-span beam displacement plots, and the load vs mid-span displacement and load vs crack mouth opening displacement (CMOD) plots for the notched beams. In addition, an effective crack length ($a_{eff)}$ versus stress intensity factor (K_I) plot was calculated using the method described in Banthia and Sheng [125], which uses compliance calibration to obtain the a_{eff} values. For the quasi-brittle materials without fiber reinforcements as studied herein, the K_{Ic} value can be calculated at the peak load point.

3.2.5 Thermal properties

Table 6 shows the summary of density, thermal conductivities (above and below the melt point of encapsulated PCMs), and mechanical properties of cementitious composites containing both CenoPCM and Micronal® MEPCM. For cementitious composite samples that contain Micronal® the density decreased more rapidly than that of the samples with CenoPCM mainly due to the lower density of Micronal®, which is a polymer-encapsulated paraffin wax, see Table 3. The density values were measured under room condition (21℃ and 45% RH) for samples cured for 28 days.

Figure 20 (a) shows the thermal conductivities of the cementitious composites measured at temperatures above and below the melting point of the PCM encapsulated. The thermal conductivity of cementitious composites in general decreases as the volume fraction of the MEPCM inclusion increases. The decrease in thermal conductivity is attributed to two major factors: (1) the addition MEPCM which has a lower thermal conductivity than other compositions in cement mortar and (2) the removal of the portion of silica sand that is replaced by MEPCMs, see Table 5. Note that CCMi samples tend to have lower thermal conductivities (34% of the reference mortar at ~20 vol% Micronal inclusion) compared to the

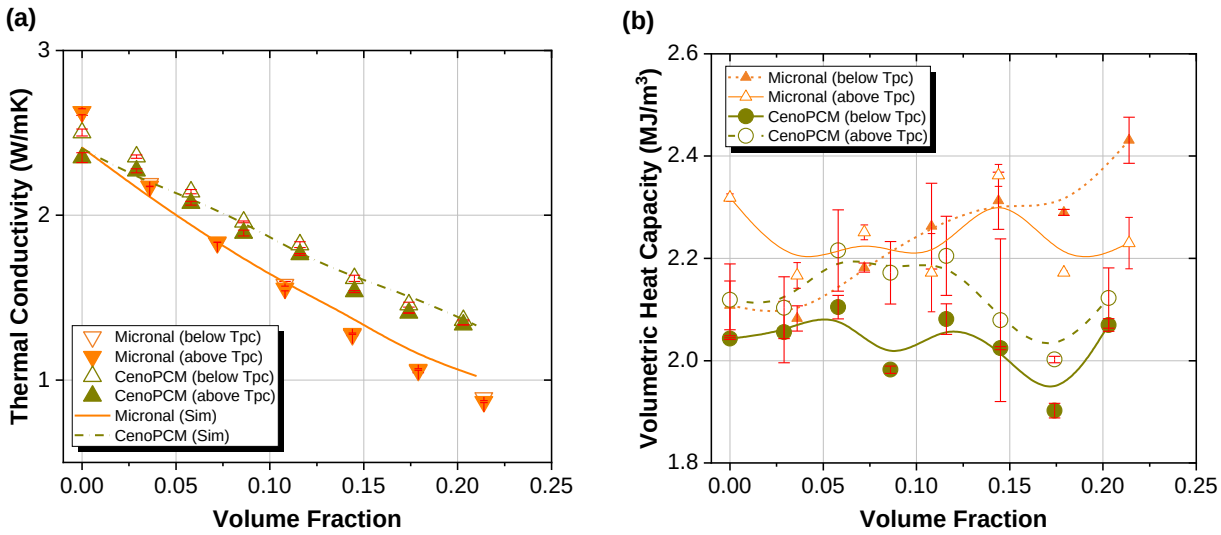

Figure 20: Thermal properties of LWCC tested through Transient Plane Source (TPS) method: (a) Thermal conductivity; (b) Volumetric heat capacity above and below phase change temperature (sensible heat)

Table 6. Density, mechanical, and thermal properties of the tested mixture groups

Mix ID	MEPCM Material Type	MEPCM Volume Fraction	Density*	Elastic Modulus	Compressive Strength	Thermal Conductivity** (below T_m)	Thermal Conductivity*** (above T_m)
		v_f (%)*	(kg/m^3)	(GPa)	(MPa)	(W m^{-1}K^{-1})	(W m^{-1}K^{-1})
Control		0.0	2238.86±15.85	36.57±1.01	88.34±1.31	2.627±0.021	2.628±0.018
CCMi-036		3.6	2180.81±7.75	29.78±0.40	79.19±2.50	2.191±0.012	2.175±0.012
CCMi-072		7.2	2109.09±4.45	23.51±0.25	64.16±0.21	1.833±0.00018	1.836±0.00049
CCMi-108	Micronal®	10.8	2042.09±3.97	19.85±0.32	57.64±2.06	1.579±0.019	1.556±0.014
CCMi-144		14.4	1932.74±6.25	15.39±0.31	49.71±0.98	1.274±0.0041	1.281±0.004
CCMi-179		17.9	1844.10±3.24	12.52±0.08	43.35±1.48	1.058±0.013	1.064±0.005
CCMi-214		21.4	1749.77±5.50	9.88±0.28	37.47±0.50	0.891±0.005	0.869±0.006
CCPCM-029		2.9	2202.84±5.58	35.65±1.52	82.41±1.55	2.356±0.01	2.27±0.012
CCPCM-058		5.8	2168.97±7.84	33.57±1.61	83.06±0.71	2.143±0.013	2.073±0.011
CCPCM-086		8.6	2142.34±5.18	32.06±0.46	85.49±0.45	1.96±0.005	1.892±0.018
CCPCM-116	CenoPCM	11.6	2111.66±6.50	31.74±1.17	87.46±0.82	1.822±0.018	1.762±0.005
CCPCM-145		14.5	2032.00±3.43	27.78±0.51	79.21±0.41	1.617±0.019	1.537±0.006
CCPCM-174		17.4	1992.26±5.38	26.71±1.73	78.55±0.86	1.457±0.015	1.407±0.001
CCPCM-20.3		20.3	1962.20±3.61	22.19±1.21	67.79±0.34	1.362±0.004	1.335±0.0011

***** The density of samples was measured at room temperature and 50%RH.

** Thermal conductivity below T_m was measured at 40%RH at 18°C.

*** Thermal conductivity above T_m was measured at 40%RH at 35°C

CCPCM samples (51% of the reference at ~20 vol% CenoPCM inclusion). This is due to the higher thermal conductivity of the cenosphere shell of CenoPCM (XRD results shown in Figure 14). Only minimal differences were observed for thermal conductivities measured above and below the phase change temperature – Puretemp 29 fatty-acid based PCM has thermal conductivity values around 0.15 W/m K (liquid) and 0.25 W/m K (solid). Using the TPS testing method the volumetric heat capacity of the material can be calculated from the measured thermal conductivity and thermal diffusivity. The volumetric heat capacity as a function of the MEPCM is shown in Figure 20(b). The volumetric heat capacity values are largely unchanged for all volume fractions – CCMi maintained values from 2083 kJ/m3K to 2430 kJ/m3K, while CCPCM ranged from 1902 kJ/m3K to 2215 kJ/m3K. It should be noted that the volumetric heat capacity does not account for the latent heat (heat of fusion) associated with the phase change process of PCMs. The thermal energy storage capacity due to PCM phase change, which is the primary advantage of the functional thermal storage concrete materials, will be discussed in later sections.

3.2.6. Elastic modulus

Figure 21(a) and (b) present the elastic moduli of cementitious composites containing MEPCM (i.e., CenoPCM and Micronal®) with various volume fractions (3-21 vol%) tested at 7 days and 28 days curing, respectively. The elastic modulus is affected by both the physical properties of the added MEPCM and their volume fractions. For cementitious composites containing Micronal® and CenoPCM, both data sets show a downward trend as the MEPCM volume fraction increases. However, for the same volume concentration, CCPCM (mixed with CenoPCM) shows much higher stiffness than that of the CCMi (mixed with Micronal®) – i.e., the reduction in elastic moduli in relation to the reference mortar is much more severe in CCMi

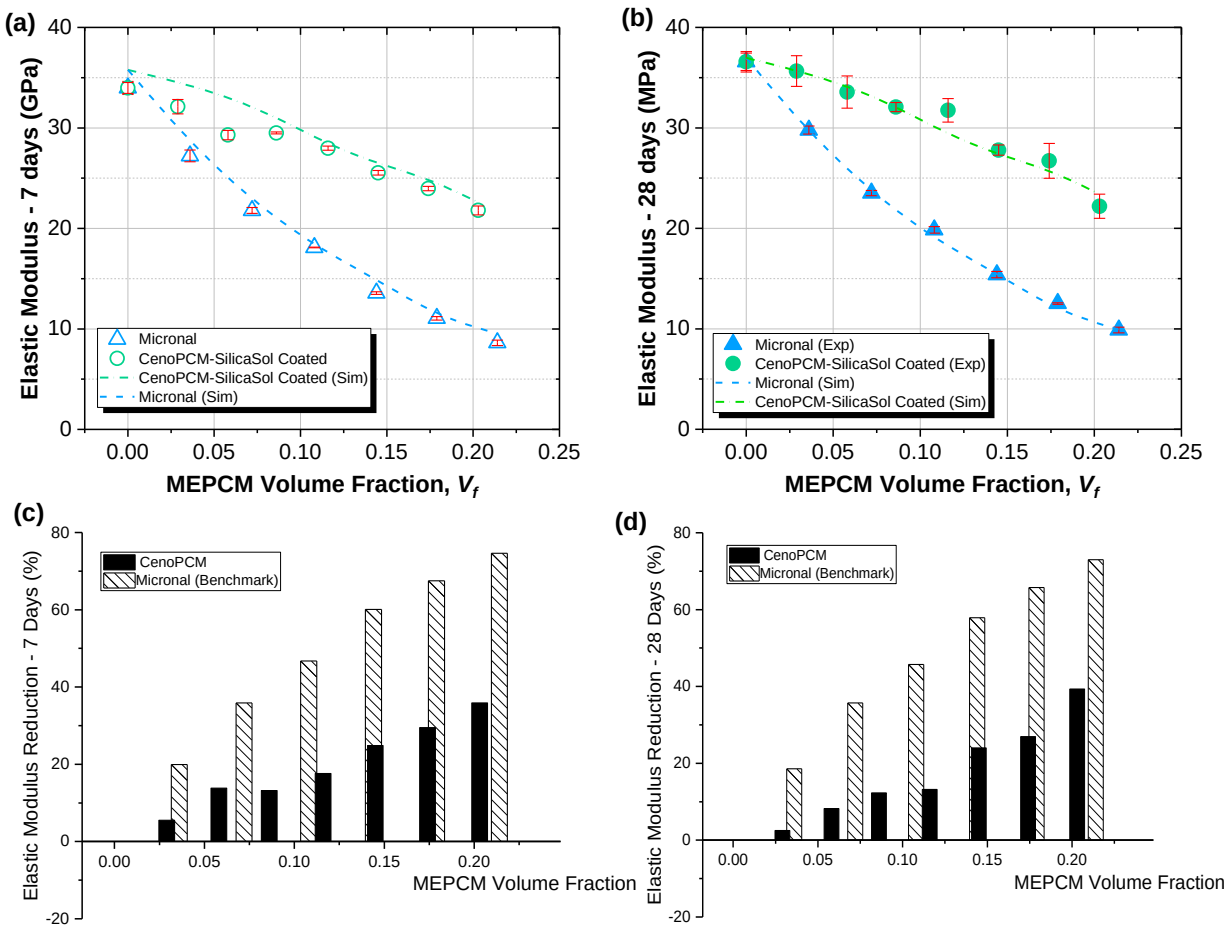

Figure 21: Elastic moduli of cementitious composites containing MEPCM: (a) 7 days; (b) 28 days curing; and the elastic moduli reduction as functions of the MEPCM volume fraction measured at (c) 7 days and (d) 28 days, respectively.

samples. Figure 21(c) and (d) present the percentage reduction (loss) of elastic moduli in relation to the reference mortar as functions of the MEPCM volume concentration, where at around 3.5 vol% Micronal® the reduction in elastic modulus is around 20%; at higher volume concentrations (i.e., 20 vol% Micronal®), the reduction in elastic modulus is as high as 70-75% in comparison with the reference mortar. On the other hand, the CCPCM samples has only 5% reduction in elastic modulus when CenoPCM vol% is 3% and 35% elastic modulus reduction when CenoPCM vol% reaches 20%. The significantly higher stiffness is attributed to the rigid pozzolanic shell of fly-ash cenosphere, which provides mechanical support to the soft fatty-acid PCM core in cementitious matrix. The relations between shell properties (stiffness), shell thickness, and the particle size with its impact on the elastic properties of cementitious composites is discussed in the authors' earlier publications [50,126].Since Micronal® - which is an acrylic polymer encapsulated paraffin, has a softer polymer shell, its influence on the mechanical properties of cementitious materials is rather significant due to the large mismatch of elastic properties between the MEPCM and the cementitious matrix.

3.2.7 Compressive strength

Unlike the thermal properties of the cementitious composite with MEPCM, which depend mostly on the MEPCM volume fraction, the compressive strength is largely dictated by the physical properties of the MEPCM incorporated (e.g., particle size and shell material). Figure 22 (a) and (b) present the compressive strength of cementitious composites with different MEPCM volume fractures, v_f , tested at 7 day and 28 day, respectively. CCMi samples had

On the other hand, CenoPCM microcapsules have a rigid shell, which is comprised mostly of pozzolanic constituents (see the XRD plot shown in Figure 14). The rigid fly-ash shell of CenoPCM provides strong support to the encapsulated PCM core. As a result, the compressive

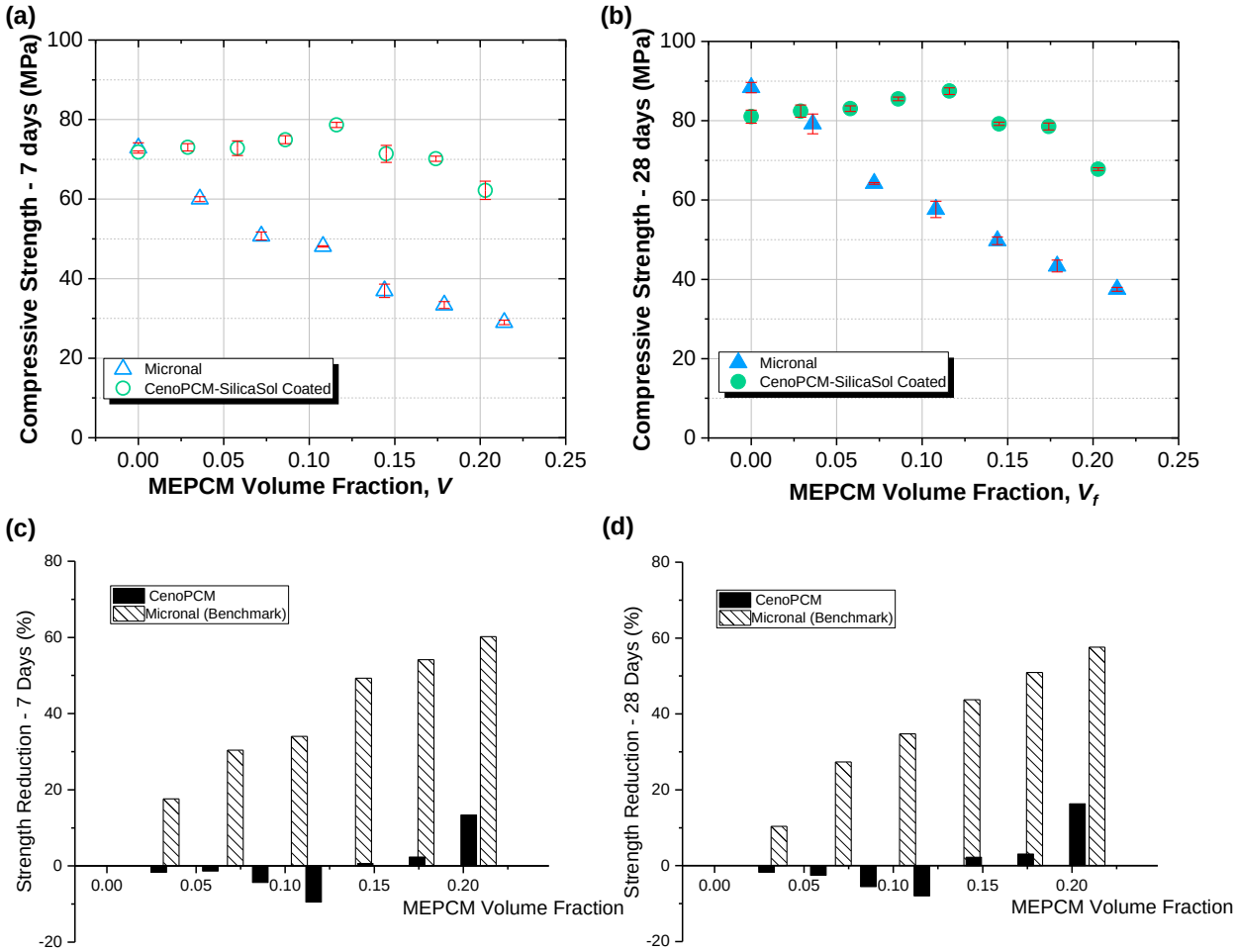

Figure 22: Compressive strength of cementitious composites containing MEPCM: 7 days; (b) 28 days curing; and the compressive strength reduction as functions of the MEPCM volume fraction measured at (c) 7 days and (d) 28 days, respectively.

strength of CCPCM is maintained (or even increased) when CenoPCM volume concentration is low (i.e., vol%<15%). At higher volume concentrations, only moderate strength reduction was observed – i.e., when volume concentration of CenoPCM reaches 20%, only 20% strength reduction was observed (CCPCM with 20 vol% CenoPCM has 28-day compressive strength of 68 MPa, in comparison to 88 MPa of the reference mortar with the same water/cement ratio). This observation is consistent with the authors previous studies [50,51], where rigid-shell core-shell particles within cementitious matrix may help to prevent the propagation of stress cracks at lower concentrations. In addition, the pozzolanic activity of CenoPCM's cenosphere shell, together with its nano-silica coating, helps to develop strong and dense bonding between the CenoPCM particle and the cementitious matrix [127], see Figure 23(b), which further helps to increase the strength of the CCPCM material.

3.2.8 Fracture toughness

Fracture toughness of cementitious composite containing Micronal® or CenoPCM were tested using notched beams under 3-point loading, see Figure 19. Table 7 summarizes the results obtained from the notched beam tests, including the force, displacement, crack-mouth opening displacement (CMOD), as well as the stress intensity factor, K_{Ic}, effective crack length a_{eff}, and the crack tip opening displacement (CTOD) is calculated at the peak load point. Figure 24(a) and (b) present the CMOD against the applied load directly measured from the experiments. The load-CMOD plots were used to determine the point at which unstable crack growth starts, while it can be directly observed from the plots that CCPCM beams have greater resistance to fracture than that of CCMi beams. The non-brittle failure of CCMi with high dosage of Micronal is likely due to the interlocking and fractional effects between micro-crack faces [128]. Figure 24(c) shows the critical stress intensity factor, K_{Ic}, varies as a function of the volume fraction of the

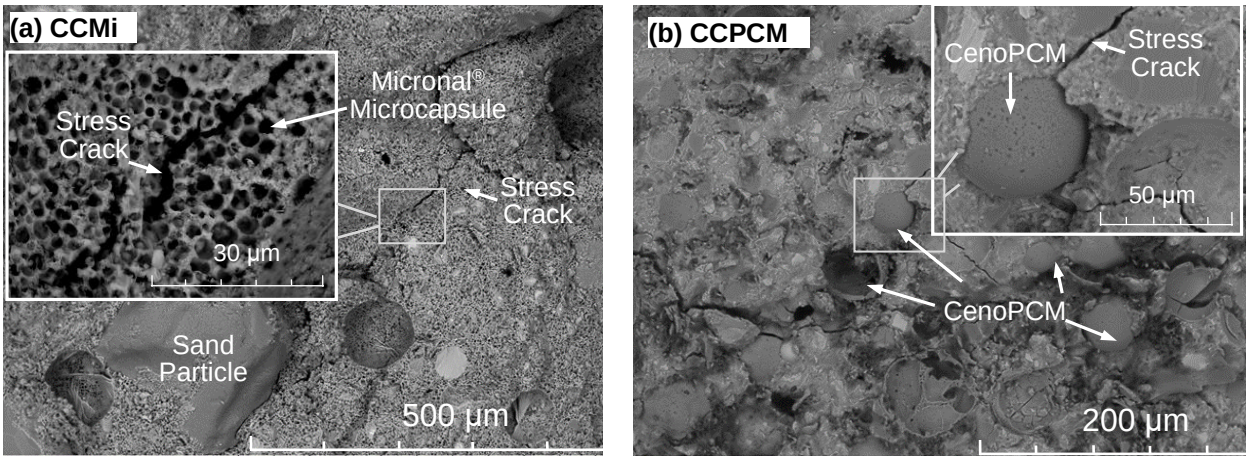

Figure 23: SEM image showing microcracking and damaged cementitious composites containing MEPCM:
(a) CCMi (with Micronal); and (b) CCPCM (with CenoPCM)

Table 7. Fracture Toughness test results

Mix ID	MEPCM Type	MEPCM Volume Fraction	Force	Disp	CMOD	a_{eff}	K_{1c}	CTODc
		v_f (%)*	(N)	(mm)	(µm)	(mm)	(MPa(m)^1/2)	(µm)
Control		0	975.37±164	0.697±0.067	9±0.1	6.146±0.046	0.650±0.107	3.8±0.01
CCMi-050		5	734.80±210	0.606±0.134	11±01.9	6.597±1.03	0.501±0.105	5.1±2.17
CCMi-100	Micronal®	10	685.07±87.3	0.719±0.066	12±1.5	5.924±0.441	0.450±0.074	4.5±1.47
CCMi-150		15	566.45±17.8	0.636±0.182	18±1.1	6.737±1.36	0.394±0.028	8.3±3.23
CCMi-200		20	510.85±72.3	0.621±0.036	16±2.3	6.696±1.21	0.353±0.018	7.4±3.16
Control2		0	855.65±66.4	0.84±0.151	10±1.5	5.72±0.401	0.563±0.025	4.7±0.2
CCPCM-050		5	1007.4±82.1	0.728±0.132	12±0.9	6.005±0.769	0.698±0.017	5.7±0.6
CCPCM-100	CenoPCM	10	726.76±112	0.802±0.111	12±2.1	6.672±2.767	0.544±0.011	6.0±3.1
CCPCM-150		15	685.15±103	0.629±0.087	11±0.6	8.082±2.628	0.496±0.013	5.1±2.1
CCPCM-200		20	561.24±33.9	0.637±0.223	11±3.4	7.542±1.12	0.406±0.056	6.7±0.5

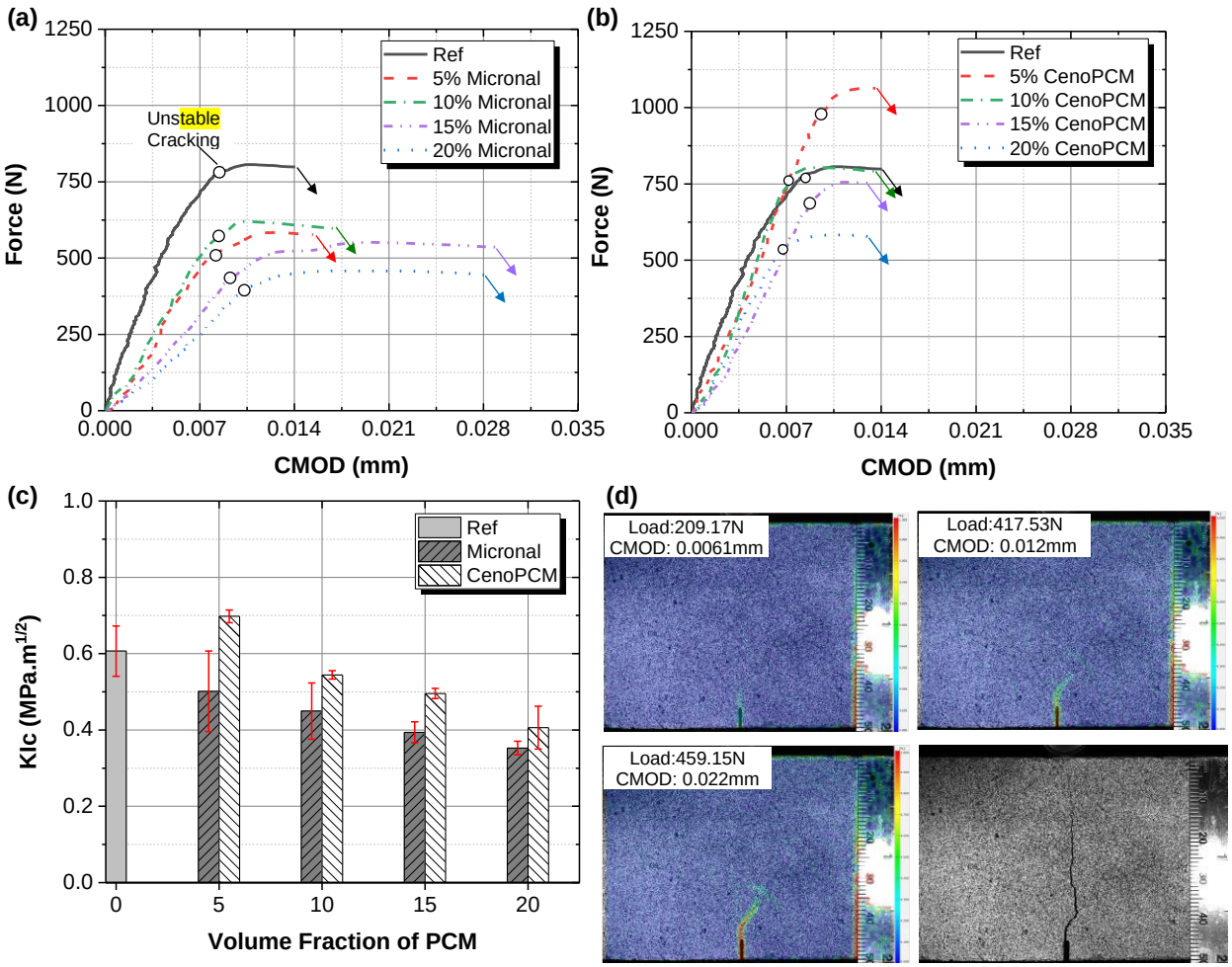

Figure 24: Results of the fracture toughness tests on cementitious composites containing Micronal® and CenoPCM:
(a) CMOD-load curves for CCMi; (b) CMOD-load curves for CCPCM; (c) comparison of K_{Ic} with various MEPCM volume loading, and (d) DIC showing the crack propagation during loading

MEPCM embedded. Overall, the fracture toughness of cementitious composite materials decreases as the MEPCM volume fraction increases (expect for CenoPCM at 5% where an increase in fracture toughness was observed. This is likely due to the decrease in air voids since lower concentrations of CenoPCM improve the workability of cement mortar. This phenomenon is discussed in an earlier work by the authors [50]). The CCPCM material shows higher fracture toughness than that of CCMi. The higher fracture toughness of CCPCM is attributed to the rigid shell of CenoPCM and good bonding strength developed between the fly-ash based CenoPCM with the cementitious matrix. It is also noted that the silica sol coating also improves the interfacial bonding strength between the CenoPCM microparticle with the cement matrix due to its pozzolanic activities. The addition of the silica-based coating also improves the durability of the functional cementitious composite, since silica reacts with the calcium hydroxide produced from the cement hydration process. The depletion of calcium hydroxide reduces its chance to react with the fatty acid. The durability of cementitious materials with fatty-acid based PCM materials will be discussed in detail in another work.

Chapter 4. Lightweight concrete containing micro-sized functional fillers

A version of this chapter was originally published by Hongyu Zhou and Adam Brooks:

Zhou, Hongyu & Brooks, Adam. (2019). *Thermal and mechanical properties of structural lightweight concrete containing lightweight aggregates and fly-ash cenospheres.* Construction and Building Materials. **198**. 512-526.

This chapter explores the effects of mix proportion, aggregate property, and microstructures on material macroscopic properties of lightweight thermally insulative concrete. Despite the studies conducted separately for LWAC and cementitious composites containing FAC (e.g., ULCC), there still lacks an understanding of the synergy between the micro-size fillers and other material phases in concrete (e.g., fine and coarse aggregates). In addition, existing research on lightweight concrete shows a significant variation regarding both mechanical and thermal properties affected by constituent materials and mix proportions [129]. Most studies to date on LWC focused either only on obtaining a material suitable for structural load-bearing purposes with high strength or as nonstructural material with low thermal conductivity. Few studies have been conducted to address the balance between mechanical properties and thermal properties [47,62,67,129].

4.1 Mixture design and material preparation

In this study, three series of normal and lightweight concrete mixtures were prepared with three binder types – i.e., normal strength (NS) cement matrix, high strength (HS) matrix with 15% cement replaced by silica fume, and HS matrix reinforced with steel fiber (SF) (20 wt% of cement, 1.49% by volume). Within each series, different aggregate types were tested with a combination of coarse and fine normal weight aggregates (NWA) and LWA. Normal weight concrete (NWC) mixtures having only NWA were tested as control groups. The LWC were designed with different size LWA to (partially) replace coarse and fine NWA. FAC was also tested as a lightweight filler to partially replace fine NWA (~50% by volume). The mix

proportions of the 14 concrete mixtures tested are listed in Table 8, and the dry density tested in this study ranges from 1421 kg/m^3 to 2488 kg/m^3.

The binder material used for preparing the concrete consists of ASTM Type I-II Portland cement and silica fume, see Figure 25. The water to cementitious material ratio was selected at 0.35 for normal strength mixtures and 0.27 for high strength mixtures. A polycarboxylic ether-based superplasticizer (*Sika*) was used to adjust the workability. The lightweight aggregates (both coarse and fine) used here are commercially available products manufactured from expanded clay in the Southeast of the US (*Trinity Lightweight*). These LWA contain a number of close-cell air pores (cellular structure), as can be seen in Figure 26. The porosity and pore-size distribution within the LWA were measured using mercury intrusion porosimetry (MIP). The LWA have moderate specific densities (~830 kg/m^3) and relatively high mechanical strength, which make them suitable for producing structural lightweight concrete. Ground quartz flour, with the density of 2650 kg/m^3, was used as filler to adjust the powder amount and reduce the air content within the mortar. Fly-ash cenospheres (FAC), with average particle size of 81 μm and particle density of 910 kg/m^3 were used as lightweight functional filler to partially replace fine NWA and induce micrometer-size air cell in the cementitious matrix. Steel fiber (*Nycon*), with 0.2 mm diameter and 13 mm length was investigated as reinforcements for the high strength LWC.

The particle size, gradation, and other physical properties of aggregates are shown in Figure 27 and Table 9. X-ray diffraction (XRD) analysis performed on the RiverLite^{TM} LWA indicates that the material is primarily comprised of amorphous materials and crystalline minerals including quartz, spinel, and millosevichite, see Figure 27 (a). Since water absorption of

Table 8. Test matrix and mix proportions (by weight, kg of materials/ m^3 of concrete)

Mix ID*	Binder		Water	W/ (C+F)	FAC	Quartz Flour	Steel Fiber	Silica Sand	Gravel (Lime Stone)	Lightweight Aggregate**	
	Cement	Silica Fume								RiverLite™ (Fine)	RiverLite™ (Coarse)
NS-SS-G	437.4	--	153.2	0.35	0.0	--	--	734.7	874.7	--	--
NS-FAC/SS-G	437.4	--	153.2		96.0	--	--	410.2	874.7	--	--
NS-FAC/RLF-G	437.4	--	153.2		96.0	--	--	0.0	874.7	216.5	--
NS-SS-RLC	437.4	--	153.2		0.0	--	--	734.7	0.0	--	377.0
NS-FAC/SS-RLC	437.4	--	153.2		96.0	--	--	410.2	0.0	--	377.0
NS-FAC/RLF-RLC	437.4	--	153.2		96.0	--	--	0.0	0.0	216.5	377.0
HS-SS-G	489	86.3	155.3	0.27	--	253.3	--	431.2	816.7	--	--
HS-FAC/SS-G	489	86.3	155.3		107.3	141.5	--	234.3	816.7	--	--
HS-SS-RLC	489	86.3	155.3		--	253.3	--	431.2	--	--	355.8
HS-FAC/SS-RLC	489	86.3	155.3		107.3	141.5	--	234.3	--	--	355.8
HS-SS-G-SF	481.5	85.0	153.0	0.27	--	249.4	116.1	424.7	804.4	--	--
HS-FAC/SS-G-SF	481.5	85.0	153.0		105.7	139.4	116.1	230.7	804.4	--	--
HS-SS-RLC-SF	481.5	85.0	153.0		--	249.4	116.1	424.7	--	--	350.4
HS-FAC/SS-RLC-SF	481.5	85.0	153.0		105.7	139.4	116.1	230.7	--	--	350.4

* NS- – Normal strength cement binder; HS- – High strength cement binder with silica fume and lower water to binder ratio;
SS – Silica Sand; G – Natural limestone gravel; RLC – RiverLite™ Coarse LWA; RLF – RiverLite™ Fine LWA; -SF – Steel fiber reinforced;
FAC/SS – 50% of fine NWA are replaced by FAC; FAC/RLF – fine aggregates are only comprised of FAC and RLF.

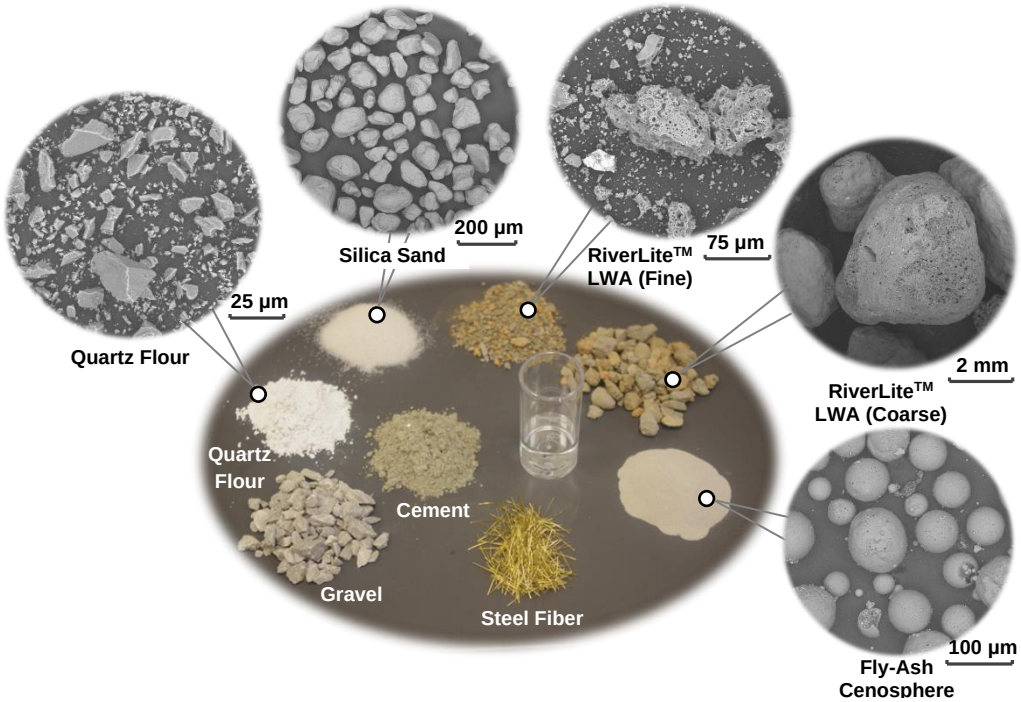

Figure 25: Common ingredients within structural lightweight concrete

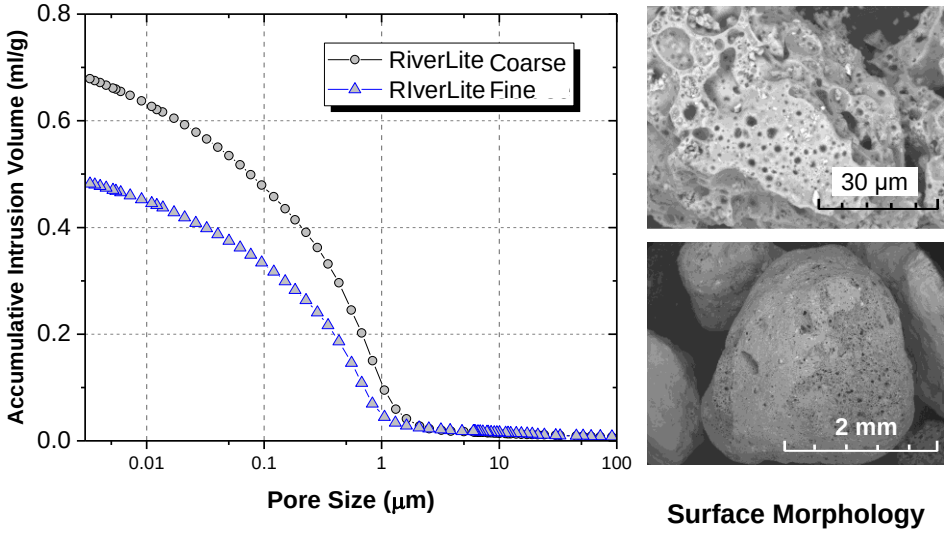

Figure 26: The mercury intrusion porosimetry (MIP) test and SEM imaging performed on RiverLite™ LWA

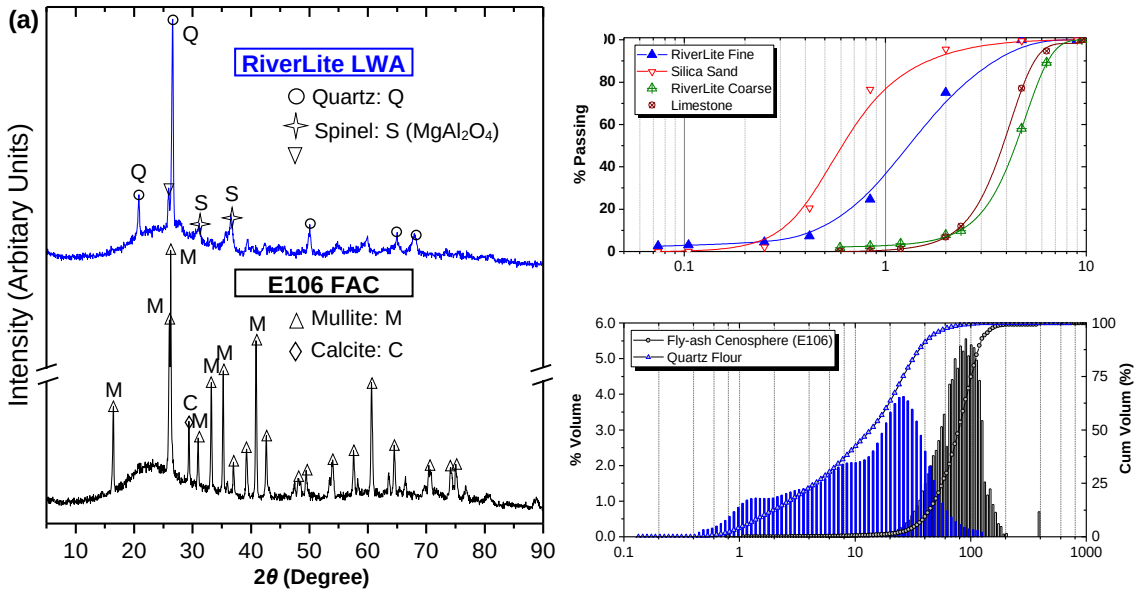

Figure 27: Characterization test performed on aggregates:
(a) XRD spectrum for LWA and FAC; and (b) particle size analysis results and gradation

LWA is an influential factor in the lightweight aggregates concrete design and production – i.e., if mixed in dry condition the LWAs normally absorb a certain amount of free water from the fresh mixture. Therefore, the LWAs were immersed in water for 24 hours until reaching saturation. The aggregates were then drained on a US #30 standard sieve with periodic mechanical agitation (shaking) for 3-4 hours until they reach surface dry (SD) condition before mixing – i.e., the SD conditions for both coarse and screened-fine LWA were determined according to ASTM C127-15 and ASTM C128-15 specifications, respectively. The specific densities of LWA were also measured under SD condition for the mix proportion design, see Table 9. The cenospheres used in this research have particle sizes up to 106 μm (*E106, CenoStar*). XRD analysis performed on the FAC (Figure 27 (a)) indicated that the cenospheres are comprised primarily of amorphous materials with small amounts of mullite and calcite. The particle size distribution of cenosphere particles was analyzed using a laser diffraction particle size analyzer (*Horiba LA-950*) and the results are plotted in Figure 28 (b).

4.2 Experimental setup for mechanical tests

The mechanical tests were performed using a 500 kN MTS-810 servo-hydraulic universal testing system as shown in Figure 29 (a). Five 101.6 mm (4 inches) diameter by 203.2 mm (8 inches) cylinders were tested for each specimen group listed in Table 8. The mechanical loading procedure was carried out in a displacement-control mode at the loading rate of 0.01 mm/min. The deformation (i.e., compressive strain) of test cylinders was measured using a pair of clamp-on extensometers (*Epsilon Tech*) with gauge length of 50 mm. The extensometer pair was clamped onto the specimen to measure the strains on both sides of the cylinder. The setup of extensometers is shown in Figure 29(b).

Table 9. Aggregate properties

	Particle Size*			Bulk Density**	Specific Density	Porosity* **	Thermal Conductivity ****
	D_{10}	D_{50}	D_{90}				
		um		kg/m^3	kg/m^3	Vol %	W/mK
Silica Sand	300	600	1350	1497 (1673)	2650	--	4.0
Quartz Flour	1.60	13.6	38.6	867 (1066)	2650	--	5.5
Fly-ash Cenosphere (E106)	42.6	81.3	125.2	394 (442)	910	--	--
Steel Fiber	--	--	--	--	7850	--	54
Limestone	2150	3800	6200	1414 (1551)	2570 (2610)*	--	3.03
RiverLite™ LWA (coarse)	2200	4300	5300	514 (556)	830 (1150)*	57.9	0.190
RiverLite™ LWA (Fine)	440	1250	3400	709 (787)	830 (1150)*	49.15	0.190

* The specific density of coarse aggregates is reported in both oven-dry and saturated surface dry conditions according to ASTM C127 and C128 specifications;

** Bulk density is reported both in loosely packed and (vibrated) states.

*** The porosity of LWA is tested using mercury intrusion porosimetry (MIP).

**** Thermal conductivities of aggregates were tested using transient plane source method (ISO22007) , also see Figure 24 (c).

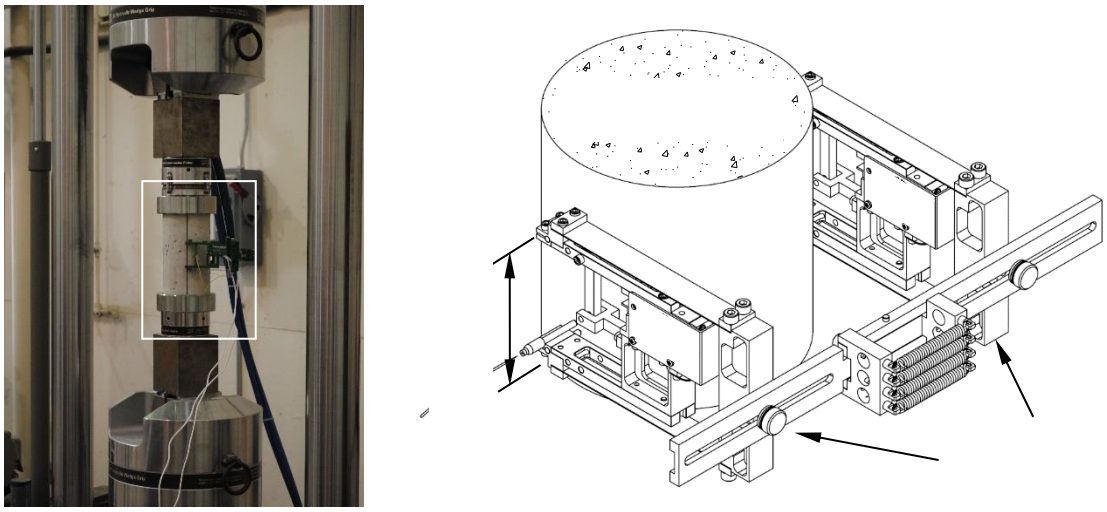

Figure 28: Mechanical test setup:
(a) picture showing the compressive cylinder used to determine mechanical properties; and (b) setup of extensometers for Young's modulus measurement

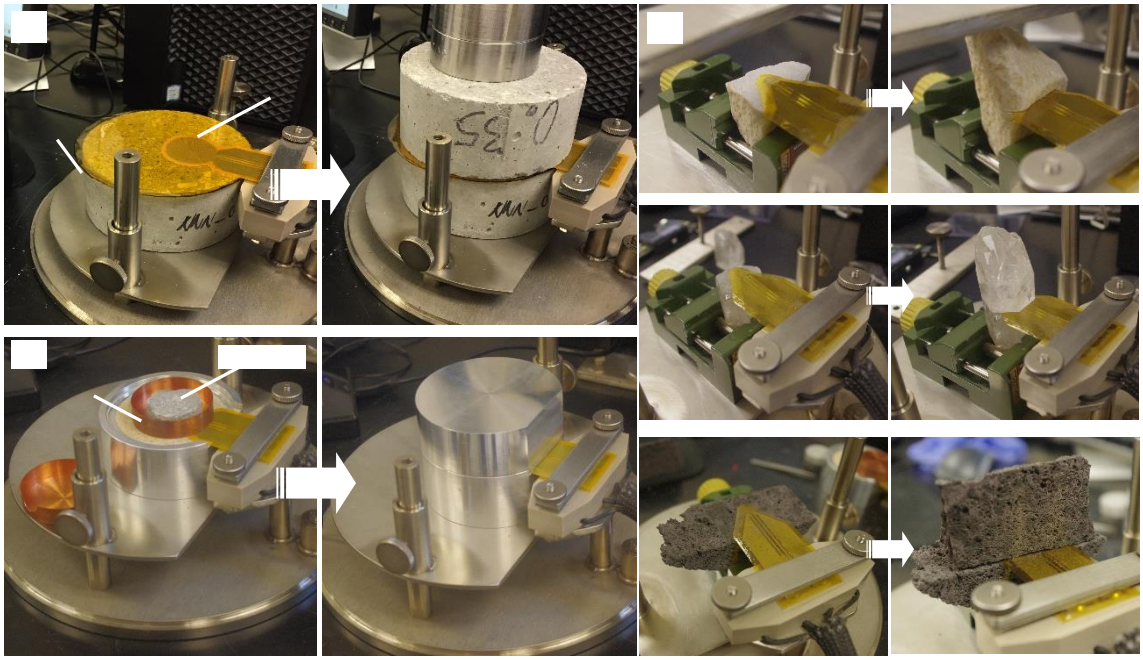

Figure 29: The Transient Plane Source (TPS) method for thermal constants analysis: (a) TPS measurement on concrete samples; (b) specific heat capacity measurement; and (c) TPS test setup for aggregates: gravel (limestone), silica sand (quartz), and LWA (sintered expended clay).

A high resolution CCD camera was staged to record the damage and failure of the specimens. The tested specimens were preserved for scanning electron microscopy (SEM) analysis.

4.3 Thermal property measurement using transient plane source (TPS) method

The transient plane source (TPS) method originally developed by Gustafsson [121] was applied to measure the thermal properties of the aggregates (see Table 9) and concrete. The TPS technique is based on the recorded temperature rise of a plane source that heats the surrounding material to be measured. In a TPS test, a conducting pattern with negligible heat capacity (e.g., Kapton supported double spiraled nickel metal sensor as shown in Figure 30(a)) serves simultaneously as the heat source and the temperature sensor.

While the specific heat capacity of the tested materials can be deduced from the thermal conductivity k and the thermal diffusivity κ as outlined by Equation (3) using a single set of TPS data, a more reliable method for measuring materials' specific heat capacity was developed [130]. In a specific heat measurement, a TPS sensor is attached to the underside of a conductive sample holder made of gold or copper and disc shape samples with 25 mm diameter and 10 mm height is used for the specific heat measurement. The process of measuring is based on two individual measurements; a reference measurement (the empty container) and a sample measurement (the container while holding a sample). In order to minimize the heat losses to ambient air, the setup of the sensor, sample holder and the sample to be measured are all encased in a thermal insulating chamber, see Figure 30(b). The method is based on the assumption of a linear temperature increase – i.e., the heat losses to the surroundings are assumed negligible for the time span of the measurement. The heat capacity would be calculated by Equation (3) as for the adiabatic calorimetry [130]:

Equation 11: Heat capacity

$$mc_p = \frac{\Delta E}{\Delta T} = \frac{\int_{t_2}^{t_2} V(t) I_0 dt}{\Delta T}$$

where m is the sample mass, c_p is the specific heat capacity, and ΔT is the temperature change. It is noted that to find the right time span for the analysis, the measurement data could be analyzed in a variety of time windows. The results will give a curve with a maximum that is close to the specific heat of the analyzed material [130].

For thermal conductivity measurements, three pairs of disc shaped concrete samples (100 mm diameter and 25 mm thick) were prepared. The TPS tests were performed using a *HotDisk TPS-1500* thermal constant analyzer with a 29.22 mm diameter TPS sensor according to the ISO22007-2 specifications [104]. The sensor size is in accordance with the guidelines set out for heterogeneous samples with grain size up to 10 mm. The applicable thermal conductivity testing range of the equipment was 0.01-400 W/m K. In addition, 25 mm diameter 9 mm tall disc shape concrete samples were machined for specific heat capacity measurements. The sample size is comparable with the maximum aggregate size used in the concrete. All samples were dried in a convection oven for 48 hours and cooled down to room temperature in an air-tight desiccant cabinet to prevent surface condensation. The thermal conductivity of aggregates – i.e., silica sand (quartz), gravel (limestone), and sintered expanded clay (lightweight RiverLite^{TM} coarse and screened fine) were tested from their corresponding parent materials provided by the material producer using the TPS setup, see Figure 29(c).

4.4 Mechanical properties

The densities, mechanical and thermal test results for the concrete mixtures tested are summarized in Table 10. The influence of LWA replacement on concrete mechanical behaviors

*Table 10. Experimental results**

Mix ID	Wet Density**	Oven-Dry Density	Young's Modulus	Compressive Strength	Thermal Conductivity k	Thermal Diffusivity κ	Volumetric Heat Capacity (by TPS)***	Volumetric Heat Capacity (Direct measure)
	kg/m^3	kg/m^3	GPa	MPa	W/mK	mm^2/s	kJ/m^3	kJ/m^3
NS-SS-G	2311	2185	27.07	59.69	1.817	0.954	1904	1902
NS-FAC/SS-G	2177	2039	25.77	46.77	1.386	0.920	1729	1875
NS-FAC/RLF-G	2038	1880	19.38	51.07	1.026	0.674	1522	1806
NS-SS-RLC	1801	1614	15.28	39.11	1.050	0.717	1464	1529
NS-FAC/SS-RLC	1666	1507	12.57	39.10	0.739	0.485	1523	1360
NS-FAC/RLF-RLC	1421	1224	8.84	33.39	0.423	0.334	1267	1130
HS-SS-G	2419	2259	19.93	66.55	1.923	0.964	1995	2031
HS-FAC/SS-G	2204	2063	20.93	60.67	1.437	0.752	1911	1941
HS-SS-RLC	1916	1770	16.50	56.66	1.074	0.709	1514	1585
HS-FAC/SS-RLC	1673	1519	13.18	43.86	0.706	0.473	1492	1412
HS-SS-G-SF	2488	2387	30.83	127.53	2.105	0.972	2165	2370
HS-FAC/SS-G-SF	2360	2228	28.87	100.09	1.607	0.759	2118	1921
HS-SS-RLC-SF	1995	1827	17.51	60.10	1.348	0.786	1714	1603
HS-FAC/SS-RLC-SF	1770	1634	14.36	54.28	0.885	0.564	1570	1447

* Results are presented as the statistical average of measurements on five specimens. The stand deviations are shown as error bars in Fig. 6 and Fig. 7.

** Wet density was measured immediately after when concrete was poured.

***The volumetric heat capacity deducted from the thermal conductivity and thermal diffusivity obtained from a TPS measurement through equation $c_v = k / \kappa$.

can be estimated by the relations of concrete mechanical properties to its density. Figure 30 plots the concrete compressive strength and Young's modulus against the materials' oven dry density. The density is presented in descending order so that the influence of the density decreasing on mechanical properties is displayed. In general, the compressive strength and Young's modulus decrease with concrete density. While at the same density, the concrete might have different compressive strength depending on the strength and type of binder materials used. For similar density, the LWC with steel fiber reinforced high strength binder (HS-xxx-xxx-SF) shows the highest compressive strength. The higher strength matrix provides higher rigidity and strength while steel fiber reinforcements greatly enhance the materials' ability to resist mechanical damage [131].

Nevertheless, the decrease of compressive strength with respect to density is at a substantially higher rate (-9.72 MPa per 100 kg/m^3 decrease in density) for the HS-xxx-xxx-SF group, when replacing the NWA with LWA, than that of the group with normal strength binders (NS-xxx-xxx) (-2.49 MPa per 100 kg/m^3 decrease in density), see Figure 30 (a). This is attributed to the more brittle nature of the higher strength matrix – i.e., the introduction of a weak lightweight phase would promote the initiation and faster propagation of stress cracks. Further discussion on the microscopic damage is provided in greater detail later in Section 3.2. The results show that, at a density around 1600-1800 kg/m^3, the compressive strength of LWC becomes insensitive to the use of steel fiber reinforcement. The elastic modulus, on the other hand, is roughly proportional to the material density regardless of the aggregates and binder type, Figure 30 (b). The substitution of NWA by FAC and LWA leads to an elastic moduli decrease of 0.2 GPa for every 100 kg/m^3 density decrease.

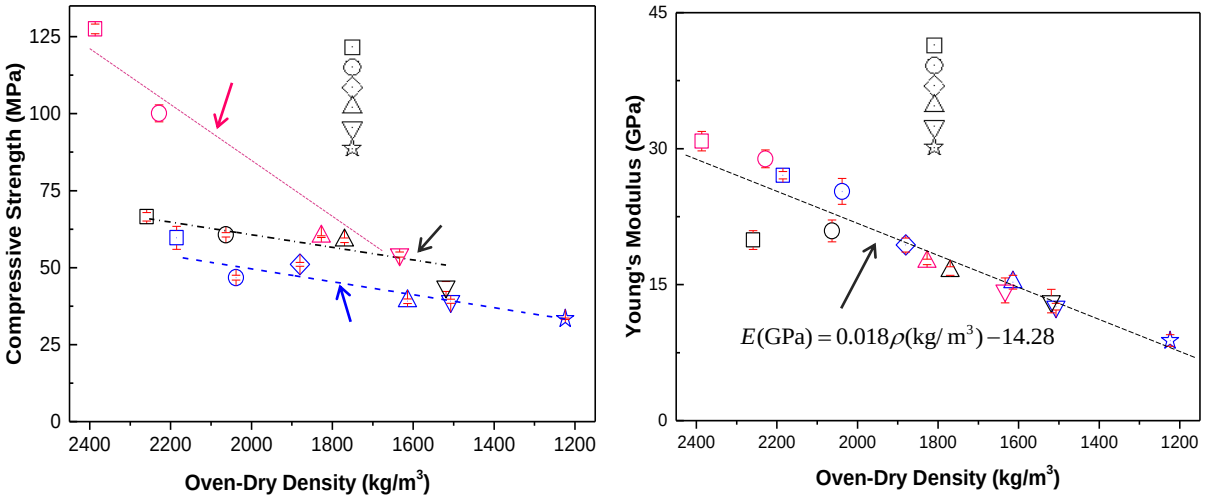

Figure 30: Mechanical property relationships:
(a) compressive strength and (b) Young's modulus and concrete oven-dry density (error bars indicate the standard deviations of the test results).

4.5 Thermal properties

The thermal conductivity, specific heat capacity, and thermal diffusivity tested by the TPS method are summarized in Table 10, and the thermal conductivity and specific heat capacity are plotted against material density in Figure 31. The thermal conductivity of building materials affects the heat transmission resistance of building components (i.e., R-value); while specific heat and density dictate their capabilities to store thermal energy and are important for building energy consumption and thermal comfort under transient conditions. Figure 32(a) and (b) show the relationship between concrete density and thermal properties. Thermal conductivity of tested LWAC depends on aggregate porosity but also on their mineralogical compositions [132]. XRD analysis performed on the expanded clay LWA and FAC indicates that they both contain crystalline minerals such as quartz, calcite and mullite, see Figure 28(a). Thus, the porosity brought by LWA and FAC makes the thermal conductivity of concrete decrease almost linearly with the decrease of material density. With respect to the decrease of the concrete density, the thermal conductivities of concretes made of normal and high strength binders decrease at a similar rate. It is noted that the thermal conductivities tested in this research are in general higher than the density based thermal conductivity equation proposed by Valore [133,134] and as shown in Figure 32(a) where tested values are compared with the ACI 122 equation [135]. This is as expected since the lower W/C ratio used in modern concrete leads to higher thermal conductivity of the mortar matrix and the aggregates used nowadays contain large amount of quartz and other crystalline minerals that have high conductivities (4 to 12 W/m K [136]). Figure 32(b) shows that the volumetric heat

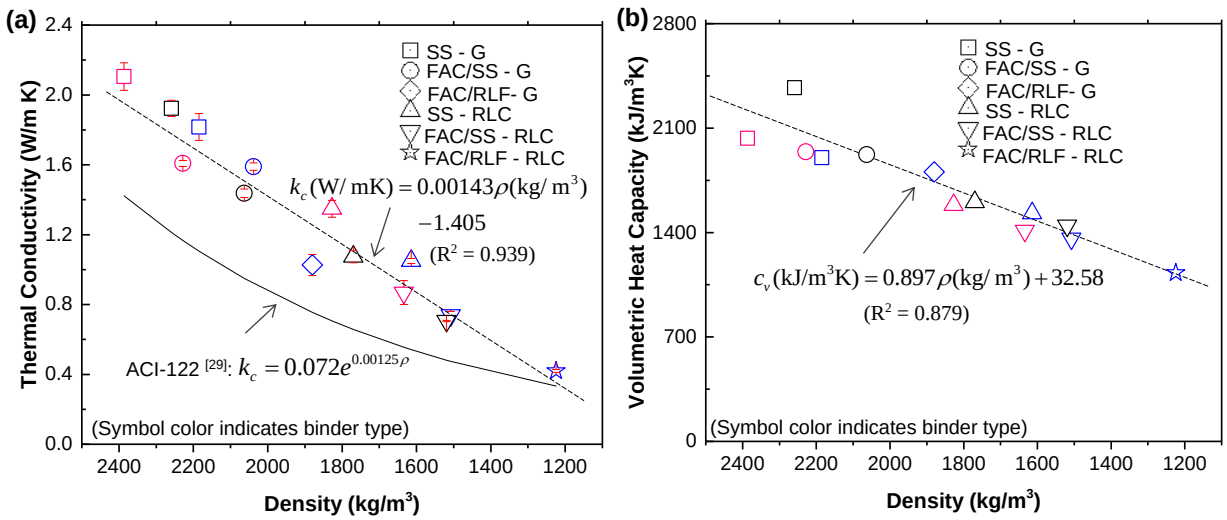

Figure 31: Thermal properties of LWCC tested through Transient Plane Source (TPS) method:
(a) thermal conductivity; and (b) Volumetric heat capacity

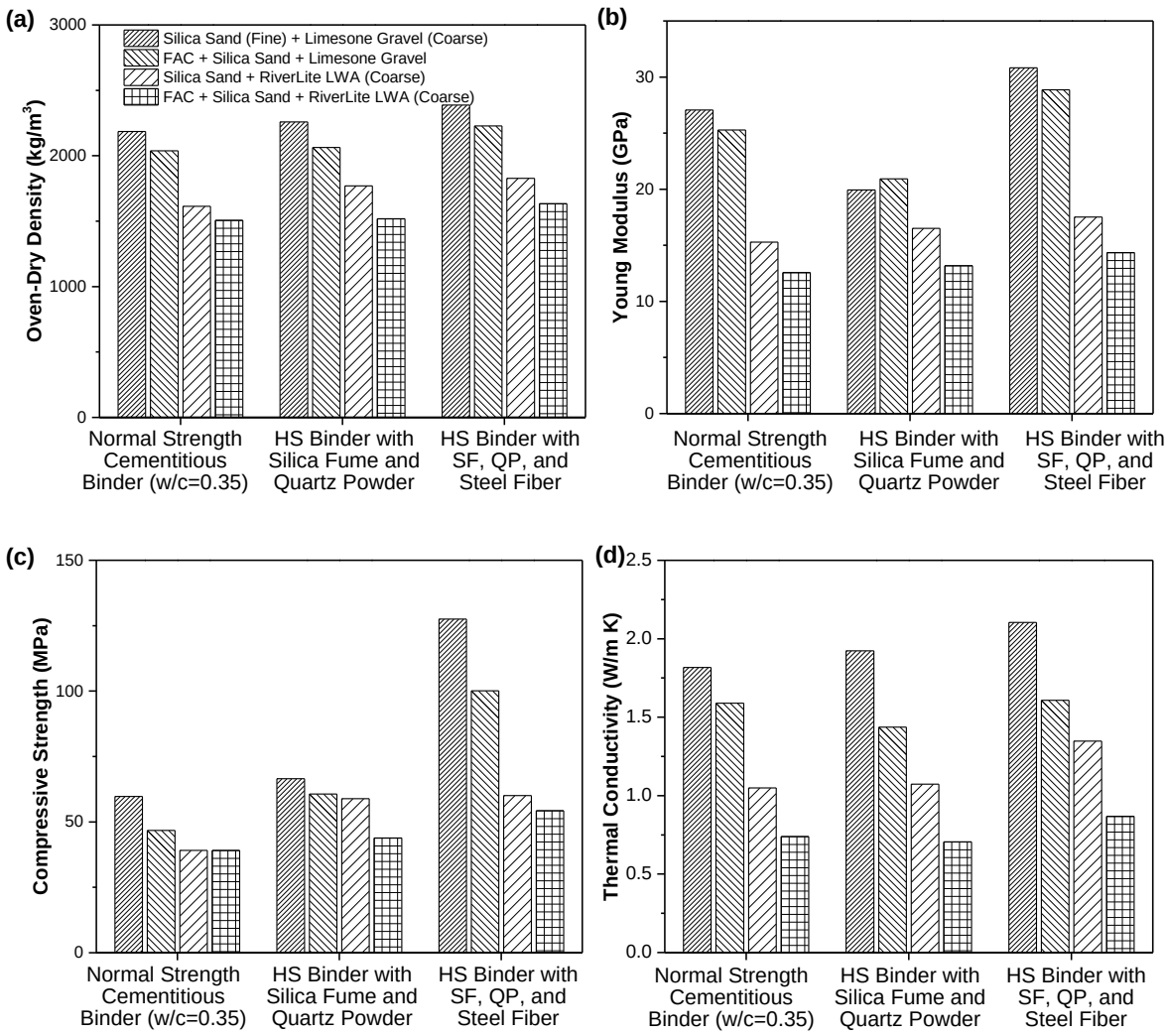

Figure 32: Effect of aggregates and binder materials: (a) oven-dry density; (b) Young's modulus; (c) compressive strength; and (d) thermal conductivity

capacity decreases proportionally with the decrease of concrete density, i.e., the specific heat of LWC is similar to that of NWC. The thermal diffusivity, κ, is combination of thermal conductivity k and specific heat c_p: $\kappa = k/(\rho c_p)$, where ρ represents the density of the material. Thus, the thermal diffusivity variation with respect to density are similar to that of the thermal conductivity, see Table 10.

4.6 Effects of aggregates and binder materials

Figure 33 shows the effect of NWA substitution by FAC, fine LWA, and coarse LWA on concrete density, mechanical and thermal properties. High strength concrete with NWA and steel fiber has higher density (7.6%) than the NWC control specimen. Replacement of NWA by LWA decreases the concrete density and influences the properties of concrete, see Figure 32 (a). The partial replacement (56% by volume) of fine NWA with FAC reduces the concrete oven-dry density by approximately 6-8%; further replacement of the fine NWA by fine graded expanded clay (*RiverLite*) reduces the density by an additional 7-9%; 100% replacement of coarse NWA by LWA (*RiverLite*) reduces the concrete density by about 20%; thus, complete replacement of all NWA with FAC and LWA reduces the density by 35% (to about 1400 kg/m^3), see Table 10. The experimentally tested densities matched well with the values calculated from the mixture composition.

The substitution of coarse NWA by coarse LWA leads to 42% decrease in Young's moduli and 15-50% decrease in compressive strength depending on the binder type as shown in Figure 32 (b) and (c) respectively. Then the partial substitution of fine NWA by fly-ash cenospheres (FAC) leads to an additional decrease of 0.2–5.1 MPa and 1.3–2.5 GPa per every 100 kg/m^3 density decrease for the compressive strength and the

modulus of elasticity, respectively. The compressive strength and elastic modulus decrease at faster rates when NWA are substituted with FAC and LWA for concrete having higher binder strength (i.e., cementitious matrix with silica fume and steel fiber).

Figure 32 (d) shows the effect of NWA substitution on the thermal conductivity of LWC. The thermal conductivity of LWC at 100% coarse NWA replacement decreases from 36% to 45%. The values of thermal conductivity vary from 1.0 to 1.37 W/m K. Further replacement of fine NWA with fly-ash cenospheres leads to an additional 20-25% decrease in thermal conductivity, i.e., the LWC with coarse LWA and 50% sand replaced by FAC have conductivities around 0.71-0.85 W/m K, which are about 35-40% of NWC conductivity (1.82-2.11 W/m K). The volumetric heat capacity, c_v, of concretes tested are roughly proportional to the material density, see Figure 31 (b). The specific heat, c_p, of the aggregates used in this research are in similar range – i.e., LWA, FAC, and limestone are tested at 675 J/kgK, 658 J/kgK, and 750 J/kgK, respectively under oven-dry condition.

4.7 Microstructures and damage

The microstructural characterization was carried out using both optical and scanning electron microscopic (SEM) imaging. The concrete and mortar samples for microstructural analysis were resin-impregnated using epoxy, and the resin mounted samples were then ground and polished using a *Buehler EcoMet* grinder/polisher to 0.3 μm diamond paste. Some polished samples were then carbon-coated to a thickness of approximately 10 nm to prevent charging under the electron beam. SEM imaging was conducted using a *Hitachi TM1000* at accelerating voltage of 15 kV. To analyze the

fracture surfaces of the mechanically tested samples, fragments of the tested compression cylinders were preserved for SEM imaging analysis.

Figure 33 (a)-(d) present the optical microscopic images of LWC with coarse NWA and 100% substitution of fine NWA with FAC and fine-graded LWA, LWC with coarse LWA and fine NWA, LWC with coarse LWA and 50% substitution of fine NWA by FAC, and LWC with coarse LWA and 100% substitution of fine NWA with FAC and fine-graded LWA, respectively. The corresponding densities and compressive strengths obtained for these LWCs are 1880 kg/m^3 (51.1 MPa), 1614 kg/m^3 (39.1 MPa), 1507 kg/m^3 (39.1 MPa), 1224 kg/m^3 (33.4 MPa), respectively. The substitution of NWA with FAC and LWA leads to lower thermal conductivities. The heat conduction in porous material results from the thermal conductivity of the solid phase of aggregate (minerals) and that of the gas or fluid phase contained in the pores. Substituting NWA in concrete by FAC and LWA leads to an increase of the voids in the concrete. Consequently, the conduction surface of the solid phase decreases whereas that of the gas phase increases. For mixes having similar density, lower thermal conductivities were tested for samples with NWA substituted by FAC and fine-graded LWA. This is consistent with the theory of Maxwell-Eucken limits [137]. For materials that are 'externally porous', where the continuous phase has lower thermal conductivity than the dispersed phase, see Figure 33 (a) and Table 9 for the thermal conductivities of each constituent phase, the heat does not have a continuous path through the more conductive phase (natural NWA); whereas an "internally porous" material consists of a continuous phase that has higher thermal conductivity than that of the dispersed phase (Figure 33(b)). In this case, the continuous

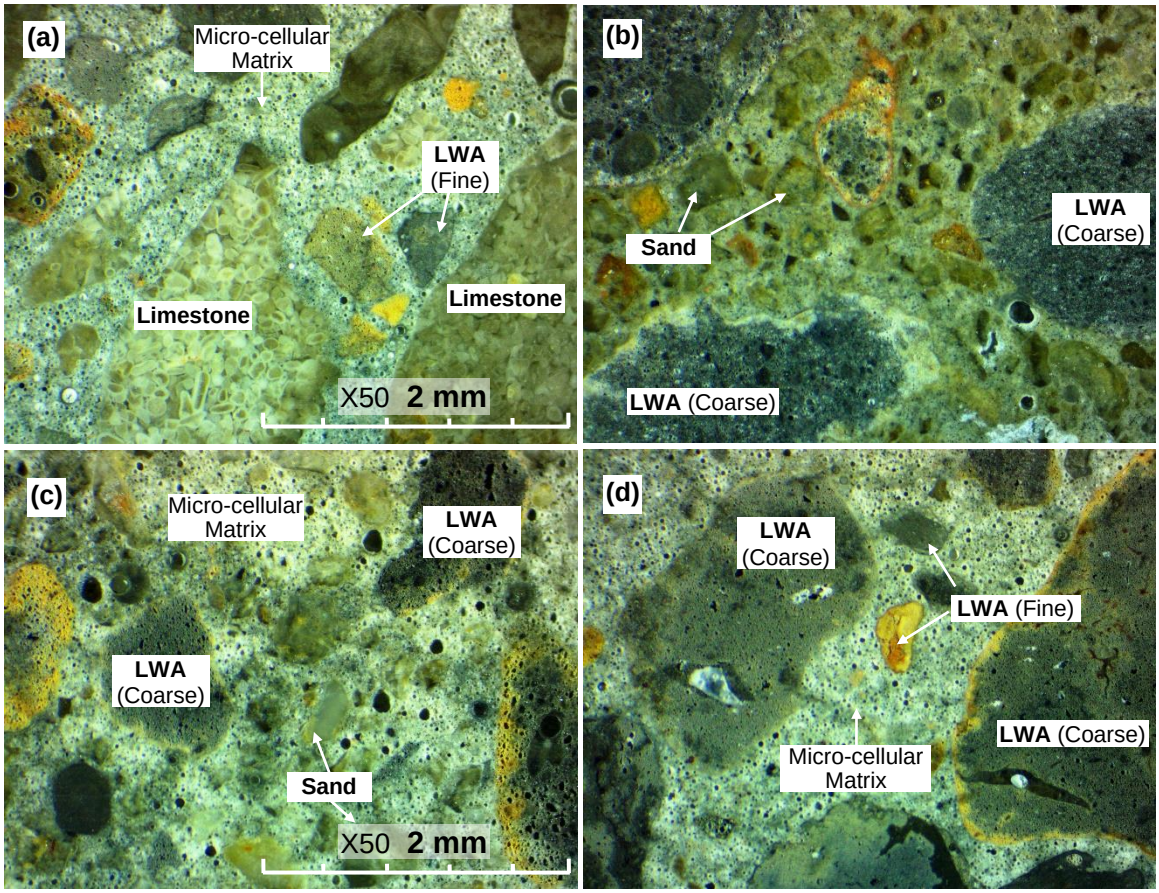

Figure 33: Optical microscopic images of lightweight aggregate concrete: (a) NS-FAC/RLF-G (Fine NWA replaced by FAC and fine LWA); (b) NS-SS-RLC (Coarse NWA replaced with LWA); (c)NS-FAC/SS-RLC (Partial replacement of Fine NWA with FAC and NWA Coarse replaced with LWA); and (d) NS-FAC/RLF-RLC (complete replacement of NWA with FAC, fine LWA, and coarse LWA)

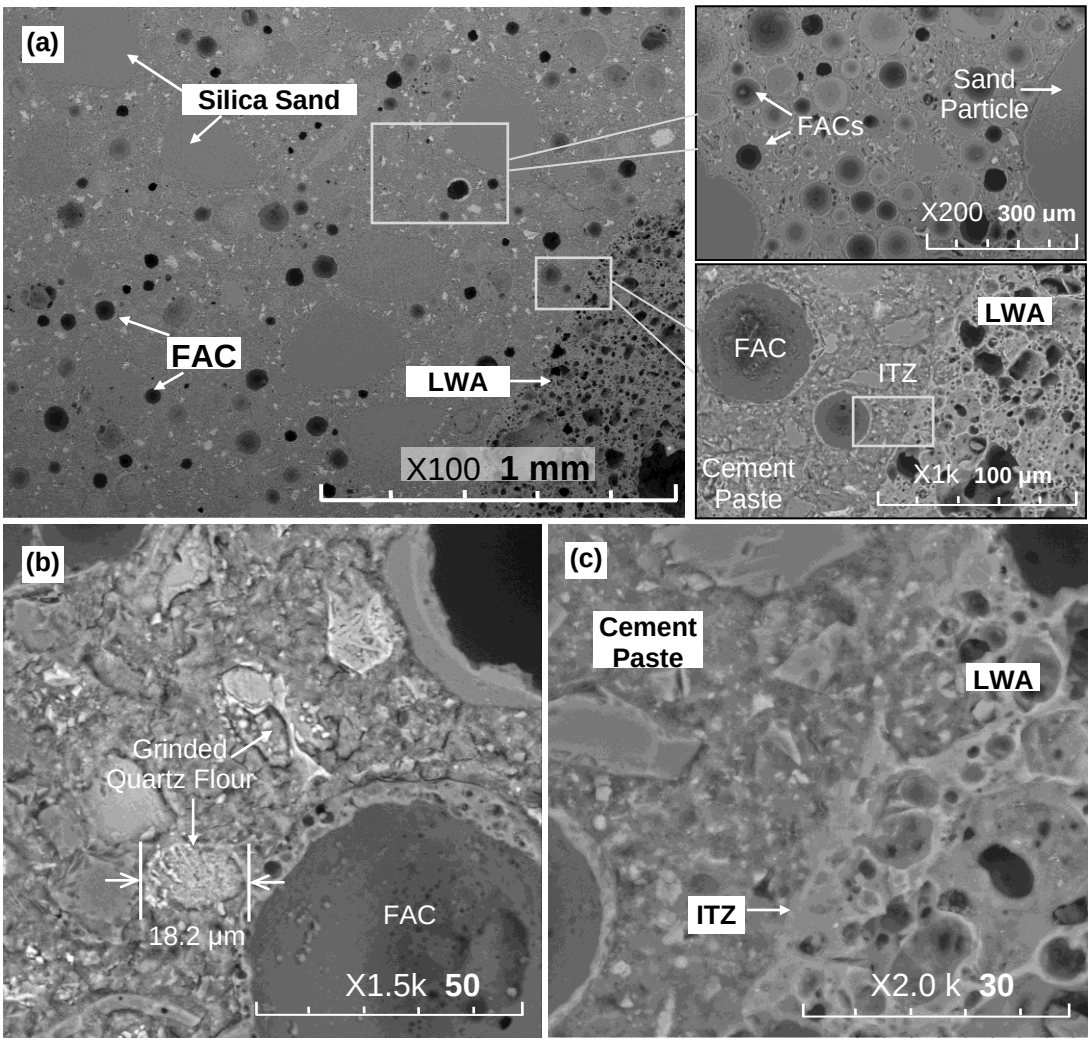

Figure 34: SEM image showing the hierarchical microstructure the FAC-filled micro-cellular cementitious matrix and LWA

phase forms an uninterrupted pathway through the material. Holding all other variables constant, concrete that is externally porous has lower thermal conductivity than that it was internally porous [138]. Thus, inducing micro air-cells into the cement matrix via FAC leads to faster decrease in thermal conductivity than replacing coarse NWA with LWA. The lowest thermal conductivity is obtained for LWC with all NWA substituted by FAC and LWA at 0.42 W/m K, which is only about 25% of that of NWC (1.8-2.0 W/m K), see Figure 32 (d).

Figure 34(a) shows the hierarchical microstructure of LWC with FAC-filled micro-cellular cement binder and LWA. For concrete with the high strength (HS) binder, the addition of fine-ground quartz flour and lower W/C lead to an increase in thermal conductivity. The average particle sizes of coarse aggregate, silica sand (fine NWA), fly-ash cenosphere (FAC), and quartz flour (Figure 34 (b)) are 4 mm, 0.6 mm, 81 μm, and 14 μm, respectively. The sizes of these filler/ aggregate materials are distributed across a wide range along the length scales. Thus, smaller size particles within the mixture can be packed in the void volume among larger size particles. The packing of different size filler/ aggregates decreases the tendency of segregation and reduces air voids, which will lead to better mechanical performance of the concrete. The polished section of LWC confirmed that all material phases are well distributed despite their large differences in density. Since most air pores in the LWA used are closed-cell pores, only a small amount of cement paste penetrated into LWA during mixing, see Figure 34 (c). This penetration of fresh cement paste into the surface pores of LWA enhances the interfacial transition zone (ITZ) and may contribute to the improvement of mechanical properties.

The fracture surfaces of the compressive cylinders used for the mechanical testing were also examined using SEM. Figure 35 (a)-(d) present the fracture topographical images of NWC, LWC with coarse NWA substituted by coarse LWA, LWC with fine NWA substitute by FAC and fine LWA, and LWC with 100% substitution of fine and coarse NWA, respectively, all containing NS binder.

It is evident that the damage modes of materials at microscopic scale are different for LWC with the various aggregate/filler types. For NWC containing only NWA, stress cracks tend to initiate and develop within and along the interfacial transition zone (ITZ). While the fracture of coarse NWA (limestone gravel) were observed for NWC, cracks normally propagate along the ITZ between fine NWA and the cement paste, see Figure 35(a). For LWCs containing LWA, stress cracks normally propagate through the porous LWA, see Figure 35 (b) and (c). Whereas for LWC with FAC and fine LWA, the stress cracks normally propagate through fine LWA and along the ITZ between coarse NWA and the matrix, see Figure 35 (c). Examination of the fracture surface indicates that many coarse NWA in this type of LWC exhibit 'pull-out' failure. As a result, for concrete with similar density, the materials with fine NWA substituted by FAC and fine graded LWA exhibit more ductile behavior than the ones having coarse LWA. Figure 36 presents the stress-strain curves obtained for representative samples within each material group, where Figure 36 (a) shows the test setup and Figure 36 (b), (c), and (d) show the stress-strain curves for concretes with normal strength binder (NS-xxx-xxx), high strength (HS-xxx-xxx), and steel fiber reinforced high strength binder (HS-xxx-xxx-SF), respectively. In addition, LWC containing fly ash cenospheres (FAC) generally exhibit good

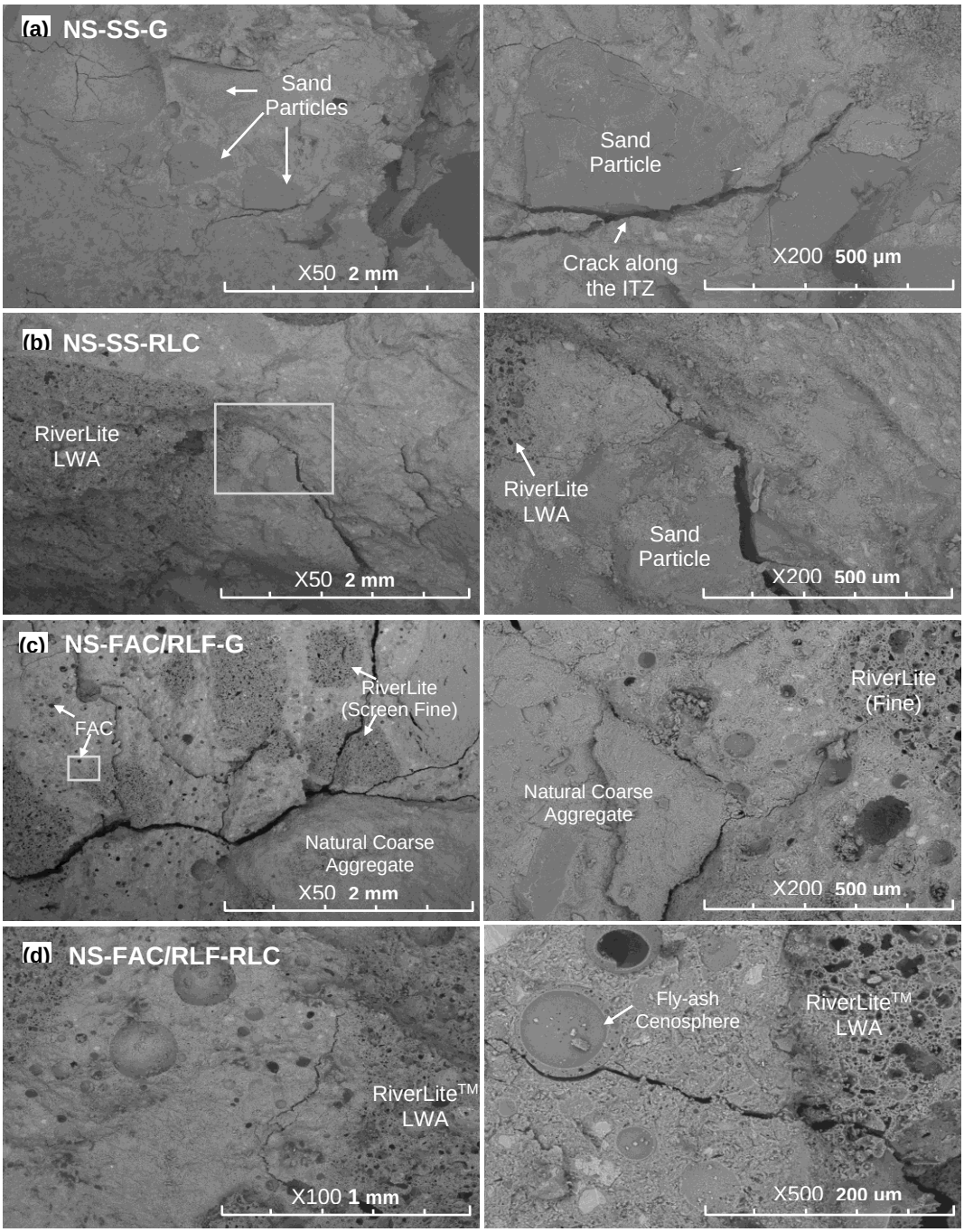

Figure 35: Fracture topographic images:
(a) NWC (reference); (b) LWC with coarse LWA; (c) LWC with fine NWA substitute by FAC and fine LWA; and (d) LWC with 100% substitution of fine and coarse NWA

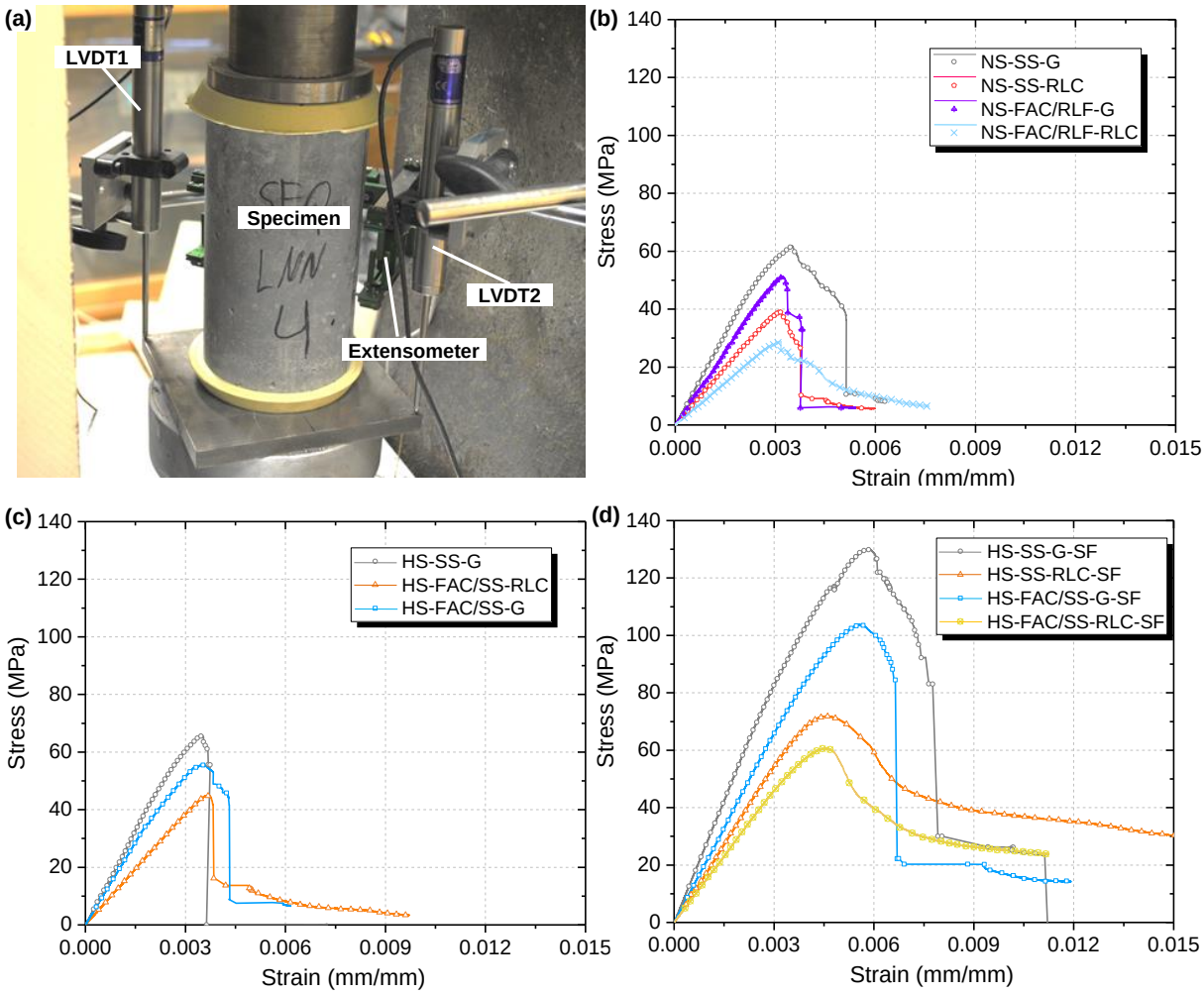

Figure 36: Stress-strain behavior:
(a) experimental test setup; representative stress-strain curves of (b) concrete with normal strength binder; (c) concrete with high strength binder (low w/c + silica fume + quartz powder filler); and (d) concrete with high strength binder reinforced with steel fiber

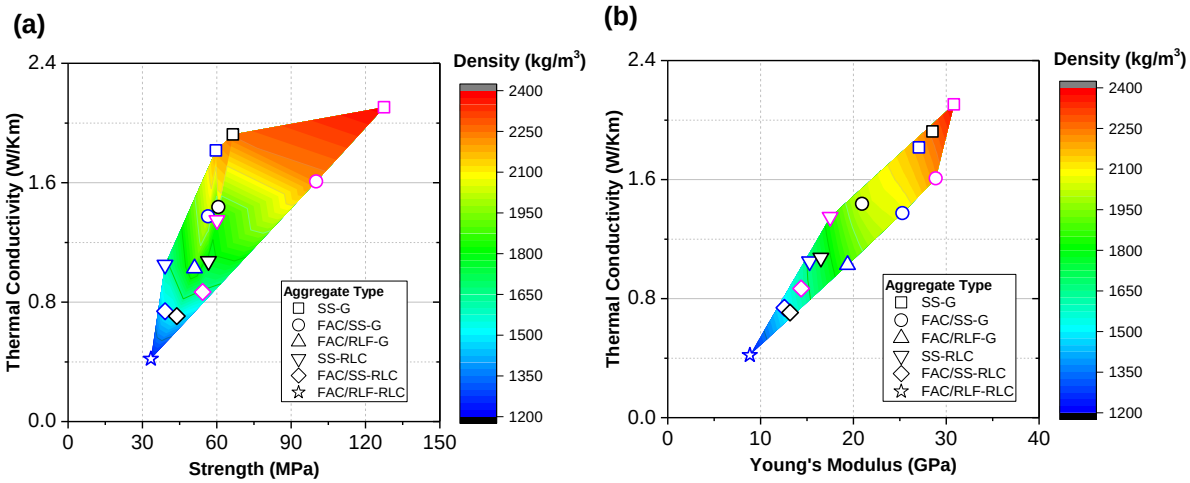

Figure 37: Thermo-mechanical relationships:
(a) thermal conductivity vs. compressive strength; and (b) thermal conductivity vs. elastic modulus

mechanical performance. Owing to the partial pozzolanic reactivity and micro-porous surface, the FAC particles bonded well with the cementitious matrix [76]. The relatively small particle size and strong shell of E106 FAC allows the FAC to act as barriers to hinder the propagation of stress cracks, see Figure 35 (d).

4.8 Balancing mechanical and thermal properties of LWCs

Figure 37 (a) and (b) show the relationship between the mechanical properties and the thermal conductivity of the various types of concrete investigated in this research. The color contour indicates oven-dry density of the materials. It is noted that all concrete mixtures studied in this research have compressive strength greater than 30 MPa and have sufficient strength to be used for structural purposes. When the thermal conductivity is less than 0.8 W/m K, LWC with different binder materials (i.e., normal strength or high strength binders) have similar compressive strength (Figure 37 (a)). On the contrary, when thermal conductivity is higher than 0.8 W/m K (density greater than 1400 kg/m^3), LWC with steel fiber reinforced high strength cementitious matrix gives the highest compressive strength. The LWC with fiber reinforced high strength binder have the best strength/conductivity ratio. Young's moduli are almost linearly correlated to thermal conductivities regardless the binder materials and aggregate type. For the concrete tested in this study, the dry density needs to be greater than 1800 kg/m^3 for the Young's modulus to be greater than 18 GPa. The lightest concrete (1220 kg/m^3) with 100% NWA substitution has moderate strength (33.4 MPa) and low elastic modulus (8.8 GPa), which may be suitable for the use in non-critical structural components such as roof slab and infill wall panel.

4.9. A two-step homogenization scheme

In a composite material system, inclusions of different sizes will be categorized as belonging to a different scale if the properties of larger sized inclusions are not affected by each individual smaller size inclusion. In that case, the larger inclusions see the original matrix materials and the smaller inclusions as new homogenous matrix [139]. Thus, the determination of effective (homogenized) thermal property of lightweight concrete and cementitious composites containing lightweight aggregates (LWAs) and fly-ash cenospheres (FAC) can be calculated using a two-step homogenization scheme as shown in Figure 38. First, the effective thermal property of cement paste containing polydispersed FACs is calculated as a composite system containing core-shell inclusions [50]. To calculate the effective thermal conductivity (ETC) of this microstructure, Felske's equations are used where the ETC of cement paste containing FACs is calculated as a function of the properties of each composing phase (i.e., cement paste matrix, FAC shell, and air enclosed in FAC particles, see Figure 38(a)) and their relative volume fractions. Then, the ETC of lightweight cement mortar containing aggregates can be calculated using two-phase homogenizations models (Figure 38(b) and (c)).

4.10. Effective thermal properties of lightweight concrete containing FAC

In a previous work by the authors [50], we demonstrated that the effective thermal conductivity (ETC) of cement mortars containing polydispersed core-shell particles can be estimated using Felske's equation [109]. For fly-ash cenospheres (FAC) that have perfect thermal conduct with the cementitious matrix, the ETC can be expressed in a simple form as:

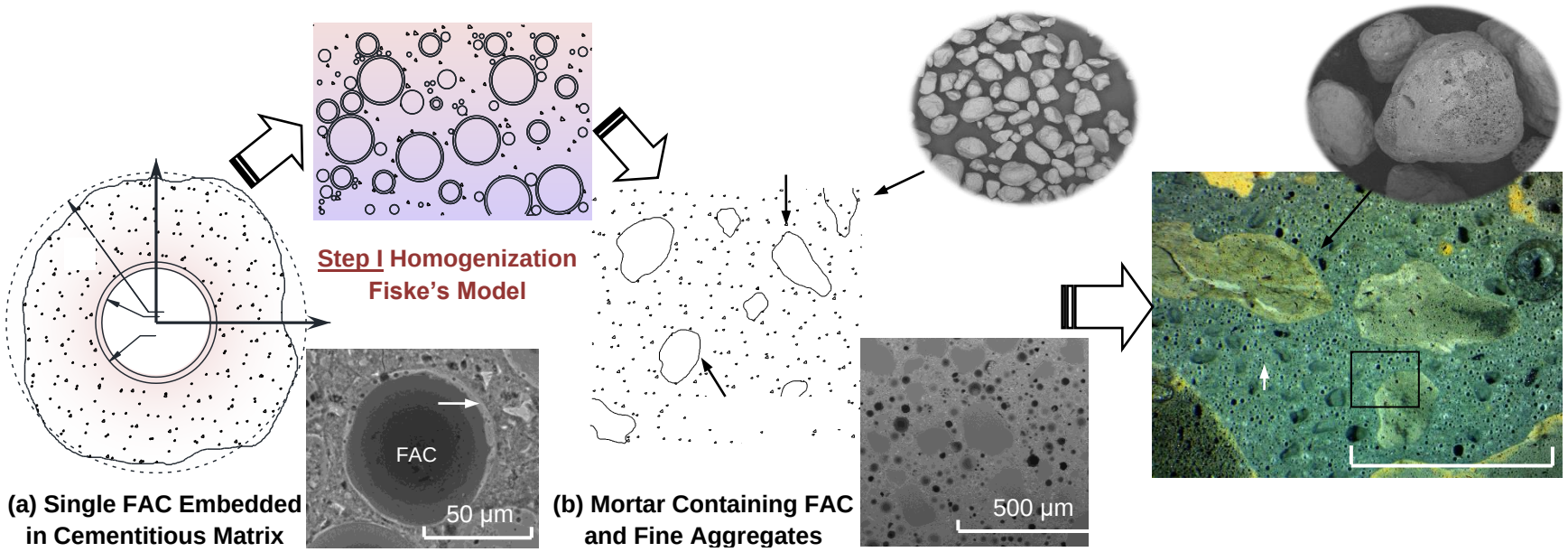

Figure 38: Microstructure and effective thermal conductivity of lightweight cementitious composite (LWCC): (a) a RVE containing one single microsphere particle; (b) mortar with polydispersed microsphere particles and fine aggregates; and (c) LWC with coarse aggregates.

Equation 12:

$$k_{eff} = \left(\frac{1 + 2\Theta \nu_f}{1 - \Theta \nu_f} \right) k_1$$

where

Equation 13:

$$\Theta = (\eta - 1)/(\eta + 2)$$

and

Equation 14:

$$\eta = 2k_{21}u/(3\rho_s - u)$$

$k_{21} = k_2/k_1$. Thus, the ETC of cement paste filled with FACs can be expressed in terms of the FAC volume fraction ν_f, the thermal conductivities of cement paste and the FAC shell, and the measured density of FAC particles, where u can be experimentally measured using gas pycnometry [110]. It is noted that Equations (3)-(5) circumvent the tedious experimental determination (even if possible) of thermal conductivity of polydispersed hollow FACs, and use only particle density and shell properties (i.e., both can be easily measured experimentally) to calculate the ETC of the composite material. The effective volumetric heat capacity of cement paste containing FACs can be expressed as (the heat capacity of air is neglected):

Equation 15:

$$(\rho c_p)_{eff} = \frac{1}{V} \frac{\partial \sum H}{\partial T} = (1 - \nu_f)(\rho c_p)_1 + \left(1 - \frac{1}{\nu_{f3}} \right) \nu_f (\rho c_p)_2$$

where T is temperature; ρ is density; H is enthalpy; and c_p is specific heat capacity of the solid material phases.

Once the homogenized thermal properties of cement paste containing FACs are obtained, the ETC of mortar and concrete containing aggregates can be obtained by treating FAC filled cement paste as a homogenized matrix, see Figure 38(b). For aggregates of different length scales (i.e., fine-ground mineral powder, sand, and coarse aggregates), the homogenization model can be repeated. In this paper, three popular homogenization models – including the parallel and series models (e.g., the cubic model proposed by Valore and Green [140]), Maxwell model [137], and the effective medium theories (EMT) [141] were employed to calculate the ETC of concretes containing fine and coarse aggregates. The results are compared in Figure 39 in comparison with the experimental data. For all 14 concrete mixtures tested in this study, the calculated ETCs coincide well with the experimental results – i.e., the differences are generally within 20% (Figure 39 (a)). Figure 39Figure 39(b) presents the calculated volumetric heat capacities of concrete in comparison with the experimentally tested values. Good agreement was found between the experimental data and calculated results. Some sources for discrepancy may include the deviation of actual volume fractions of each constituent from the design values (i.e., which may be a result of the variation of water content of aggregates for each batch), the variations of the aggregate distribution between each tested specimen, experimental errors, etc.

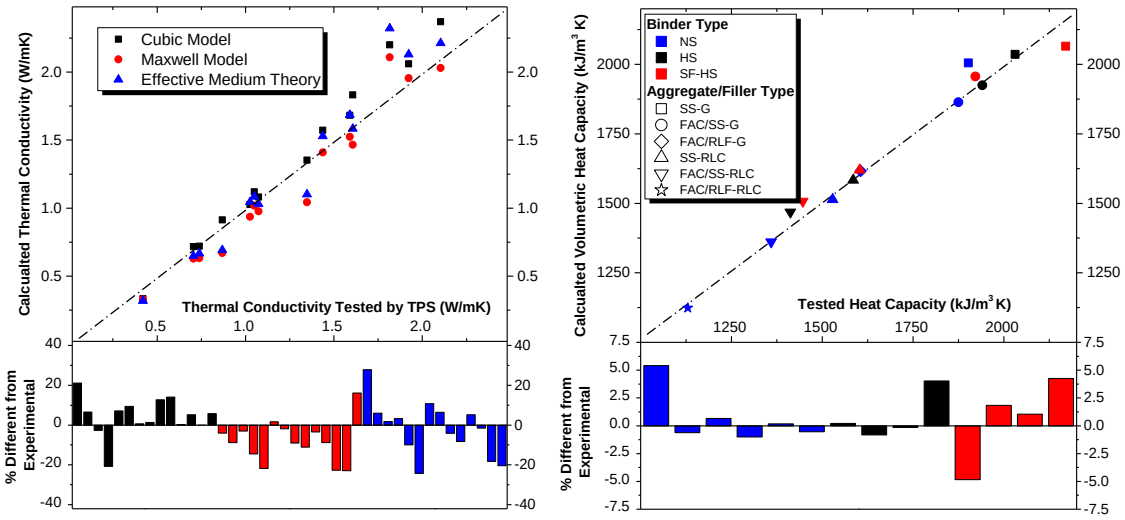

Figure 39: Comparison between calculated and experimental results: (a) thermal conductivity; and (b) volumetric heat capacity

Chapter 5. Building envelopes

A version of this chapter was originally published by Zhenglai Shen, Adam Brooks, Yawen He, Som Shrestha, and Hongyu Zhou:

Z. Shen, A.L. Brooks, Y. He, S.S. Shrestha, H. Zhou, *Evaluating dynamic thermal performance of building envelope components using small-scale calibrated hot box tests*, Energy Build. 251 (2021).

5.1 Small-scale calibrated hot box apparatus setup and calibration

5.1.1. Instrumentation and setup

A small-scale hot box apparatus with a 355 mm by 355 mm (14 inches by 14 inches) open test area was developed and calibrated. The overall dimensions of the designed hot-side are 445 mm × 445 mm × 380 mm (17.5 inches × 17.5 inches × 15 inches) in *x*-*y*-*z* directions (see Figure 4 (b)). The hot-side box consists of a five-sided insulated box with a programmable DC power supply (Rigol DP832), fin-heater (McMaster-Carr), and a variable-speed crossflow fan. The programmable DC power source has built-in sine, pulse, and ramp templets which can be used conveniently [142]. The cold-side environmental chamber is equipped with temperature and relative humidity conditioning and programmable control, which can simulate a range of temperature and humidity profiles. An insulated specimen frame is clamped between the cambers, see Figure 40. The hot-side box is also instrumented and calibrated as a metering chamber to measure the thermal flow through the test specimens. The box is constructed using 25.4 mm (1 inch)-thick rigid closed-cell foam board, finished with 19.1 mm (¾ inch) thick plywood backings and wrapped with a layer of an insulation blanket. The primary purpose of wrapping a layer of insulation blanket on top of the plywood backing is to reduce the influence of temperature fluctuation of the outside environment. An alumina baffle, 3 mm thick by 305 mm wide by 305 mm high (1/8 inches × 12 inches × 12 inches), is vertically placed in the center of the hot-side box to direct the airflow to the surface of the test specimen, see Figure 40 (b). The baffle is located at 121 mm (4.75 inches) from the test specimen surface and about 230 mm (9

inches) from the crossflow fan. The fin-heater is raised above the bottom of the baffle, which shields the test specimen from direct radiation of the heater. As a result, heated air flows up between the sample surface and the baffle through the gap at the bottom and then returns through the opening at the top. In this way, an air loop is formed in the metering chamber, reducing the potential non-uniform heating on the test specimen [143]. Type K thermocouples (Omega SA1XL-K, with accuracy ±2.2^{o}C or 0.75%) were used to measure the temperature difference. Five type K thermocouples and one type K thermocouple were attached on the backside and the remaining four sides of the metering walls (total of 18 locations, see Figure 40 (b)), respectively. Thus, heat flux going through the metering walls was able to be calculated from temperature readings. Instrumentation is also provided to measure the total energy input into the hot box (i.e., heating and fan). The heat losses are determined by calibrating the box with panel specimens of known thermal properties (R-value), detailed in the following section.

The hot- and cold-side air temperature was measured with a set of RTD sensors (Omega RTD-805). A fan circulated air in the cold-side chamber, and the air temperature was controlled by the built-in controller of the environmental chamber. At the same time, an additional RTD sensor and a relative humidity (RH) sensor (Omega HX92B) were mounted near the specimen surface to directly measure the air temperature and RH level near the specimen panel. All sensors for data collection were conditioned using a *National Instrument* PXI-express DAQ system with adjustable data sampling frequency up to 100 samples/sec. During steady-state tests, a constant power input was supplied to the DC heater in the hot-side box. The air temperature in the environmental chamber (cold-side) was maintained constant was well. The temperature profile of each side could be individually controlled if the dynamic thermal performance of the building envelope element specimens were to be tested. In addition, a FLIR

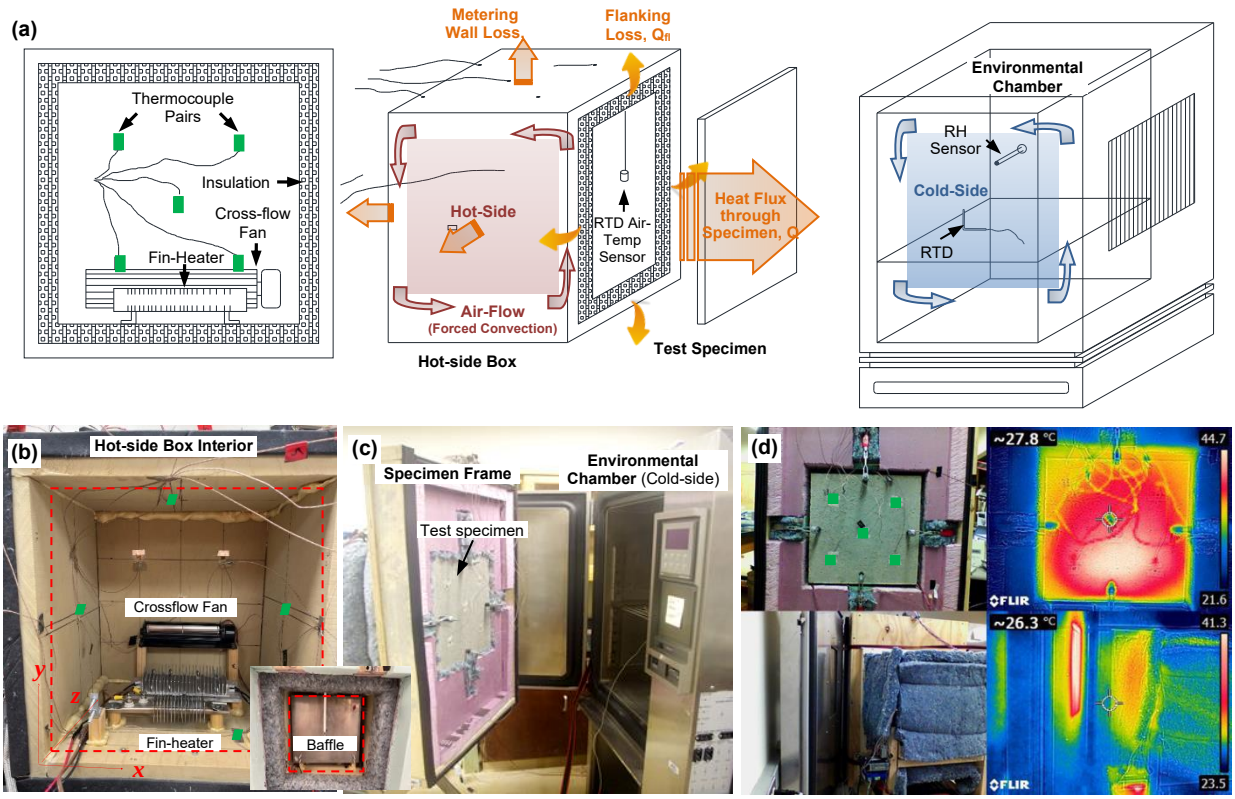

Figure 40: Hot box setup and instrumentation:
(a) schematic figures showing the setup of hot box (hot-side), heat losses, and the environment chamber (cold-side); (b) pictures showing the instrumentation of the hot-side box (metering chamber); (c) picture showing the specimen frame and its interface with the environment chamber (cold-side); and (d) infrared thermal images showing the heat flow through the specimen and heat loss (flanking loss and frame loss)

E5XT thermal imaging inspection camera was used to collect thermal images during experimental tests.

5.1.2 Calibration

A homogenous rigid foam panel specimen with known thermophysical properties was tested under steady-state conditions to calibrate the hot box apparatus. The thermophysical properties (i.e., thermal conductivity and specific heat) of the rigid foam panel and materials used for constructing the small-scale hot box apparatus were measured by the Transient Plane Source (TPS) method using a *Hotdisk TPS 1500* thermal constant analyzer [122]. The calibration of the small-scale hot box apparatus was carried out by balancing the energy components following the procedure outlined in ASTM C1363 [144], where the fin-heater and the crossflow fan were considered as the energy input into the hot-side box. The total energy input is the summation of the programmed electricity energy supplied to the heaters recorded by the NI PXI DAQ system and the energy consumed by the fan measured by an inline power meter. The system energy losses are subtracted from the total energy input to calculate the amount of thermal energy passing through the tested specimen (i.e., rigid foam panel).

A total of three energy loss components were considered based on the geometries of the hot box, sample holder, and surrounding frame, including the metering wall heat loss (Q_{mw}), flanking heat loss (Q_{fl}), and the heat loss from frame/foam (Q_{ff}). The frame/foam loss was added to account for heat losses due to the geometry of the hot box developed herein, which is different from the ASTM configuration. Foam loss refers to the heat loss due to the contact of the insulated specimen frame to the cold-side chamber. The frame loss refers to the heat loss due to the sample supports and clamp mounts. Figure 4 (d) shows the thermal loss associated with the specimen frame.

Since the thermal properties of the metering wall materials are known (experimentally measured by the TPS method), the metering wall loss, Q_{mw}, is calculated based on the readings of thermocouple pairs and can be calculated as [144]:

Equation 16:

$$Q_{mw} = \frac{\chi_{eff-mw} A_{eff-mw} \left(T_{si-mw} - T_{so-mw}\right)}{L_{mw}}$$

where $\chi_{eff\text{-}mw}$ is the effective thermal conductivity of the metering wall, $T_{si\text{-}mw}$ and $T_{so\text{-}mw}$ are the inside, and outside wall surface temperature respectively, L_{mw} is the wall thickness, and $A_{eff\text{-}mw}$ is the effective area normal to heat flow which can be calculated by:

Equation 17:

$$A_{eff-mw} = A_{si-mw} + 0.54 L_{mw} \left(\sum el_p\right) + 0.60 L_{mw}^2$$

with Asi-mw is inside surface area of the metering chamber, Σelp is interior edge lengths of the metering chamber where walls meet, and the coefficients 0.54 and 0.15 (0.60 = 0.15 ×4) are the conduction shape factors for metering wall interior edges and the thickness of the metering wall respectively [40].

The flanking loss is estimated using a FLIR infrared thermal camera (see Figure 40)). The flanking loss (Q_{fl}) can be calculated as:

Equation 18:

$$Q_{fl} = \chi_{eff-fl} \left(A_{eff-fl} / L_{eff-fl}\right) \Delta T_{ai-ao}$$

where $\chi_{eff\text{-}fl}$ is the effective thermal conductivity of base insulation and the skin material, $A_{eff\text{-}fl}/L_{eff\text{-}fl}$ is the effective area/path length of the entire frame around its perimeter, and $\Delta T_{ai\text{-}ao}$ is the air-to-air temperature difference between inside and outside.

The frame and foam heat loss (Q_{ff}) can be calculated as:

Equation 19:

$$Q_{ff} = \frac{A_{frame}}{R_{frame}}\left(T_{si-frame} - T_{so-frame}\right) + \frac{A_{foam}}{R_{foam}}\left(T_{si-foam} - T_{so-foam}\right)$$

where A_{frame}, A_{foam}, R_{frame}, R_{foam}, $T_{si\text{-}frame}$, $T_{si\text{-}foam}$, and $T_{so\text{-}frame}$, $T_{so\text{-}foam}$, are the surface area, thermal resistance, and inside and outside surface temperatures of the frame and foam, respectively.

By subtracting all losses from the total input energy into the system, the total heat flowing through the specimen can be determined. The R-value of the test specimen (R_{spe}) can then be calculated by:

Equation 20:

$$R_{sp} = \frac{A_{sp}}{Q_{input} - Q_{loss}}\left(T_{sp-hot} - T_{sp-cold}\right)$$

Table *11* summarizes the calibration result by using a rigid foam panel with known thermal properties. It includes the hot box's geometry and thermophysical properties, the specimen, the measured temperature readings, energy losses, and the calculated R-value of the specimen. As can be seen, the R-value obtained by the hot box test matches well to the R-value calculated based on the thermal conductivity value tested by TPS with 0.5329 m2K/W.

5.2. Thermal performance characterization of wall panels

5.2.1 Specimen design

Following the calibration process, three scaled-down concrete sandwich wall panels were prepared and tested under periodically transient conditions (i.e., sinusoidal temperature wave) using the small-scale calibrated hot box. Data obtained by the transient tests were used to calculate the dynamic thermal response of the wall assemblies based on the equations derived in Shen et.al [145].

In this study, three concrete sandwich wall panels made from normal-weight concrete,

Table 11. Energy input, loss, and test panel R-value

$A_{eff\text{-}mw}$	L_{mw}	$\sum el_p$	$T_{so\text{-}mw}$	30.3 °C	Q_{mw} 6.785 W
0.201 m^2	0.045 m	3.048	$T_{si\text{-}mw}$	37.6 °C	
A_{eff}	0.201 m^2		λ_{eff}	0.205 W/mK	
$L_{eff\text{-}fl}$	1.78 m		$T_{so\text{-}fl}$	17.0 °C	Q_{fl} 0.595 W
A_{frame}	R_{frame}		$T_{si\text{-}frame}$	37.1 °C	Q_{ff} 3.741 W
0.062 m^2	0.214 m^2K/W		$T_{so\text{-}frame}$	26.0 °C	
A_{foam}	R_{foam}		$T_{si\text{-}foam}$	37.6 °C	
0.011 m^2	0.258 m^2K/W		$T_{so\text{-}foam}$	28.8 °C	
Q_{input}		16.654 W	Q_{loss}		11.121 W
A_{sp}	$T_{sp\text{-}hot}$	$T_{sp\text{-}cold}$	Q_{input}-Q_{loss}		R_{sp}
0.126 m^2	36.4 °C	13.1 °C	5.533 W		**0.5582**

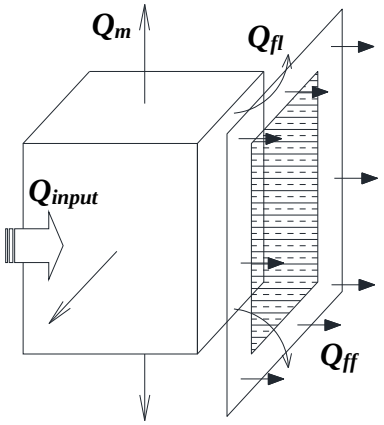

structural lightweight concrete, and low-density cementitious composites [41] were prepared and tested. The physical and thermal properties of concretes used to construct the sandwich wall panels are summarized in Table 12. The concrete mixture design was presented in a previous paper of the authors [41], and three different concrete types were selected in this study, i.e., C1 and C2 represent lightweight concrete while C3 represents normal weight concrete. The difference between C1 and C2 is that the mixture of C1 also added fly-ash cenosphere (FAC) to further reduce the concrete's density and thermal conductivity. The densities of C1 to C3 ranged from 1224 to 2387 kg/m3 (oven-dry condition), with thermal conductivity measured by the transient plane source (TPS) method [42] ranged from 0.423 to 2.105 W/m-K. Figure 5 presents the preparation process, configuration, and instrumentation of the scaled-down insulation concrete sandwich panels. The test panels consist of one layer of 15.9 mm thick rigid expanded polystyrene (EPS) foam board sandwiched between two layers of concrete wythes (25.4 mm thick for each layer). A layer of wire mesh (50mm by 50mm spacing) was used as reinforcements for the concrete layers, and U-type steel connectors were used to connect the two concrete wythes and provide sheer resistance. The prepared insulated concrete sandwich panels present one half ($1/2^{th}$) scale of a typical concrete sandwich wall panel having an overall thickness of 127 mm (5 inches). Five thermocouples were attached on the front and back surfaces of the tested specimens, respectively (see Figure 41 (a)). Moreover, thermocouples were also attached to the surfaces of the insulation panel to monitor the temperature development history during the experimental test and validate the finite difference method. *Table 13* summarizes the design and dimensions of each panel.

Table 12. Thermal properties of concrete materials

Concrete ID	Density	Thermal Conductivity	Thermal Diffusivity	Volumetric Heat Capacity
	Kg/m^3	W/mK	mm2/s	kJ/m^3
C1 (NS-FAC/RLF-RLC*)	1224	0.423	0.334	1267
C2 (NS-SS-RLC*)	1614	1.050	0.717	1464
C3 (NS-SS-G*)	2185	1.817	0.954	1904

* represents the Mix ID in reference [7].

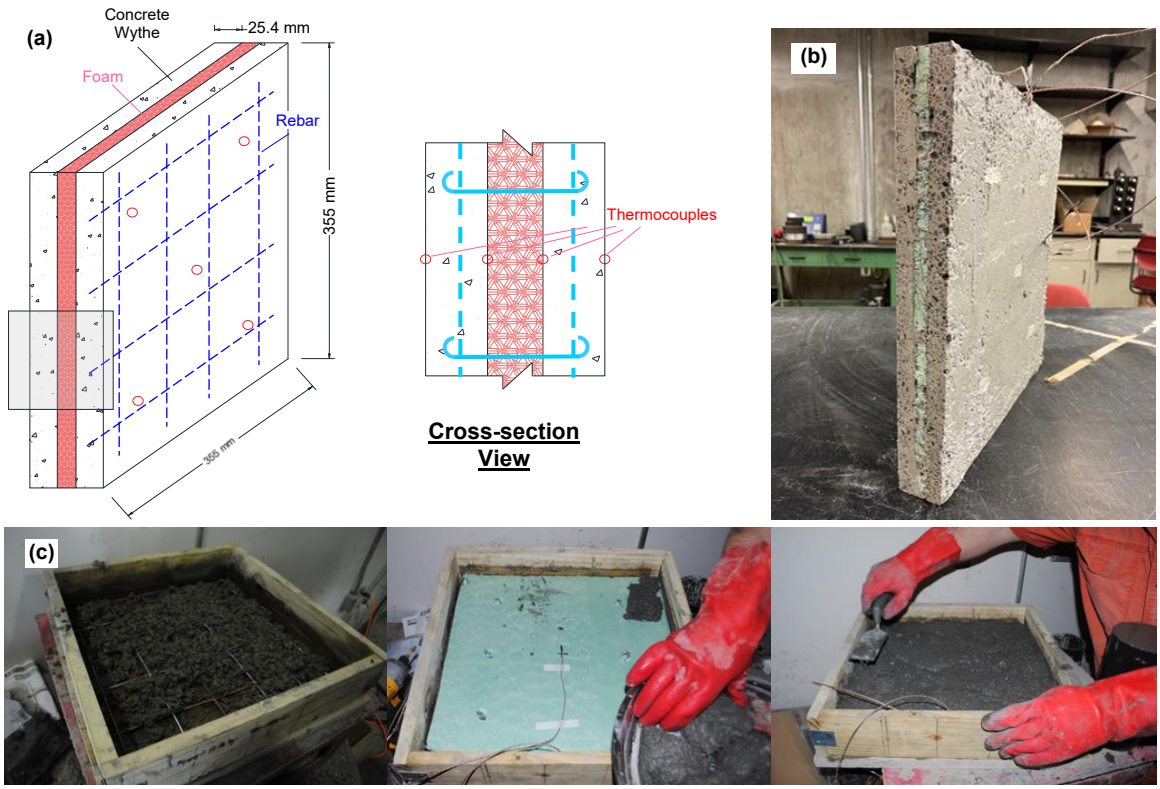

Figure 41: The scaled-down concrete sandwich wall panel specimen for thermal testing: (a) Illustrative figure showing the configuration and instrumentation; (b) picture showing the cross-section of the specimen panel; and (c) pictures showing the specimen preparation process

Table 13. Concrete sandwich wall panel composition and thermal transmittance

Sandwich panel	**Component composition (hot to cold side)**	**Calculated thermal transmittance (W/m^2K)**
LLL	2.54 cm C1; 1.59 cm EPS; 2.54 cm C1	1.934
NNL	2.54 cm C2; 1.59 cm EPS; 2.54 cm C2	2.246
NNN	2.54 cm C3; 1.59 cm EPS; 2.54 cm C3	2.354

5.2.2 Transient thermal behavior of down-scaled concrete sandwich wall panels

Figure 42 presents the experimental data obtained by the small-scale hot box apparatus. The temperature of the hot-side box follows a sinusoidal temperature profile with a period, P, equal to 6 hours to account for the ½ scale factor (to represent a 24-hour test cycle for a full-scale specimen). On the cold side, the environmental chamber air temperature was kept at a constant temperature at around 15°C. During the experiment, both the hot- and cold-side were pre-heated or cooled to a pre-designated temperature (close to steady-state), followed by the sinusoidal forcing temperature solicitation. As can be seen from the experimental data, the hot-side air temperature history follows the sinusoidal input temperature closely. In contrast, the cold-side air temperature experienced some disturbances due to the limitation of the environmental chamber's control program. Therefore, data segments with environmental chamber temperature close to a constant were used to calculate the dynamic properties, i.e., time lag and decremental factor.

5.3 Mechanical performance of small scale concrete sandwich panels

Further, this research evaluated the performance of concrete mixtures developed and presented in previous work by the authors. Of the fourteen mixes that were tested, three were evaluated as precast concrete sandwich panels under uniaxial compression. Two of the mixtures have normal strength binder (NS) and a combination of normal weight aggregate, silica sand (SS) and gravel (G), as well as lightweight aggregate, fly ash cenospheres (FAC) and RiverLite™ coarse and fine (RLC, RLF), and one mixture with high strength binder (HS) and steel fibers (SF). From these mixture two uniform panels were created with both wythes the same mixture, NS-SS-RLC and NS-FAC/RLF-RLC, while the third panel consisted of two mixtures, one wythe of NS-

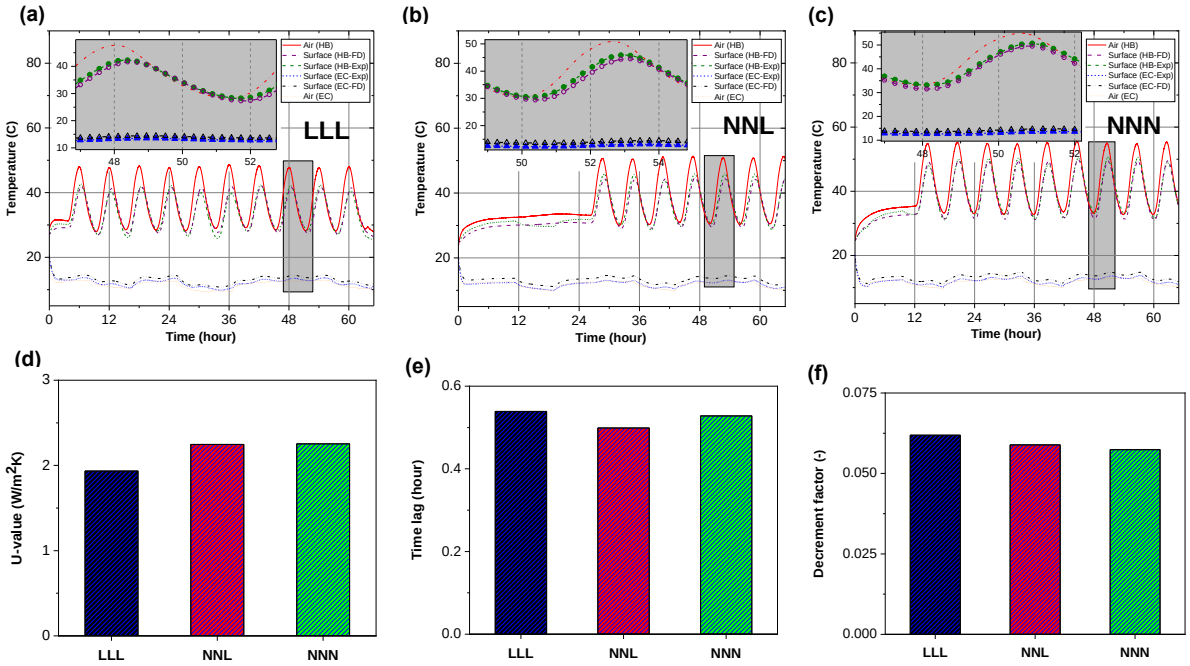

Figure 42: Hot box testing results versus finite different method simulated results and thermal properties of tested panels:
(a) LLL; (b) NNL; (c) NNN; (d) U-value, (e) time lag; and (f) decrement factor

FAC/RLF-RLC and one wythe of HS-SS-G-SF. Samples that were made from single mixtures had grid reinforcement on both sides connected by shear hooks, 3.5mm diameter steel. The fourth panel only the lightweight concrete (NS-FAC/RLF-RLC) had a rebar grid while the high strength wythe relied on the distributed steel fiber (20 wt% of cement, 1.49% by volume)) to act as the reinforcement and anchor the shear hooks. Figure 40 presents the specimen design and preparation process of the concrete sandwich panels, and Table 11 shows the mixture design for the chosen four mixtures. The test panels consist of one layer of 15.9 mm thick rigid expanded polystyrene (EPS) foam board sandwiched between two layers of concrete wythes (20 mm thick for each layer). A layer of wire mesh (75 mm by 75 mm spacing) was used as reinforcements for the concrete layers, and hook type steel connectors were used to connect the two concrete wythes and provide shear resistance. Holes were placed in the insulation board at the shear connector location to allow the hooks to pass through while maintaining a "full sheet" of insulation between the two concrete wythes. A table style concrete vibrator was used to prepare the panels. Each panel was constructed with three layers, the first layer was poured with a rebar grid and shear hooks in place, then the second layer foam board was placed down and vibrated to remove trapped air between the concrete and insulation. Finally, the second layer of reinforcement was attached to the shear hooks then covered with concrete. The prepared insulated concrete sandwich panels present roughly one half (1/2th) scale of a typical concrete sandwich wall panel having an overall thickness of 127 mm (5 inches). Each panel had a height of 430mm and a width of 175mm.

5.3.1 Experimental setup for uniaxial compression

The mechanical tests were performed on a 1780 kN concrete compression machine. The mechanical loading was performed at a displacement rate of ~0.18mm/min. Each sample was

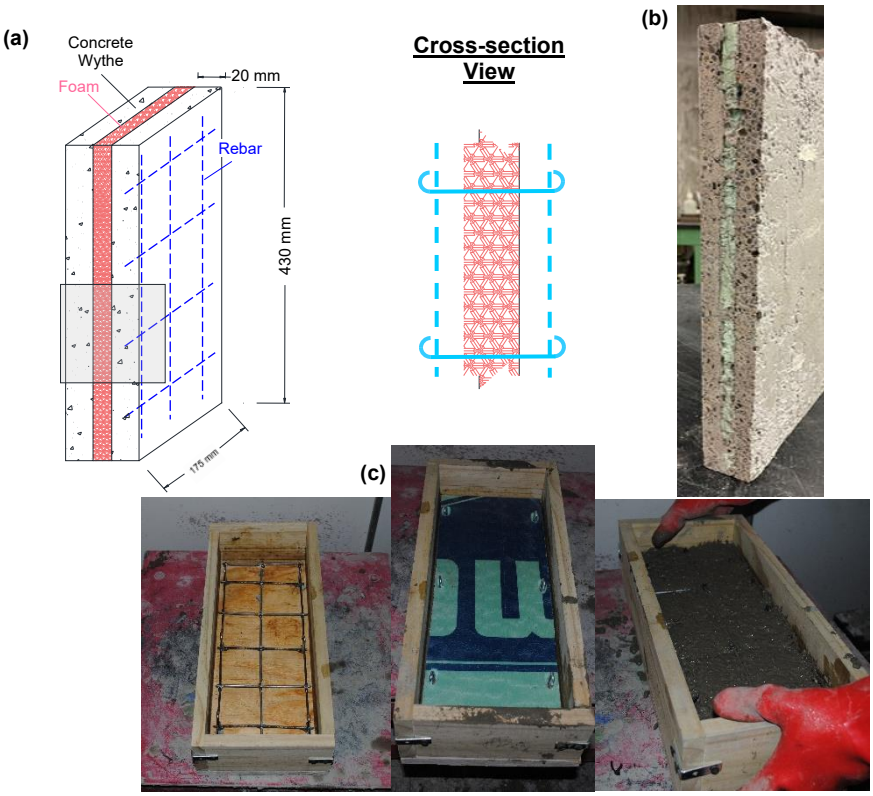

Figure 43: Scaled-down concrete sandwich wall panel specimen for mechanical testing: (a) Illustrative figure showing the configuration and instrumentation; (b) picture showing the cross-section of the specimen panel; and (c) pictures showing the specimen preparation process

Table 14. Test matrix and mix proportions (by weight, kg of materials/ m^3 of concrete)

Mix ID*	**Binder**		**Water**	**W/ (C+F)**	**FAC**	**Quartz Flour**	**Steel Fiber**	**Silica Sand**	**Gravel** (Lime Stone)	**Lightweight Aggregate****	
	Cement	Silica Fume								RiverLite™ (Fine)	RiverLite™ (Coarse)
NS-SS-G	437.4	--	153.2	0.35	0.0	--	--	734.7	874.7	--	--
NS-SS-RLC	437.4	--	153.2		0.0	--	--	734.7	0.0	--	377.0
NS-FAC/RLF-RLC	437.4	--	153.2		96.0	--	--	0.0	0.0	216.5	377.0
HS-SS-G-SF	481.5	85.0	153.0	0.27	--	249.4	116.1	424.7	804.4	--	--

* NS- – Normal strength cement binder; HS- – High strength cement binder with silica fume and lower water to binder ratio; SS – Silica Sand; G – Natural limestone gravel; RLC – RiverLite™ Coarse LWA; RLF – RiverLite™ Fine LWA; -SF – Steel fiber reinforced;
FAC/SS – 50% of fine NWA are replaced by FAC; FAC/RLF – fine aggregates are only comprised of FAC and RLF.

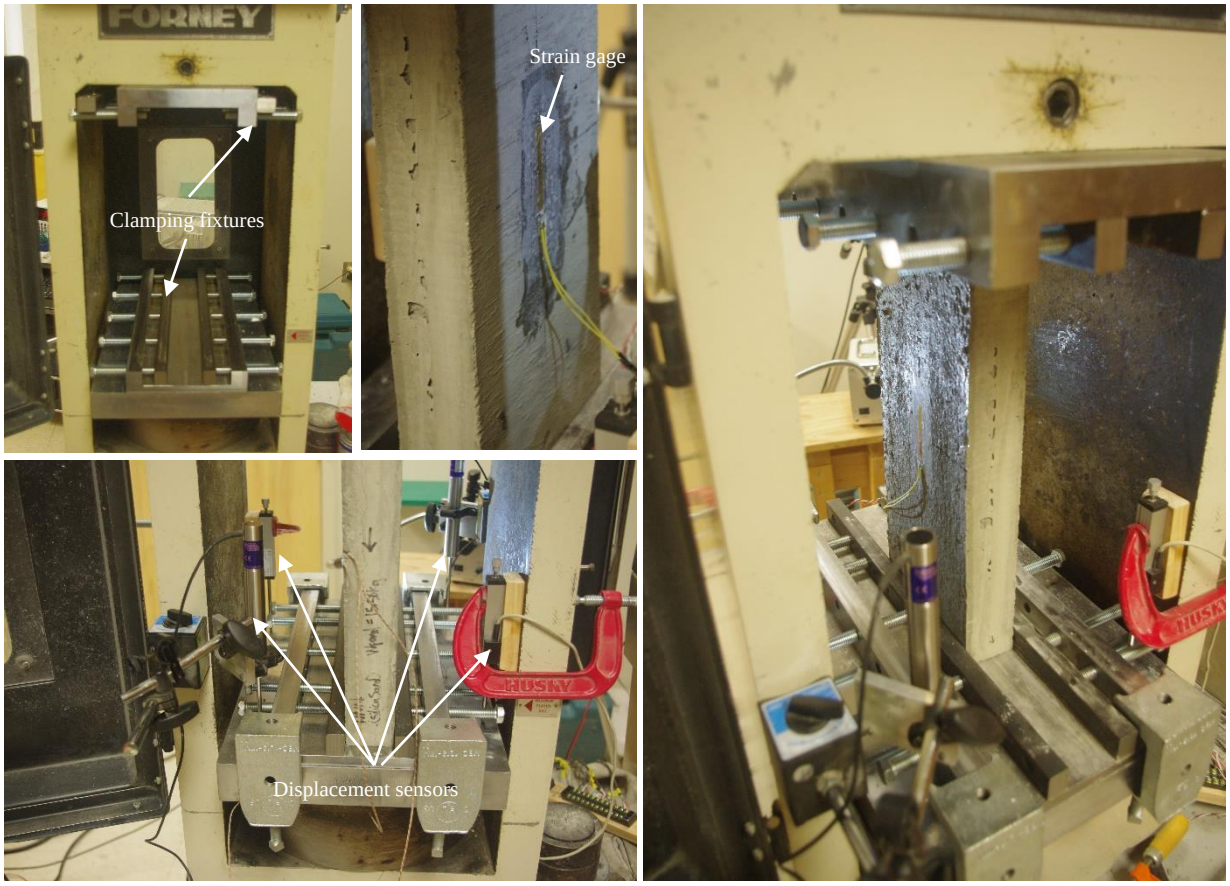

Figure 44: Experimental set up for scaled concrete sandwich panels under uniaxial loading.

clamped into a fixed holder on the top and bottom of the sample, this can be seen in Figure 41. The panels were clamped into position on the bottom fixture, then the platform was raised until the panel was in contact with the upper fixture. Finally, the tensioning bolts were adjusted so that there was no lateral force applied to the samples from clamping. Vertical displacement was measured on each of the four corners of the loading plate using two LVDTs and two potentiometers each sensor had a gage length of 50 mm. Along with the displacement sensors each sample had two concrete strain gages (50 mm) placed at the center of the sample, along each side of the specimen, aligned along the compression axis, see Figure 41. A CCD camera was staged to record the damage and failure of the specimens. Care was taken to prevent any asymmetric loading from happening with all panels by smoothing and squaring the loading surfaces before testing and leveling the samples during test set up.

5.3.2 Mechanical behavior

The material properties of the concrete can be found in Table 10 of the previous chapter. The mechanical performance of a concrete sandwich panel can be estimated based off the material properties of the concrete used, but the complexity that is added to the system introduces uncertainties, e.g., bond strength with rebar and possible a gapping. Based on the material performance of the concretes tested the results are generally good. Figure 45 shows the load vs displacement plot of all three panels.

Compressive strength and stiffness

The panel with the high strength binder and steel fiber reinforced wythe (HS-SS-G-SF) achieved the highest load capacity even when combined with a wythe of the lowest performing material (NS-FAC/RLF-RLC). This sample demonstrated that the combination of strong outer

and a lightweight insulating layer of concrete can result in a composite material that outperforms normal structural concrete in strength capacity. The material that resulted in the lowest strength was the NS-FAC/RLF-RLC sample that was made with the lightest concrete. This is the expectation for this material because the mixture is designed to reduce weight and increase thermal resistance of the panel, not have high mechanical strength, though it should be noted that the material performance achieves over 30 MPa and would be suitable for some structural applications where young's modulus is less important. Figure 45 shows the failure of each sample. It can be seen that there was a horizontal bending failure crack on the high strength binder panel (this develops at large deformation and will be discussed more later) while the other two panels show crushing damage within the top 25% of the sample which is in agreement with other work by Awan et. al. [146,147].

To prevent damage to the foam-concrete interface the panels were not submerged in water to cure as is generally the case with cylinders but were periodically saturated with water on both concrete surfaces. The LWA that was used in the NS-SS-RLC and NS-FAC/RLF-RLC panels was saturated, by the method mentioned in the previous chapter, before being mixed. It is known that the use of LWA for internal curing has benefits to the strength of the concrete; therefore, it is proposed that this process allowed the NS-SS-RLC panel to perform better than expected.

Figure 45 also shows that the stiffness of panels NS-SS-RLC and HS-SS-G-SF_ NS-FAC/RLF-RLC are almost identical. Given the young's Moduli of the concretes shown in Table 10 this is not the expected outcome; however, since the HS-SS-G-SF_ NS-FAC/RLF-RLC panel combines two concrete types a composite young's modulus was calculated. Since both wythes of

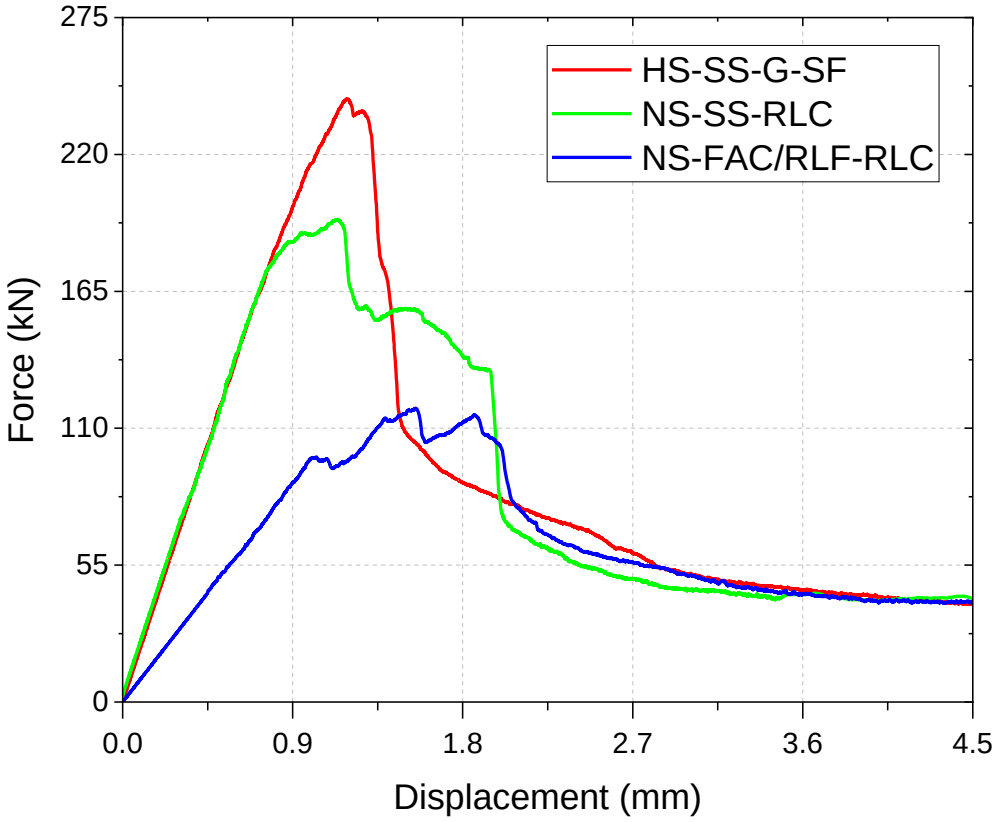

Figure 45: Force deflection curves for small scale concrete sandwich panels.



Figure 46: Failure of scaled down concrete sandwich panels.

concrete have the same area the composite young's modulus can be calculated as half the sum of the moduli of both HS-SS-G-SF and NS-FAC/RLF-RLC, 30.83 GPa and 8.84 GPa respectively. This composite young's modulus, 19.84 GPa, is similar to that of the NS-SS-RLC material, 15.28 GPa, the difference between the two can be accounted for by the internal curing as well as the fact that the HS-SS-G-SF_ NS-FAC/RLF-RLC panel only has one rebar grid to support the load. As discussed before steel fiber in the HS-SS-G-SF wythe of concrete was used in place of the rebar reinforcement in that panel.

Ductility

Though the HS-SS-G-SF_ NS-FAC/RLF-RLC panel reached the highest strength the ductility was lower than expected. This is most likely due to the asymmetric loading that resulted from the two types of materials, causing a bending force to be applied to the stronger concrete in the panel Though the HS-SS-G-SF_ NS-FAC/RLF-RLC panel reached the highest strength the ductility was lower than expected. This is most likely due to the asymmetric loading that resulted from the two types of materials, causing a bending force to be applied to the stronger concrete in the panel once the ultimate load of the weaker concrete had been reached. The material that resulted in the lowest strength was the NS-FAC/RLF-RLC specimen which is the lightest concrete. This is as expected for this material based on the mixture design is to reduce weight and increase thermal resistance of the panel, not have high mechanical strength. Based on the material property tests it was expected that this specimen panel had high ductility when lightweight aggregates and stress crack propagation within the matrix. For LWA the stress cracks start and propagate through the LWA skeleton. However, stress cracks start in the matrix and propagate along the ITZ of NWAs. As can be seen in Figure 46 both panels that incorporated lightweight aggregates demonstrated

the highest levels of ductility or roughly the same amount. The lightweight coarse aggregates have a controlling impact over the ductility over lightweight fine aggregates and lightweight fillers. This is apparent when comparing NS-FAC/RLF-RLC specimen with the NS-SS-RLC specimen. The additional replacement of normal weight fine aggregate with lightweight fine aggregate had a minimal impact on the ductility of the lighter weight specimen.

Performance of steel fiber reinforced concrete

For all concrete wythe a steel rebar grid was used as reinforcement, with the exception of the HS-SS-G-SF concrete wythe. As mentioned earlier this layer of concrete included 1.49 percent steel fiber (SF) by volume. This test evaluated the mechanical performance of a composite sandwich panel, i.e., wythes of two types of concrete, as well as the performance of a steel fiber reinforced concrete (SFRC) with no added rebar. Figure 47 (a)-(d) show four stages the test for this material: before peak, at the peak load, before plateau, and at buckling failure. The mechanical performance was discussed in previous sections. This section will focus on the performance of the steel fiber concrete in terms of delamination and pull-out failure of the HS-SS-G-SF wythe. Under compressive loading the SFRC was able to carry the largest load of the four samples tested. Comparing the data from the plot in Figure 3 along with the images captured with the CCD camera and presented in Figure 44 it can be seen that the failure of the panel resulted from the crushing of concrete rather than pull-out or buckling failure. In fact, the buckling did not surface until a vertical displacement of 39 mm was reached. This buckling was due to the pull out of the shear connectors between the two wythes of concrete. As can be seen in Figure 47 (e) the pull out was not just the shear connector, but the connector was able to pull out the concrete and fibers that were inside the hooked area, i.e., the concrete failed before the connector did.

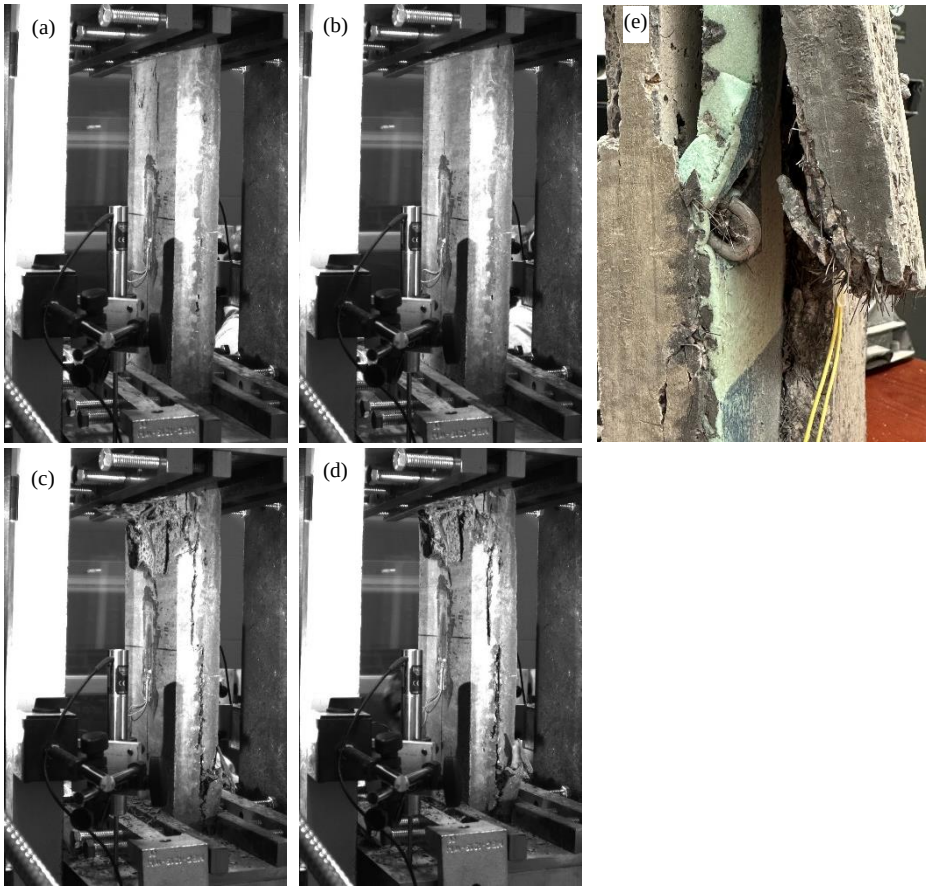

Figure 47: Failure of fiber reinforced concrete wythe:
(a) Mid load before peak, (b) at peak load, (c) mid load after peak, (d) start of buckling (e) failure at 39 mm

Chapter 6. Towards future additive construction

A version of this chapter was originally published by Adam Brooks, Yawen He, Nima Farzadnia, Shayan Seyfimakrani, and Hongyu Zhou:

Brooks, Adam & He, Yawen & Farzadnia, Nima & Seyfimakrani, Shayan & Zhou, Hongyu. (2022). *Incorporating PCM-enabled thermal energy storage into 3D printable cementitious composites.* Cement and Concrete Composites. **129**. 104492.

6.1 Material design of 3D printable mixture design incorporating TES

Large-scale concrete 3D printing and digital construction has brought enormous potential to expand the design space of building components (e.g., building envelope) for the integration of multiple architectural functionalities including energy saving [27]. With large-scale 3D printing technology, unprecedented levels of structural efficiencies and/or multifunctionality can now be achieved [148] – i.e., additional functions can be embedded in the structural parts, the architectural components are not only constructed for mechanical properties but also serve other functions such as soundproofing and thermal insulation. This new paradigm of construction technology allows a new approach for building design – the material and component can be parametrically designed attuning to the optimal performance and functionalities.

While the thermal energy storage enabled by PCM has been demonstrated as one of the most effective means to improve building's energy performance, microencapsulated phase change materials (MEPCMs) are still considered expensive as compared to other building materials. Due to the nonlinear nature of the 3D printing process, this new construction technique can facilitate architectural designs with spatial variations in geometry and/or material composition – e.g., PCM-charged concrete can be used to construct building envelope components that can benefit from passive solar while others can be built using less expensive materials with higher insulation to optimize the cost-benefits, see Figure 48: Conceptual design

showing strategically placed thermal energy storage enabled by 3D printed cementitious materials charged with microencapsulated PCM (MEPCM) One key element to realize the optimal thermal mass (or TES) distribution in such designs is the feasibility of incorporating MEPCM directly into 3D printable structural materials like concrete, see Figure 48 To this end, this paper aims to understand the influence of MEPCM on both the fresh (printability) and hardened properties (i.e., mechanical, and thermal properties) of 3D printable cementitious composite materials with MEPCM.

3D printable cementitious composite mixtures were formulated by blending a polymer microencapsulated PCM (MEPCM) – e.g., Micronal® 24D, with a cementitious 3D printing pre-mix supplied by Laticrete LLC Inc (Laticrete M68). The main constituents of Laticrete M68 include Portland cement, quartz, calcium oxide, and limestone [149]. To incorporate PCM microcapsules into the cementitious premix, the Micronal® 24D microcapsules were simply added to the dry mixture to achieve designated volume loadings of 0%, 2.5%, 4.5%, 6%, which correspond to mixture naming Ref, Mic2.5, Mic4.5, and Mic6, respectively, see Figure 49. The Micronal® 24D used in this study was a polymer encapsulated paraffin wax with melting temperature of 21-22℃ and heat of fusion of 90 kJ/kg, see Table 15. The inserted figure in Figure 49 shows the conglomerates of Micronal® particles, where microencapsulated particles with particle size of 2-3μm were grouped into larger size (50-300μm) conglomerates. A Hobart mixer (20 L) was used to mix the printing material at a constant mixing rate for about 5 minutes. During mixing, the adhesive keeping the conglomerates together was partially dissolved and the Micronal® particles become evenly distributed across the cementitious materials with scattered clusters.

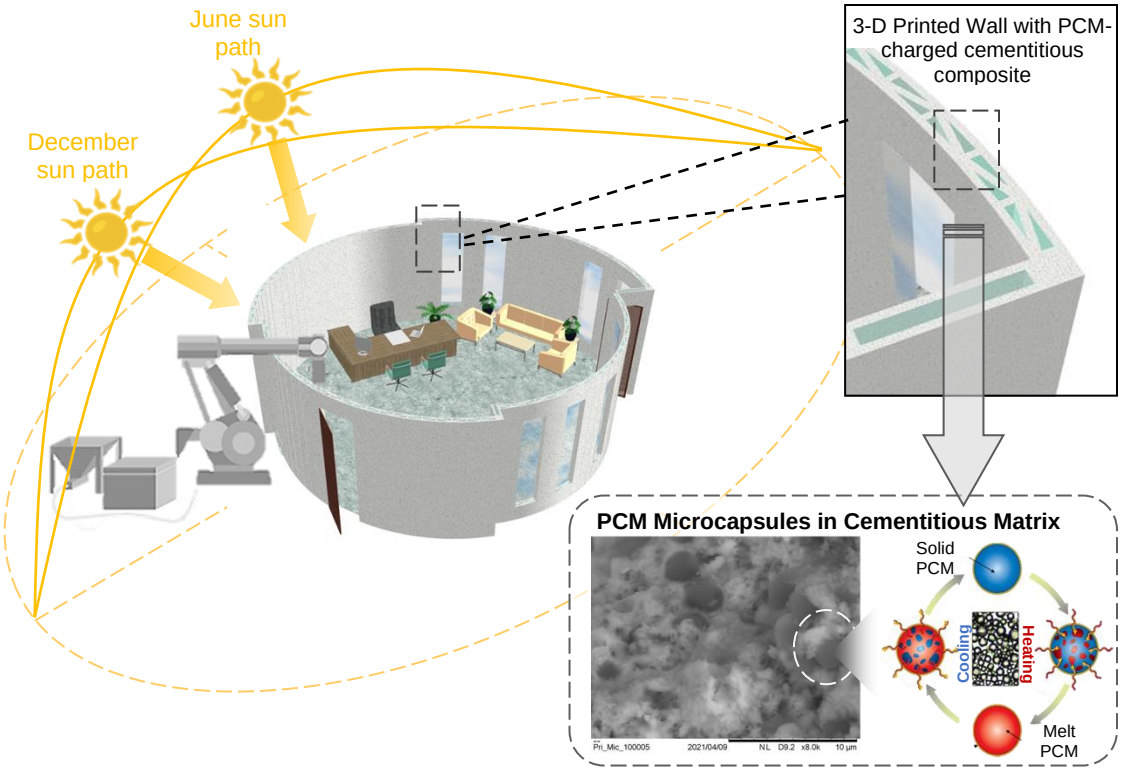

Figure 48: Conceptual design showing strategically placed thermal energy storage enabled by 3D printed cementitious materials charged with microencapsulated PCM (MEPCM).

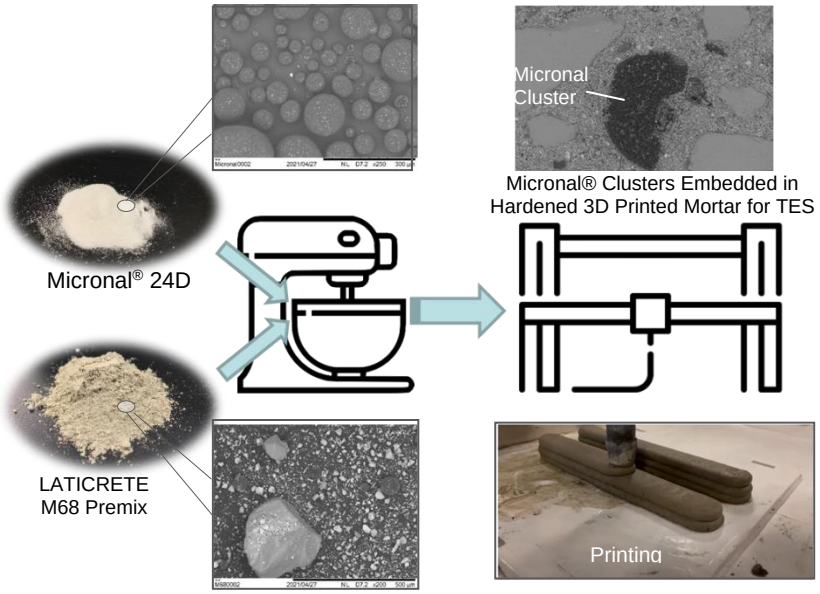

Figure 49: Illustrative figure showing the mixing and printing process of cementitious composites charged with MEPCM.

Table 15. Properties of the MEPCM

Material	Shell type	Mean Particle Size	Density	Heat of Fusion, ΔH_m		Phase Change Temp, T_m	Phase Change Temp, T_s
		μm	kg/m^3	kJ/kg	kJ/L		
Micronal® 24D	Nonhazardous Polymers and synthetic	5-300 μm (agglomeration of 2-3 μm microcapsules)	1.005	90.31	90.74	22.3℃	21.1℃

6.2 Fresh properties and printing parameters

6.2.1 Concrete 3D printer setup

Figure 50 shows the 3D printer set-up with a screw-driven extrusion mechanism used in this study. The gantry style concrete 3D printing has a screw-driven extruder, motion sliders, and a platform with effective printing volume of 0.75 m (L) × 0.675 m (W) by 0.675 m (H). The freshly mixed printing material was fed directly to the hopper. The volume of the hopper is 2 Liters. An auger driven by a servo-motor with controllable speed is equipped in the hopper to transport the cementitious printing material to the nozzle. The printing nozzles have openings with diameter of 5-35 mm, see Figure 50. The print head has 3 degrees-of-freedom in the X, Y and Z directions and the nozzle dimensions, horizontal print head velocity, and the extrusion rate were configurable and adjusted based on specific objectives of this study. Printability of the mixtures were examined by varying the extrusion rate and horizontal print head velocity at different ranges. The printability properties characterized in this study included flowability, extrudability and buildability within the open time of 30 minutes. The samples for mechanical and thermal testing were printed based on the optimum printing parameters obtained from the printability tests.

6.3 Evaluation of effects of MEPCM on printing parameters

6.3.1 Experimental procedures

The printability of the cementitious ink materials is evaluated by their ‘flowability’, ‘extrudability’, and ‘buildability’, each described as follows. Flowability is an important parameter to ensure easy handling and transportation of the cementitious printing ink material from the mixer to the nozzle. In this study, the flow table test was conducted as per ASTM C230 to measure the flowability of the mixture within the open time up to 30 min. A cast bronze cone mold with 69.85 mm top diameter, 101.6 mm bottom diameter, and 20.8 mm height was filled with the

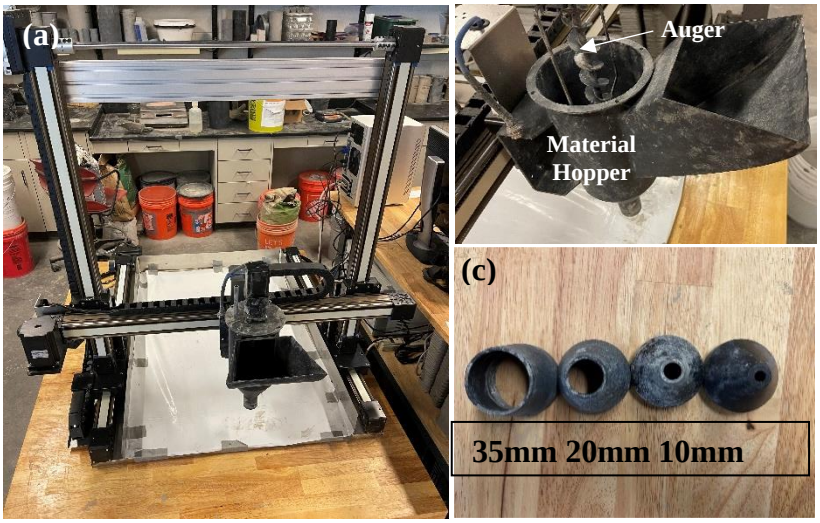

Figure 50: Printer System:
(a) Gantry printer; (b) printhead; (c) the printing nozzles

cementitious ink materials and then the cone was removed. Subsequently, the table was dropped for 25 times within the time of 60 s, allowing the mixture to freely spread out. After that, the average diameter of the spread mortar was measured in two perpendicular directions to indicate the flowability of the fresh mortar. The average of the three measurements was used as the flowability values of the mixtures. The ambient temperature of the laboratory was measured at a constant 21℃ for the duration of the testing.

Extrudability is defined as the workability of the cementitious ink material continuously extruded through the nozzles. The extrudability of the fresh mortar was evaluated by the continuity and stability of the extruded ink material from the nozzle with a diameter of 10 mm. The mortar was printed with a continuous length of 3500 mm long in a S-shaped pattern, with each "leg" of the print being 500 mm long. The extrudability was characterized by the quality and the longer distance over which the mortar could be extruded without breakage or change in the thickness of the printed layer. The nozzle was selected with a smaller opening from what was used to make test samples to assure that the mortar can be deposited with no liquid drainage or blockage of the nozzle. Three extrusion rates and three horizontal print head velocities were selected to study the effect of printing parameters on the extrudability of the mixtures. The extrusion rates included low (0.57 rps), moderate (1.0 rps), and high (1.7 rps) and horizontal print head velocity was adjusted for three classes of low (45 mm/s), medium (65 mm/s) and high (90 mm/s).

Another critical factor to consider for the layer extrusion method is buildability [150]. The term 'buildability refers to the ability of the ink material to retain its extruded shape and the resistance of the deposited mixture at the plastic stage to deformation under loads from the successive layers before it hardens. In this study, the buildability of materials was characterized by printing structures with eight layers of extruded ink material with the length of 250 mm and an

average width of 30 mm. A nozzle with an opening of 20 mm was selected and the printing parameters were kept constant at extrusion rate of 1.77 rps and print head velocity of 45 mm/s unit for all mixtures. The height of each layer was considered constant (14 mm) and the machine was designed to move up in 14 mm intervals. The buildability was quantified as in [151] by measuring the average vertical strain of each printed layer (ε_h) to characterize the shape retention of the fresh pastes. Also, the height to width ratio (h/w) of the printed element was recorded to describe the stability of the printed element with different volume fractions of MEPCM as compared to the reference mixture.

6.3.2 *Flowability*

Figure 51 (a) shows the flowability of the mortar mixtures with three volume loadings of MEPCM immediately and 30 min. after mixing, representing the open time for the printing process. As indicated by the results, the flowability of the mixtures reduced slightly within the 30 minutes of open time. This is important to ensure the consistency of the printability results that were obtained at different times within the open time. At lower volume loading of the Micronal® MEPCM (2.5%), the flow increased by 14% to 16.3 cm, comparing to the Ref mixture. This may be attributed to the spherical shape of MEPCM particles, which may act as a rolling lubricate to facilitate the slide of solid components such as fine aggregates in the mixture, see the first illustrative figure in Figure 51(b). As the MEPCM dosage increased, passing 2.5 vol%, there is a general trend of flowability decrease. This may be mainly attributed to the replacement of the equivalent volume of binder with the MEPCM particles that lowers the viscosity of the mixture, see the second figure in Figure 51 (b).

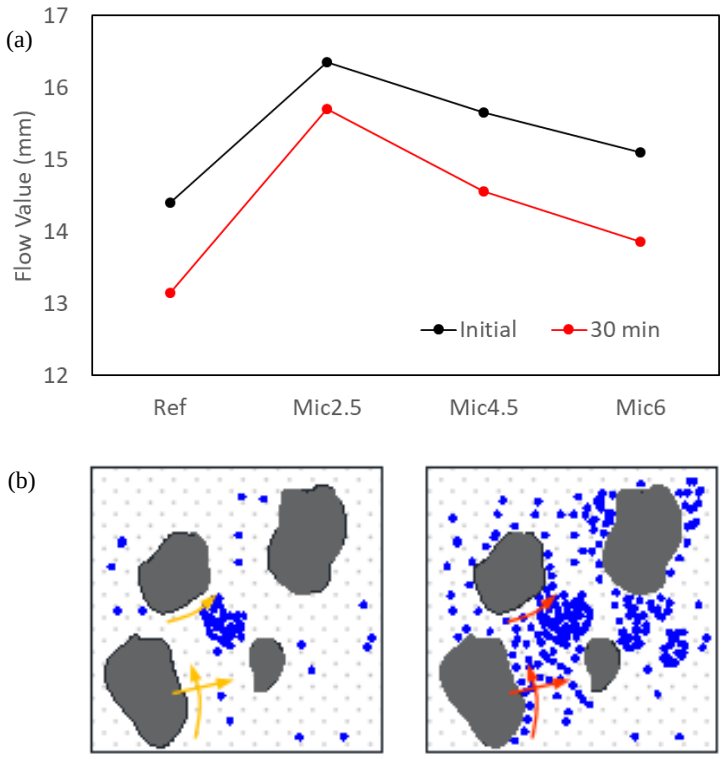

Figure 51: Material flow effects:
(a) Flowability of mixtures within the open time (30 min) and (b) schematic rolling effect of MEPCM on flowability

6.3.3 *Extrudability*

Table 16 shows the extrudability of the mixtures recorded at different extrusion rates and the print head velocities. The extrudability was assessed based on the visual observation and was categorized into four classes: 1) extrudable (E): the mixture extruded with no flaws and at the appropriate size close to the nozzle geometry; 2) over extruded (O): the mixture spread excessively - flow-out (F) during extrusion and the desired shape stability was not obtained; 3) Under extrudable (U): the printed bead was stretched and the desired shape stability was not obtained; and 4) Breakage (B): the printed bead was extruded discontinuously (teared). Figure 52 shows the selected images representing visual observation for each category.

6.3.4 *Buildability*

Figure 53 shows the effect of MEPCM content on the buildability of the mixtures. In this study, average strain of layers, average height of layers, and height to width ratio are measured to quantify the buildability of the mixtures with and without MEPCM. The results showed that the addition of 2.5 vol% MEPCM increased the average strain of layers and decreased the height to width ratio. This can indicate a reduction in the buildability of Mic2.5 samples compared to the reference mortar (Ref). This is in good agreement with the flowability of the Mic2.5 mixtures. The inclusion of the 2.5 vol% Micronal® MEPCM reduced the yield strength and viscosity of the mixtures owing to the rolling effect of their spherical particles. However, the higher loading volumes of MEPCM increased the buildability and the printed mixture retained its shape comparatively better than Mic2.5 yet lower than the Ref. This higher width of layers with MEPCM well demonstrates the effect of inclusion of MEPCM on the buildability of mixtures (Figure 53(d)).

Table 16. Extrudability of printing materials with different contents of PCM

Mixture	Extrusion rate (Low = 0.57 rps)			Extrusion rate (Moderate = 1 rps)			Extrusion rate (High = 1.7 rps)		
	Print head velocity (mm/s unit)			Print head velocity (mm/s unit)			Print head velocity (mm/s unit)		
	45	65	90	45	65	90	45	65	90
Ref	O	E	E	O	E	E	O	O	O
Mic2.5	O	E	E	O	E	E	O	O	O
Mic4.5	E	U	U	O	E	E	O	O	E
Mic6	E	B	U	E	E	U	O	E	E

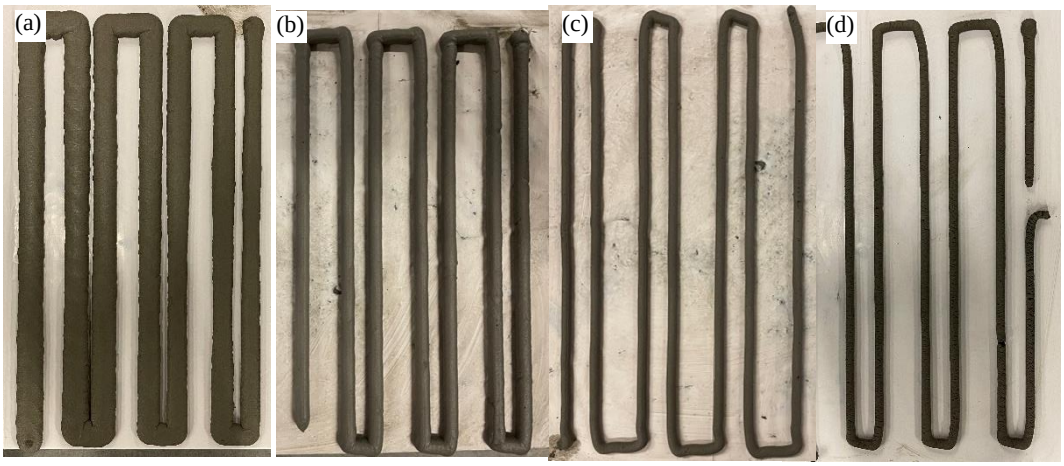

Figure 52: Visual representation of print quality for different extrusion rates and print head velocity:
(a) Over Extruded (thickness above 15 mm); (b) Extrudable (thickness between 10 – 15 mm); (c) Under Extruded (thickness below 10); (d) Breakage

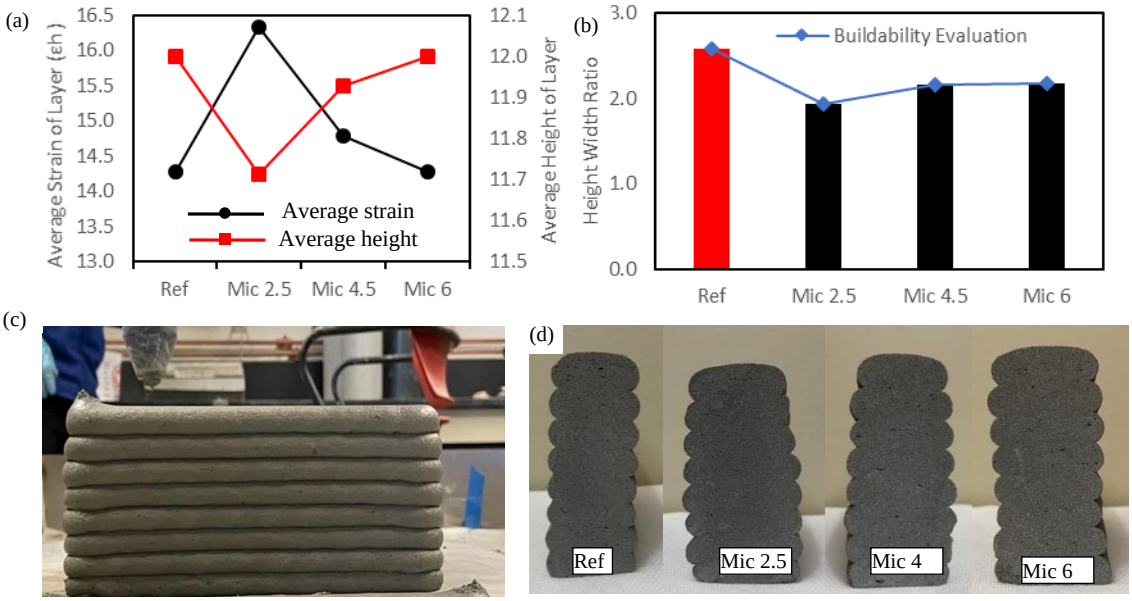

Figure 53: buildability properties of printed material:
(a) average strain and height of layer, (b) height width ratio, (c) printed structure for buildability assessment, and (d) cross section of printed Ref, Mic2.5, Mic4, and Mic6.

In this study, the extrusion rate and horizontal print head velocity were kept constant at extrusion rate of 1 rps and print head velocity of 65 mm/s unit for all mixtures.

The results showed that the printing parameters had a significant impact on the extrudability of the mixtures as the MEPCM volume loading varied. In general, the inclusion of higher contents of MEPCM required higher extrusion rate and print head velocity, which can be explained by the lower flowability of the mixtures with the addition of > 2.5 vol% MEPCM. In contrast, Ref and Mic2.5 required lower extrusion rates to achieve the desirable extrudability. According to the studies by Perrot et. al. [152–154],the extrusion rate is relative to the hydraulic conductivity of the ink material as it can cause the flow of liquid phase through the granular skeleton, leading to an undesirable extrusion. Therefore, it is critical to control the extrusion rate by taking the flowability of the ink material into account in order to reach a consistent printing. As can be seen from Table 16. Extrudability of printing materials with different contents of PCM, mismatching printing parameters led to printing of beads with undesirable extrusion in the forms of thicker or narrower layers. For mixtures with 6 vol% MEPCM at the extrusion rate of 0.57 rps and print head velocity of 65 mm/s the breakage was observed. In general, directly adding MEPCM microcapsules to printable cementitious premix is feasible, however, adjustments to the printing parameters may be needed.

6.4 Thermal properties of cementitious composites containing MEPCM

6.4.1 Energy storage capacity

The thermal energy storage capacities of cement paste and mortar containing various volume loadings of MEPCM were characterized through differential scanning calorimetry (DSC) (*TA Instrument Q2000,* scanning rate 10℃/min.). Table 17 summarizes the volume loading and thermal properties including heat of fusion (latent heat during phase change), ΔH_m, phase change

Table 17. DSC test results for cement paste and cement mortar containing MEPCM

Material	**w/c**	**Volume % of MEPCM**	**Heat of Fusion,** ΔH_m	**Phase Change Temp,** T_m	**Phase Change Temp,** T_s
			kJ/kg	℃	℃
Cement Paste + 6.5 vol% MEPCM	0.3	6.5	2.989	20.16	22.39
Cement Paste +16.5vol% MEPCM		16.5	7.207	20.09	22.40
Cement Paste +26.5vol% MEPCM		26.5	12.831	20.07	22.39
M68 Mortar + 2.5 vol% MEPCM	0.35*	2.5	0.909	21.08	22.29
M68 Mortar + 4.5 vol% MEPCM		4.5	1.678	21.07	22.01
M68 Mortar + 6 vol% MEPCM		6	2.307	21.08	22.29

* Water to binder ratio estimated based on the (proprietary) mixture information provided by the manufacturer

temperature (onset), T_m, and phase change temperature (finish), T_s, tested for each group of samples. Figure 54(a) shows the DSC traces obtained for cement paste containing 0, 6.5, 16.5, and 26.5 vol% of Micronal® microcapsules, which corresponds approximately with the volume loadings of MEPCM in the paste phase (excluding the fine aggregates and fillers) of Ref, Mic2.5, Mic4.5, and Mic6, respectively. The latent heat of the Micronal® benchmark was tested at 90.3kJ/kg with phase change onset temperature of 22℃, also see Figure 49; the latent heat of cement paste containing Micronal® MEPCM was tested roughly proportional to the weight percent of the PCM within the composite materials system. DSC samples were also prepared by mixing Micronal® MEPCM with the Laticrete M68 mortar to achieve volume loadings of 2.5% (Mic2.5), 4.5% (Mic4.5), and 6% (Mic6). Figure 54(b) shows the DSC traces of MEPCM charged M68 mortar, where the latent heat measured are also proportional to the wt% of the MEPCM inclusions as expected. It is noted that during mixing (and printing), the binder for the conglomerated Micronal® particles dissolves and the PCM microcapsules (2-3μm in size) uniformly distributed within the cementitious matrix, see Figure 54(c).

6.4.2 Thermal conductivity

The transient plane source (TPS) method originally developed by Gustafsson [121] was applied to measure the thermal conductivity and diffusivity of the cementitious composites. The TPS test method is based on the recorded temperature rise of a plane source that heats the surrounding sample to be measured. In a TPS test, a conducting pattern with negligible heat capacity (e.g., Kapton supported double spiraled nickel metal sensor as shown in Figure 55(a) serves simultaneously as the heat source and the temperature sensor. The initial electrical resistance of the TPS element, R_0, is first balanced in a Wheatstone bridge and, during the

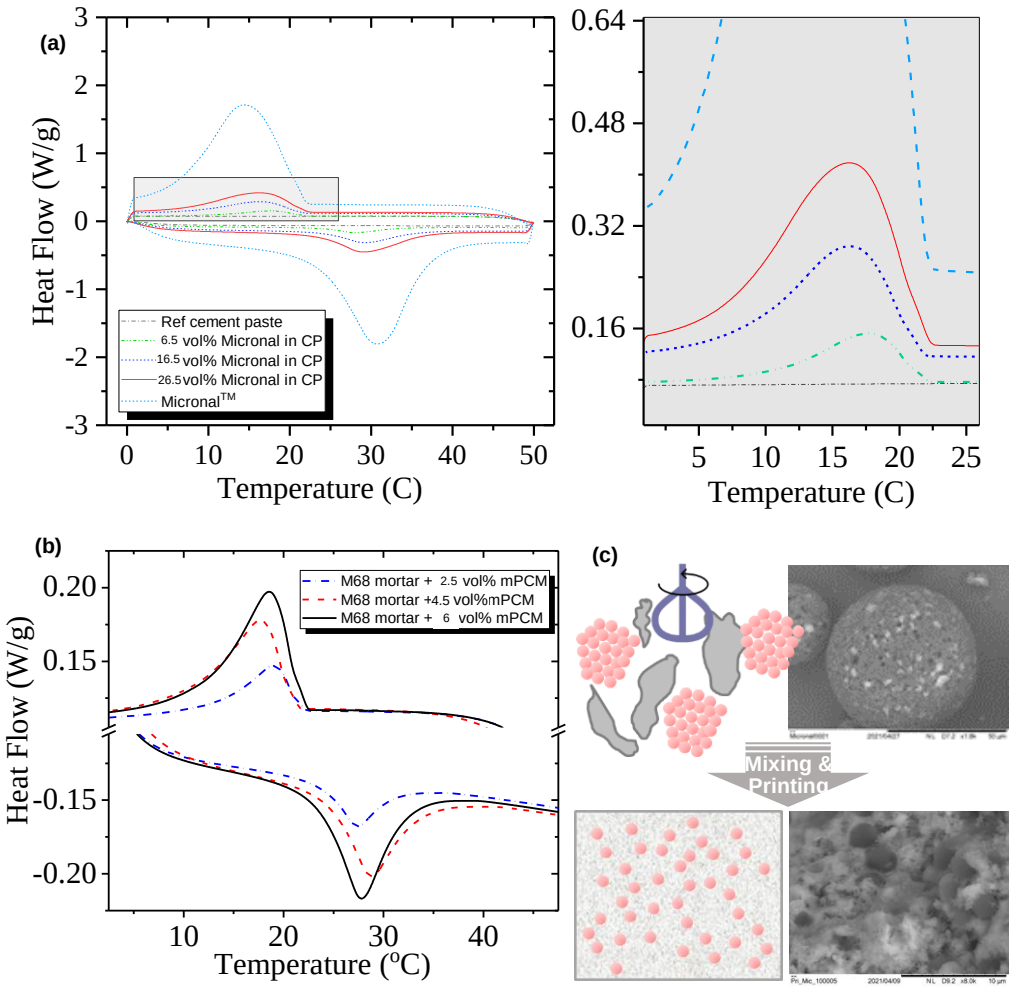

Figure 54: Differential scanning calorimetry (DSC) results obtained on cement paste and M68 mortars with Micronal® MEPCM:
DSC traces of cement paste containing various volume loadings of MEPCM; (b) DSC traces of M68 mortars containing MEPCM; and (c) illustrative figure and SEM images showing the distribution of Micronal® microcapsules within the printed material

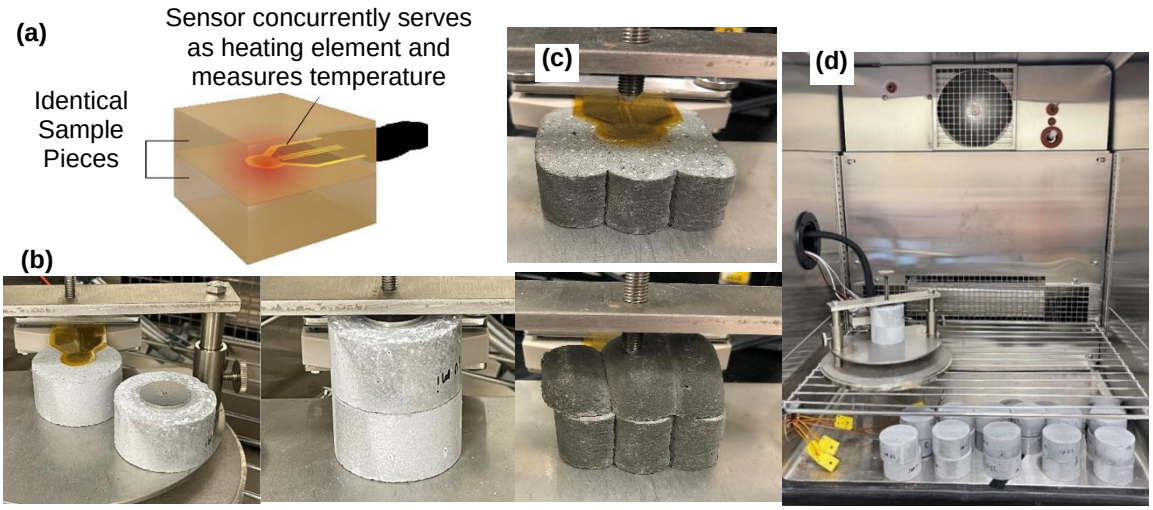

Figure 55: Transient plane source (TPS) test setup for thermal conductivity measurement: (a) illustrative figure showing the sensor and sample locations; (b) samples prepared for cast specimen; (c) TPS samples cut from 3D printed samples; and (d) test assembly in an environmental chamber for thermal conductivity measurements under various temperatures and

Through a process of iteration, the thermal conductivity k and thermal diffusivity κ of the tested material can be simultaneously obtained from one single transient recording [123]. For each sample type three pairs of samples were tested, both cast sample and printed samples as shown in Figure 55(b) and (c). Each sample pair consisted of two slices of cast or printed samples that are used to sandwich the TPS Kapton sensor. The TPS tests were conducted in an environmental chamber with controlled temperature and relative humidity (RH).Table 18 shows the summary of thermal conductivities and specific heat of both printed and cast samples of 3D printable cementitious composites containing Micronal® MEPCM.

Figure 56 shows the thermal conductivities and specific heat capacity of the cementitious composites measured at temperatures above the melting point of the encapsulated PCM. Previous work by the authors [155] demonstrated that the thermal properties of cementitious composites containing MEPCM showed similar results above and below the phase change point. The thermal conductivity for cast samples agrees with the workability tests discussed earlier. The inclusion of 2.5 vol% Micronal (Mic2.5) resulted in a higher workability of the mixture creating a more densely packed sample which results is higher thermal conductivity values due to the creation of better thermal pathways. For samples Mic4.5 and Mic6, Micronal® addition caused a decrease in the thermal conductivity, which can be attributed to the opposite of this, i.e., the lower workability resulting in the decreased results. Printed samples showed an inconsistent trend when compared with the cast samples. This may be due to the unpredictable compaction levels of printed samples. It is noted that the thermal conductivities of cast samples also do not show a clear trend with MEPCM dosage. This is likely due to the low thermal conductivity polymeric constituents added to the M68 mortar for workability improvement. The TPS method also measures the

Table 18. Thermal properties of the tested mixture groups

Mix ID	**MEPCM Volume Fraction**	**Thermal Conductivity** (Cast)	**Thermal Conductivity** (Printed)	**Specific Heat Capacity** (Cast)	**Specific Heat Capacity** (Printed)
	v_f (%)*	W $m^{-1}K^{-1}$	W $m^{-1}K^{-1}$	MJ/m^3K	MJ/m^3K
Ref	0.0	1.2637±0.022	0.9915±0.032	2.163±0.069	2.342±0.059
Mic2.5	2.5	1.1833±0.0165	0.9417±0.027	2.06±0.082	1.553±0.257
Mic4.5	4.5	1.2857±0.0176	0.8556±0.0078	2.023±0.004	2.233±0.034
Mic6	6	1.1613±0.0122	1.002±0.011	2.309±0.064	2.229±0.163

***** The density of samples was measured at room temperature and 35%RH.

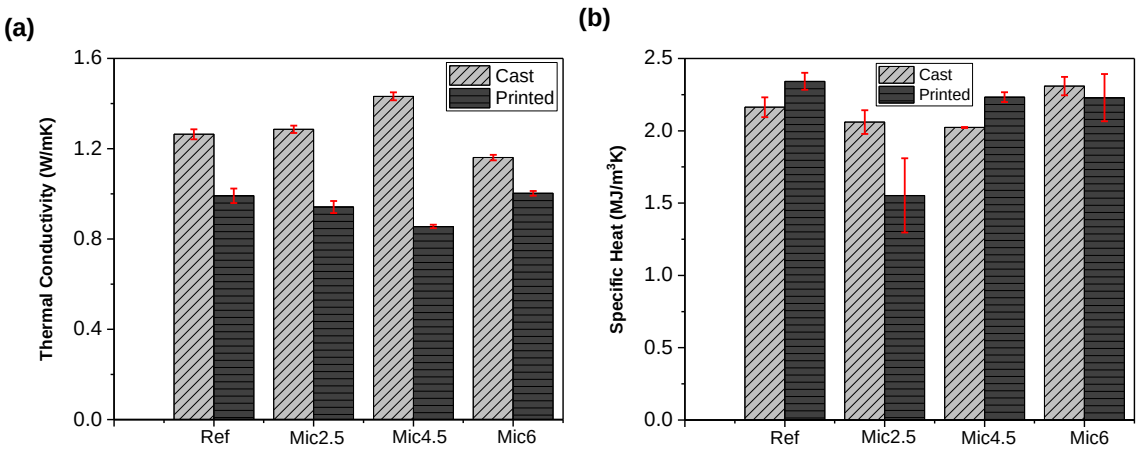

Figure 56: Thermal properties of printed LWCC tested through Transient Plane Source (TPS) method:
(a) Thermal conductivity; (b) Volumetric heat capacity above phase change temperature (sensible heat)

volumetric heat capacity of a sample based on the emissivity values tested. Volumetric heat capacity shows a mostly stable trend around 2000 kJ/m^3 for cast samples, while the printed samples show more variance in their results, mostly likely due to variation in porosity as previously discussed.

6.5 Microstructure and mechanical properties

6.5.1 Microstructures

Representative sections (including interlayer boundaries for printed samples) were cored/cut from the cured specimen and impregnated into epoxy pucks. The samples were then ground using a Buehler variable speed grinder/polisher from 120 grit to 1200 grit, before being polished to 1 µm using diamond polishing compound. For the fractured samples, a piece of dried paste representing each mixture was taken from the freshly broken sample. Loose debris was removed with compressed air and then imaged. The specimen was sputtered with a 20-30 nm layer of gold if charging was observed. The SEM images were taken using a Hitachi TM3030 Tabletop SEM.

Figure 57 presents the microstructure of cast and printed Ref and Mic6 (6 vol% MEPCM) samples after 28 days of curing. The magnification and the working distance were adjusted to investigate the effect of the casting/printing process on the microstructures of the samples. As indicated by the SEM images, the printed Ref sample (Figure 57(a)) has more porous microstructure in comparison with the cast counterparts, as indicated by the air pockets and voids. This is mainly due to lack of compaction during the screw-driven extrusion process despite it providing adequate homogeneity of the printed beads. The vibration compaction for cast samples densified the matrix more effectively, as expected. The inclusion of 6 vol%

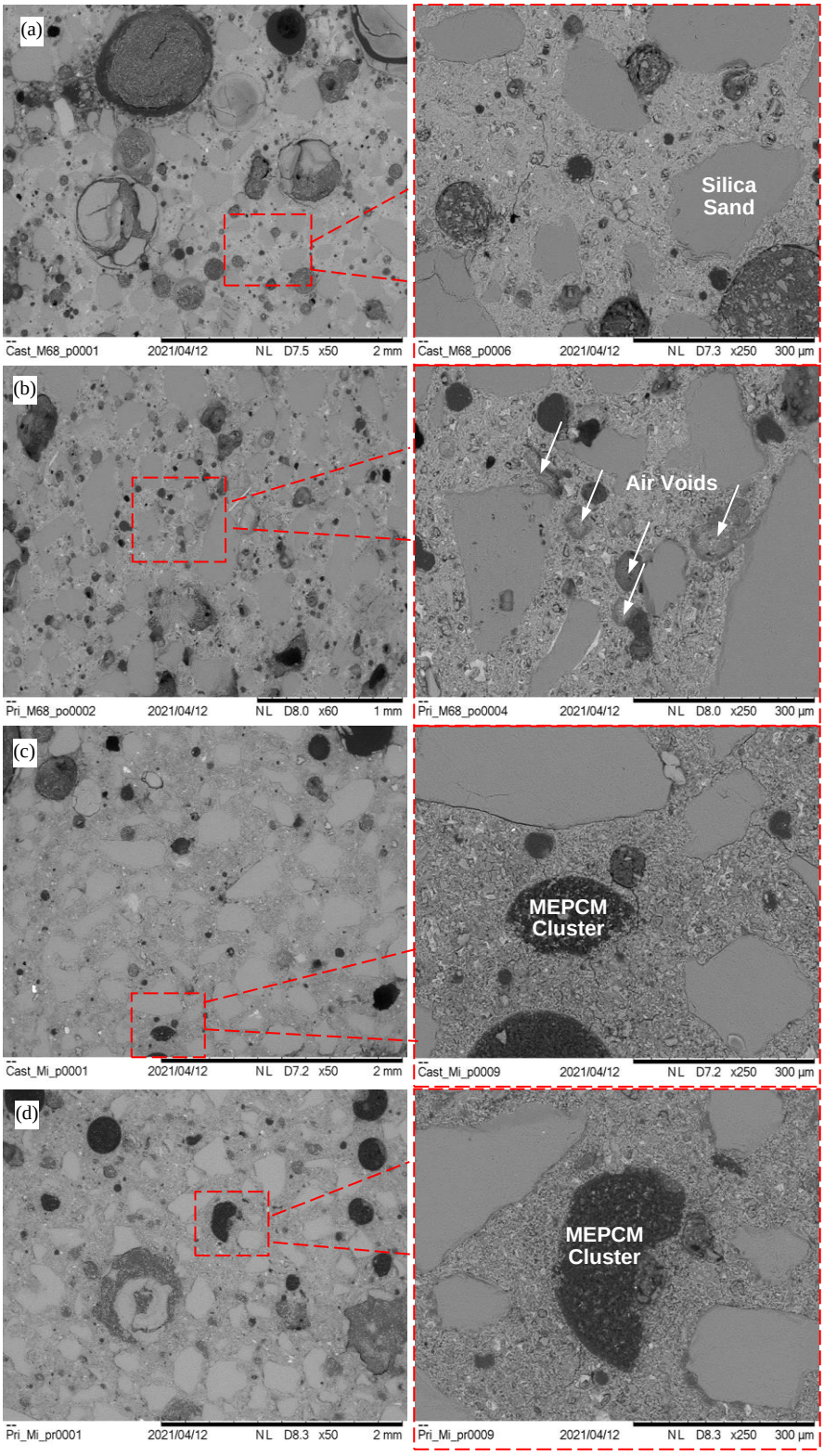

Figure 57: SEM images of cast vs. printed cementitious composite (M68) samples: (a) cast M68 mortar; (b) printed M68 mortar; (c) cast Mic6 mortar with 6 vol% MEPCM; and (d) printed Mic6 mortar with 6 vol% MEPCM

MEPCM densified the matrix of the printed samples due to the 'lubrication' effects as pointed in the previous section, leading to a dense microstructure (Figure 57 (d)). It can be seen that selected representative samples with MEPCM had similar density as compared to its cast counterpart (Figure 57 (c)). The lower air void content of the printed Mic6 can be attributed to the higher extrusion rate required during printing (see Table 16. Extrudability of printing materials with different contents of PCM). The addition of 6 vol% MEPCM reduced the flowability while increasing the buildability (green strength and yield strength) of the mixture, which necessitated the higher extrusion rate (Table 16). The higher extrusion rate combined with the rolling effect of MEPCM as illustrated in Figure 51 (b) – i.e., the microcapsules spherical shape can increase the particle packing density during extrusion and makes the solid skeleton slide over each other more effectively during the extrusion, collectively increased the compaction of the mixture during extrusion. During the mixing and the screw-driven extrusion, some conglomerates were disaggregated into smaller clusters or individual microcapsules and dispersed in the bulk paste.

6.5.2. Mechanical performance

In order to study the impacts of MEPCM on the mechanical properties of the 3D printed cementitious composite materials, printed samples charged with various volume loadings of MEPCM (Micronal®), i.e., Mic2.5, Mic4.5, and Mic6, were prepared using printing parameters identified in section 2.3. In this study reference samples and 2.5% MEPCM volume loading an extrusion rate of 0.57 rps and print head velocity of 65mm/s was used. For 4.5% and 6% volume loadings 0.57 rps and 45 mm/s and 1.7 rps and 65 mm/s were used respectively. These parameters were selected from the extrudable combinations based on their consistency and the ease of working

with the materials and printer. For each volume loading, five 50.8 mm diameter by 101.6 mm cylinders were casted for each specimen group listed in Table 19.

Additionally, nine 50.8 mm cubes were cut from a printed bar, see Figure 58 (a). These samples were then tested in X, Y, and Z orientations (three samples tested in each orientation). All samples were cured in a humidity (98%) and temperature (25℃) controlled curing room for 28 days after casting/printing before testing. Mechanical tests were performed using a 500kN INSTRON servo-hydraulic universal testing system as shown in Figure 58(b). The mechanical loading procedure was carried out in a displacement-control mode at the loading rate of 0.01 mm/min. To measure the elastic moduli of tested materials, the deformation (i.e., compressive strain) was measured using a pair of clamp-on extensometers (*Epsilon Tech*) with gauge length of 50 mm for cast cylinder samples. The setup of extensometers is shown in Figure 58 (c). A high-resolution Charge Coupled Device (CCD) camera was staged to record the damage and failure of the specimens, see Figure 58 (d). The tested specimens were preserved for scanning electron microscopy (SEM) analysis following the mechanical tests.

Table 19 present the elastic moduli of 3D printable cementitious composites containing MEPCM (cast) with various volume loading (2.5-6 vol%) tested after 28 days of curing. The elastic modulus is affected by both the physical properties of the added MEPCM and their volume fractions. For cementitious composites containing Micronal® the data shows a downward trend as the MEPCM volume fraction increases, see Table 19. These reductions resulted in a 7.7%, 24.5% and 30% reduction compared to the reference material for the Mic2.5, Mic4.5 and Mic6 respectively. It was found in the authors previous work [50,51,126,155–157] that shell properties

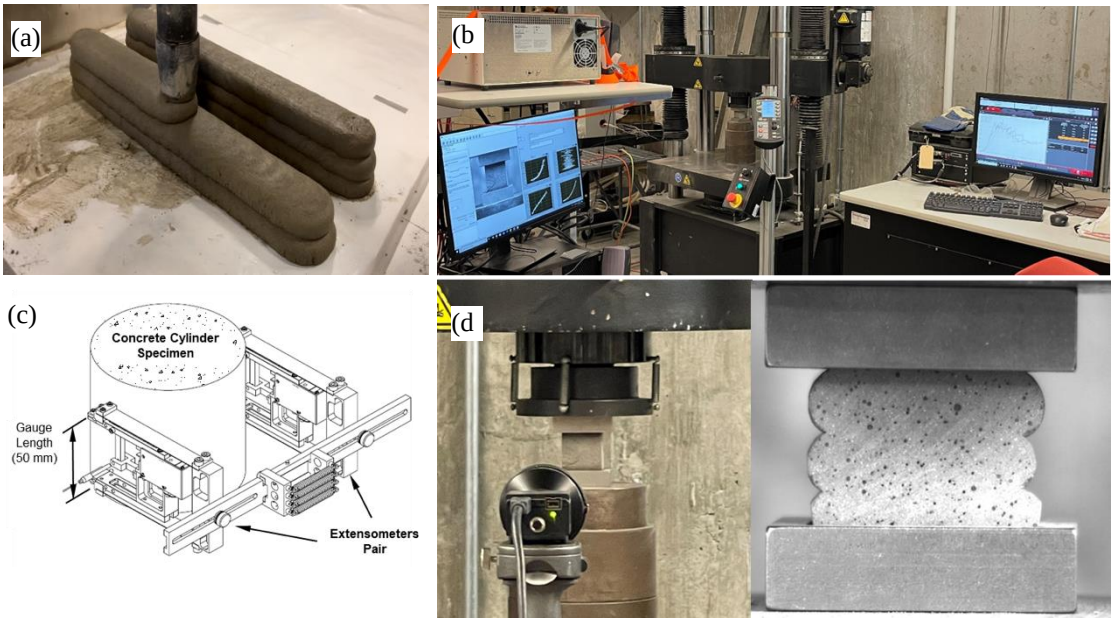

Figure 58: Mechanical property testing of printed LWCC: (a) Printing mechanical samples; (b) setup for mechanical test of cementitious composite samples; (c) extensimeter set up for cast cylinders; (d) compression test set up on printed samples

Table 19. Density, mechanical, and thermal properties of the tested mixture groups

Mix ID	MEPCM Volume Fraction	Density * (cast)	Density* (printed)	Elastic Modulus (cast)	Compressive Strength (cast)	Compressive Strength (Printed x)	Compressive Strength (Printed y)	Compressive Strength (Printed z)
	v_f (%)*	(kg/m^3)	(kg/m^3)	(GPa)	(MPa)	(MPa)	(MPa)	(MPa)
Reference	0.0	1793±19	1753±45	22.0±0.7	45.5±1.47	19.9±0.559	18.0±0.042	19.7±1.06
Mic2.5	2.5	1764±3	1681±15	20.3±1.3	43.1±0.311	19.8±2.932	20.9±0.827	19.9±0.55
Mic4.5	4.5	1786±12	1715±48	16.6±1.2	41.3±0.527	23.0±1.119	22.1±2.201	21.3±1.812
Mic6	6	1791±8	1739±20	15.4±0.8	42.1±0.459	17.8±1.079	18.4±3.326	19.2±2.728

***** The density of samples was measured at room temperature and 45%RH.
Each cylinder was made in three layers using vibration as the method of compaction

(stiffness), shell thickness, and the particle size of the micro-inclusion all have an impact on the elastic properties of cementitious composites. Micronal® has an acrylic polymer shell based on its encapsulation method [158], which has a significantly lower stiffness than that of the surrounding mortar. As a result, the elastic modulus of 3D printable cementitious composites decreases proportionally as volume loading of MEPCM increases.

Figure 56 (b) shows the compressive strength of both cast and 3D printed samples tested under different orientations. In general, the compressive strength of cementitious composites with MEPCM depends mostly on the volume loading (i.e., 2.5%, 4.5%, 6%) and physical properties of the MEPCM incorporated (e.g., particle size and shell material). However, it is noted that in the case of printed cementitious composites with MEPCM, there is an increase in the compressive strength in comparison with the printed reference when the vol% of MEPCM is below 4.5%. This increase of strength can be attributed to the spherical nature of the MEPCM inclusion, which leads to better flowability and improved compaction of the material as it is extruded – i.e., reduction of air voids within the printed materials. The cast samples, however, show that when mechanical compaction methods (i.e., vibration) are used, the weak discontinuities created by the MEPCM particles becomes the dictating factor controlling the strength of the material. The Mic6 samples can be seen to have slightly higher strength than the Mic4.5 samples, though the standard deviation of the samples overlap, possibly indicating a plateau of strength loss. The decrease in compressive strength of the printed samples as compared to the cast samples is partially due to the different compaction states [159]. During printing, the compaction of the material relies mostly on the pressure generated by the rotating screw, while cast samples use vibration as the compaction method. Figure 60 shows the failure mode of printed sample with 6 vol% MEPCM. The sample

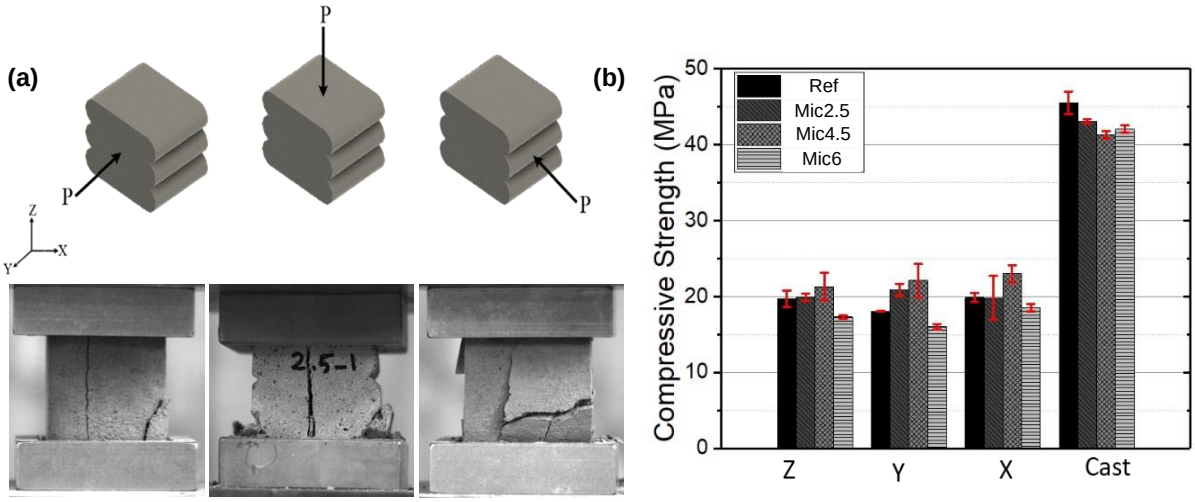

Figure 59: Mechanical properties of printed LWCC:
(a) testing orientation for printed samples; (b) mechanical test results as functions of the test orientation and volume loadings of MEPCM

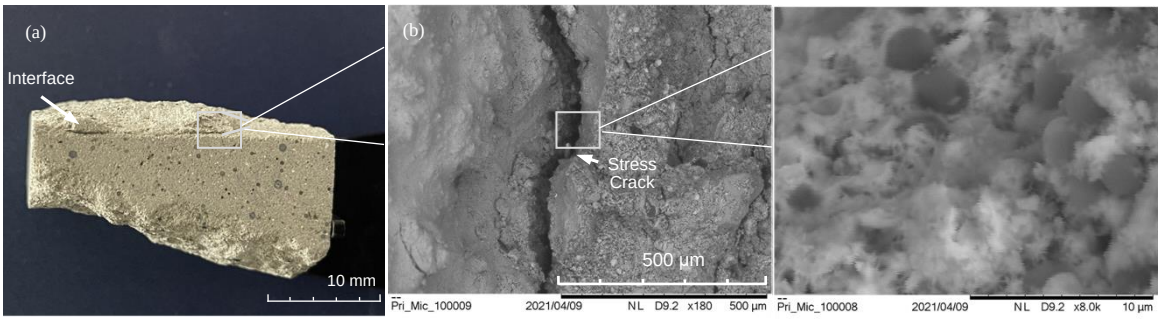

Figure 60: Failure mode of printed sample with Mic6:
(a) mechanical fracture piece showing macrocrack formed during failure; (b) closed-up view of stress crack from mechanical load; and (c) Micronal© particle in cement matrix (fracture surface)

failed at both interlayer zones (between two successive printed layers), as well as the shear zone through the bulk mortar (i.e., beads). The interfacial fracture of the two successive layers is mainly due to the weak bonds at the interlayer that can be attributed to the increase in the stiffness of the mixture when a high volume loading of MEPCM was incorporated. The flowability results showed that the inclusion of the 6 vol% Micronal® MEPCM increased the stiffness of the fresh mixture and reduced the flowability by 15%. The lowered printability can reduce the ability of the freshly printed layers to form a well-infused interface with the existing layer, leading to reduction of the interlayer bond strength. On the other hand, incorporation of spherical MEPCM with low stiffness and the low bonding strength with the surrounding cement paste can generate weak interfacial transition zone (ITZ) around the MEPCM particle [50]. Figure 60 shows the fractured sample piece obtained from a printed Mic6 sample tested under compressive loading, where a crack is shown initiated at the filament interface. Collectively, these three mechanisms lead to lower mechanical strength of the printed samples as compared to their cast counterparts.

Chapter 7. Conclusions

This dissertation focused on the thermomechanical performance of functional cementitious composites that incorporated lightweight micro-sized fillers (i.e., fly ash cenospheres, hollow glass microspheres, thermoplastic microspheres, and EPS beads), lightweight aggregates (i.e., expanded clay), and micro-encapsulated phase change materials (i.e., CenoPCM and Micronal©). A multiscale approach was taken for this research that evaluated the mechanical and thermal performance at the mortar, concrete, and scaled panel levels. Further analysis was conducted to evaluate the feasibility of the performance of MEPCM materials when incorporated into a concrete "ink" for 3d printing.

Despite the individual research that has been conducted for each type of the aforementioned functional aggregates/ filler materials, there still lacks a comprehensive investigation on the mechanical and thermal performance of cementitious composites containing these emerging micro-sized functional fillers/ additives. While the use of lightweight aggregate is common, it is less common to see its use in structural applications. Unlike most lightweight coarse aggregates with irregular shape and porous surfaces (e.g., expanded shale clay), the lightweight particulate aggregates/ fillers discussed in this dissertation have much smaller particle size and are mostly spherical in shape (or have a core-shell configuration). This will allow the fine-tuning of material properties by varying material parameters of the filler particles such as particle size, shell thickness (stiffness), and volume fraction. Lightweight concrete and cementitious composites are increasingly studied because they reduce structural self-weight loads and have potential for energy-savings in buildings. With new technologies and more push to reduce energy consumption of the building sector more research has looked to identify ways to introduce phase change materials into cementitious composites on larger scales. In this dissertation, a series of experimental and numerical studies were carried out to investigate the

effects of various lightweight fillers (LWFs) and micro-encapsulated phase change materials (MEPCMs) on the mechanical and thermal properties of lightweight cementitious composites (LWCCs). This study evaluated the use of various LWFs to identify the most effective implementation to reduce both self-weight and thermal conductivity or increase the overall thermal energy storage capacity of the material while maintaining a high mechanical strength. The following conclusions are drawn from this study:

- The mechanical and thermal properties of lightweight cementitious composites, or LWCC, are greatly affected by the type and properties of the lightweight functional filler (LWF) used. To achieve the desired lightweight feature while still maintaining adequate mechanical properties, careful selection and efficient utilization of LWF materials is imperative. Thermal properties of LWCCs are primarily dictated by the volume fraction of LWF and they are insensitive to the type of LWF used; on the other hand, the mechanical properties of LWCC are greatly affected by the LWF particle properties including the size, shell thickness (stiffness), and interfacial bonding between the particles and cementitious binder. Because of the high strength-to-unit weight ratio, most fly ash cenospheres (FAC) and hollow glass microspheres (HGM) with higher density (e.g., H50 and S60) are suitable for producing lightweight cementitious composite (LWCC) materials that may be used for structural load bearing, as long as the LWF volume fraction is controlled within a reasonable range.
- Increasing the volume fraction of MEPCM leads to the decrease of mechanical properties in general. However, cementitious composites containing the CenoPCM have significantly higher strength that those with polymer encapsulated PCM with the same MEPCM volume loading – while at lower volume fractions, the compressive strength of cementitious composites with CenoPCM surpasses the reference mortar likely due to the reduced air content because of

the improved workability. A similar trend was observed for elastic moduli. The rigid shell of FAC provides strong support of the encapsulated PCM within cementitious systems, leading to radically higher strength and stiffness (elastic modulus). Thermal conductivities of cementitious composites containing both types of MEPCM show a declining trend as the volume percentage of MEPCM increases. Cement composite with CenoPCM shows higher thermal conductivity overall due to the higher thermal conductivity of FAC shell than that of the polymer microcapsules.

- While full scale guarded hotbox testing is time consuming and costly this dissertation demonstrated that using a small-scale calibrated hot box and scaled-down specimen to evaluate the performance of building envelope elements is feasible. It has the merits of drastically lower experimental costs and experimentation time. The developed small-scale calibrated hot box equipment can be applied to both steady-state and transient heat transfer tests of building envelopes. Further the developed hotbox testing showed that the concrete produced using the micro sized functional additives were both effective as thermal barriers as well as able to withstand mechanical loads in a sandwich panel configuration.
- Incorporating micro-size fly ash cenospheres (FAC) into the cementitious matrix can effectively reduce the density and thermal conductivity of concrete by inducing a micro-cellular structure to the matrix phase. The strong shell and small particle size of FAC provide barriers to hinder crack propagation. SEM analysis performed on the mechanically tested LWC samples revealed that FAC with smaller particle size and thicker shell walls would survive the mechanical loading and show “pull-out” failure. In addition, introducing small and spherical FAC particles may also improve the rheological properties of concrete by allowing the FAC to roll among angular aggregates during mixing.

- The use of micro sized functional fillers/admixtures demonstrated that their use could be promising because of a two-fold application, as a viscosity modifier as well as demonstrating at 6% volume inclusion a nearly 50% reduction in temperature amplitude when compared to a reference sample under the same conditions. MEPCM affected the printability of the cementitious ink material in different ways depending on the volumetric loading level. The results showed that the lower volume loading of the Micronal® MEPCM (2.5%) increased the flowability as compared to the Ref mixture. This may be attributed to the spherical shape of MEPCM particles, which act as a rolling lubricant to facilitate the slide of solid components such as fine aggregates in the mixture. However, as the MEPCM dosage increased, a decrease of flowability was observed. Such reduction in the flowability with higher contents of MEPCM was accompanied by the improvement of buildability of the mixture. Thermal cycling tests performed on hollow cylindrical specimens printed with the reference and MEPCM charged mortar materials indicated that microencapsulated PCM materials (MEPCMs) are a potentially good candidate as an inclusion phase for 3D-printable cementitious composite materials to improve building's thermal and energy performance. Thermal cycling tests performed on hollow cylindrical specimens printed with the reference and MEPCM charged mortar materials indicated that microencapsulated PCM materials (MEPCMs) are a potentially good candidate as an inclusion phase for 3D-printable cementitious composite materials to improve building's thermal and energy performance.

Bibliography

[1] Shafigh P, Asadi I, Mahyuddin NB. Concrete as a thermal mass material for building applications - A review. J Build Eng 2018;19:14–25. https://doi.org/10.1016/j.jobe.2018.04.021.

[2] D&R International. 2011 Buildings Energy Data Book. U.S. Department of Energy; 2012.

[3] U.S Energy Information Administration. Annual Energy Outlook 2019 with projections to 2050. Washington, DC: U.S. Energy Information Admistration; 2019.

[4] Ineternational Energy Agency. Transition to Sustainable Buildings: Strategies and Opportunites to 2050. Paris: 2013. https://doi.org/10.1787/9789264202955-en.

[5] Kim T, Tae S, Roh S. Assessment of the CO2 emission and cost reduction performance of a low-carbon-emission concrete mix design using an optimal mix design system. Renew Sustain Energy Rev 2013;25:729–41. https://doi.org/10.1016/j.rser.2013.05.013.

[6] Ramkumar VR, Murali G, Asrani NP, Karthikeyan K. Development of a novel low carbon cementitious two stage layered fibrous concrete with superior impact strength. J Build Eng 2019;25:100841. https://doi.org/10.1016/j.jobe.2019.100841.

[7] Sathanandam T, Awoyera PO, Vijayan V, Sathishkumar K. Low carbon building: Experimental insight on the use of fly ash and glass fibre for making geopolymer concrete. Sustain Environ Res 2017;27:146–53. https://doi.org/10.1016/j.serj.2017.03.005.

[8] Kurpińska M, Karwacki J, Maurin A, Kin M. Measurements of thermal conductivity of LWC cement composites using simplified laboratory scale method. Materials (Basel) 2021;14:1–17. https://doi.org/10.3390/ma14061351.

[9] Heath A, Paine K, Goodhew S, Ramage M, Lawrence M. The potential for using geopolymer concrete in the UK. Proc Inst Civ Eng Constr Mater 2013;166:195–203. https://doi.org/10.1680/coma.12.00030.

[10] Kramar D, Bindiganavile V. Mechanical properties and size effects in lightweight mortars containing expanded perlite aggregate. Mater Struct 2011;44:735–48. https://doi.org/10.1617/s11527-010-9662-0.

[11] Lanzón M, García-Ruiz PA. Lightweight cement mortars: Advantages and inconveniences of expanded perlite and its influence on fresh and hardened state and durability. Constr Build Mater 2008;22:1798–806. https://doi.org/10.1016/j.conbuildmat.2007.05.006.

[12] Lu Z, Xu B, Zhang J, Zhu Y, Sun G, Li Z. Preparation and characterization of expanded perlite/paraffin composite as form-stable phase change material. Sol Energy 2014;108:460–6. https://doi.org/10.1016/j.solener.2014.08.008.

[13] Lotfy A, Hossain KMA, Lachemi M. Lightweight Self-consolidating Concrete with Expanded Shale Aggregates: Modelling and Optimization. Int J Concr Struct Mater 2015;9:185–206. https://doi.org/10.1007/s40069-015-0096-5.

[14] American Society for Testing and Materials. Standard Specification for Lightweight Aggregates for Structural Concrete. 2017. https://doi.org/10.1520/C0330.

[15] America Concrete Institute. ACI 211.2: Standard Practice for Selecting Proportions for

Structural Lightweight Concrete. 1998.

[16] Fantucci S, Garbaccio S, Lorenzati A, Perino M. Thermo-economic analysis of building energy retrofits using VIP - Vacuum Insulation Panels. Energy Build 2019;196:269–79. https://doi.org/10.1016/j.enbuild.2019.05.019.

[17] Bossche N Van Den, Moens J, Janssens A, Delvoye E. Thermal performance of VIP panels : Assessment of the edge effect by experimental and numerical analysis . Res Build Phys Proc 1st Cent Eur Symp Build Physics 2009:p.279-286.

[18] Voellinger T, Bassi A, Heitel M. Facilitating the incorporation of VIP into precast concrete sandwich panels. Energy Build 2014;85:666–71. https://doi.org/10.1016/j.enbuild.2014.05.038.

[19] Zach J, Peterková J, Dufek Z, Sekavčnik T. Development of vacuum insulating panels (VIP) with non-traditional core materials. Energy Build 2019;199:12–9. https://doi.org/10.1016/j.enbuild.2019.06.026.

[20] Navarro L, de Gracia A, Colclough S, Browne M, McCormack SJ, Griffiths P, et al. Thermal energy storage in building integrated thermal systems: A review. Part 1. active storage systems. Renew Energy 2016;88:526–47. https://doi.org/10.1016/j.renene.2015.11.040.

[21] Rempel AR, Rempel AW. Rocks, clays, water, and salts: Highly durable, infinitely rechargeable, eminently controllable thermal batteries for buildings. vol. 3. 2013. https://doi.org/10.3390/geosciences3010063.

[22] Souayfane F, Fardoun F, Biwole PH. Phase change materials (PCM) for cooling applications in buildings: A review. Energy Build 2016;129:396–431. https://doi.org/10.1016/j.enbuild.2016.04.006.

[23] Ma P, Wang LS, Guo N. Energy storage and heat extraction - From thermally activated building systems (TABS) to thermally homeostatic buildings. Renew Sustain Energy Rev 2015;45:677–85. https://doi.org/10.1016/j.rser.2015.02.017.

[24] Hasan A, McCormack SJ, Huang MJ, Norton B. Energy and cost saving of a photovoltaic-phase change materials (PV-PCM) System through temperature regulation and performance enhancement of photovoltaics. Energies 2014;7:1318–31. https://doi.org/10.3390/en7031318.

[25] Zhu L, Hurt R, Correia D, Boehm R. Detailed energy saving performance analyses on thermal mass walls demonstrated in a zero energy house. Energy Build 2009;41:303–10. https://doi.org/10.1016/j.enbuild.2008.10.003.

[26] Wahid MA, Hosseini SE, Hussen HM, Akeiber HJ, Saud SN, Mohammad AT. An overview of phase change materials for construction architecture thermal management in hot and dry climate region. Appl Therm Eng 2017;112:1240–59. https://doi.org/10.1016/j.applthermaleng.2016.07.032.

[27] He Y, Zhang Y, Zhang C, Zhou H. Energy-saving potential of 3D printed concrete building with integrated living wall. Energy Build 2020;222:110110. https://doi.org/10.1016/j.enbuild.2020.110110.

[28] Patel AJ. Study of pore structure effect on durability and strength of concrete incorporating of ceramic waste. RK University, 2020.

[29] Li VC. Advances in ECC Research 2019.

[30] Şahmaran M, Li VC. Durability properties of micro-cracked ECC containing high volumes fly ash. Cem Concr Res 2009;39:1033–43. https://doi.org/10.1016/j.cemconres.2009.07.009.

[31] degradation 5 S. Engineered Cementitious Composites (Ecc) – Tailored Composites through Micromechanical Modeling. Can Soc Civ Eng 1997:1–38.

[32] Li VC. On Engineered Cementitious Composites (ECC). J Adv Concr Technol 2003;1:215–30. https://doi.org/10.3151/jact.1.215.

[33] Li VC, Bos FP, Yu K, McGee W, Ng TY, Figueiredo SC, et al. On the emergence of 3D printable Engineered, Strain Hardening Cementitious Composites (ECC/SHCC). Cem Concr Res 2020;132:106038. https://doi.org/10.1016/j.cemconres.2020.106038.

[34] Li VC. Tailoring ECC for Special Attributes: A Review. Int J Concr Struct Mater 2012;6:135–44. https://doi.org/10.1007/s40069-012-0018-8.

[35] Yun TS, Jeong YJ, Han TS, Youm KS. Evaluation of thermal conductivity for thermally insulated concretes. Energy Build 2013;61:125–32. https://doi.org/10.1016/j.enbuild.2013.01.043.

[36] Zhang Q, Li VC. Development of durable spray-applied fire-resistive Engineered Cementitious Composites (SFR-ECC). Cem Concr Compos 2015;60:10–6. https://doi.org/10.1016/j.cemconcomp.2015.03.012.

[37] Oreshkin D, Semenov V, Rozovskaya T. Properties of Light-weight Extruded Concrete with Hollow Glass Microspheres. Procedia Eng 2016;153:638–43. https://doi.org/10.1016/j.proeng.2016.08.214.

[38] Vijay K, Murmu M, Deo S V. Bacteria based self healing concrete – A review. Constr Build Mater 2017;152:1008–14. https://doi.org/10.1016/j.conbuildmat.2017.07.040.

[39] Gilford J, Hassan MM, Rupnow T, Barbato M, Okeil A, Asadi S. Dicyclopentadiene and Sodium Silicate Microencapsulation for Self-Healing of Concrete. J Mater Civ Eng 2014;26:886–96. https://doi.org/10.1061/(ASCE)MT.1943-5533.0000892.

[40] Xu B, Li Z. Paraffin/diatomite composite phase change material incorporated cement-based composite for thermal energy storage. Appl Energy 2013;105:229–37. https://doi.org/10.1016/j.apenergy.2013.01.005.

[41] Sakulich AR, Bentz DP. Incorporation of phase change materials in cementitious systems via fine lightweight aggregate. Constr Build Mater 2012;35:483–90. https://doi.org/10.1016/j.conbuildmat.2012.04.042.

[42] Aguayo M, Das S, Castro C, Kabay N, Sant G, Neithalath N. Porous inclusions as hosts for phase change materials in cementitious composites: Characterization, thermal performance, and analytical models. Constr Build Mater 2017;134:574–84. https://doi.org/10.1016/j.conbuildmat.2016.12.185.

[43] Kim HK, Jeon JH, Lee HK. Workability, and mechanical, acoustic and thermal properties of lightweight aggregate concrete with a high volume of entrained air. Constr Build Mater 2012;29:193–200. https://doi.org/10.1016/j.conbuildmat.2011.08.067.

[44] Li P, Wu H, Liu Y, Yang J, Fang Z, Lin B. Preparation and optimization of ultra-light and thermal insulative aerogel foam concrete. Constr Build Mater 2019;205:529–42. https://doi.org/10.1016/j.conbuildmat.2019.01.212.

[45] Real S, Gomes MG, Moret Rodrigues A, Bogas JA. Contribution of structural lightweight aggregate concrete to the reduction of thermal bridging effect in buildings. Constr Build Mater 2016;121:460–70. https://doi.org/10.1016/j.conbuildmat.2016.06.018.

[46] Zhang B, Poon CS. Use of Furnace Bottom Ash for producing lightweight aggregate concrete with thermal insulation properties. J Clean Prod 2015;99:94–100. https://doi.org/10.1016/j.jclepro.2015.03.007.

[47] Huang X, Ranade R, Zhang Q, Ni W, Li VC. Mechanical and thermal properties of green lightweight engineered cementitious composites. Constr Build Mater 2013;48:954–60. https://doi.org/10.1016/j.conbuildmat.2013.07.104.

[48] Hanif A, Lu Z, Cheng Y, Diao S, Li Z. Effects of Different Lightweight Functional Fillers for Use in Cementitious Composites. Int J Concr Struct Mater 2017;11:99–113. https://doi.org/10.1007/s40069-016-0184-1.

[49] Hanif A, Lu Z, Li Z. Utilization of fly ash cenosphere as lightweight filler in cement-based composites – A review. Constr Build Mater 2017;144:373–84. https://doi.org/10.1016/j.conbuildmat.2017.03.188.

[50] Brooks AL, Zhou H, Hanna D. Comparative study of the mechanical and thermal properties of lightweight cementitious composites. Constr Build Mater 2018;159:316–28. https://doi.org/10.1016/j.conbuildmat.2017.10.102.

[51] Zhou H, Brooks AL. Thermal and mechanical properties of structural lightweight concrete containing lightweight aggregates and fly-ash cenospheres. Constr Build Mater 2019;198:512–26. https://doi.org/10.1016/j.conbuildmat.2018.11.074.

[52] Kalnaes SE, Jelle BP. Phase change materials and products for building applications: A state-of-the-art review and future research opportunities. Energy Build 2015;94:150–76. https://doi.org/10.1016/j.enbuild.2015.02.023.

[53] Konuklu Y, Ostry M, Paksoy HO, Charvat P. Review on using microencapsulated phase change materials (PCM) in building applications. Energy Build 2015;106:134–55. https://doi.org/10.1016/j.enbuild.2015.07.019.

[54] Ricklefs A, Thiele AM, Falzone G, Sant G, Pilon L. Thermal conductivity of cementitious composites containing microencapsulated phase change materials. Int J Heat Mass Transf 2017;104:71–82. https://doi.org/10.1016/j.ijheatmasstransfer.2016.08.013.

[55] Young BA, Fujii AM, Thiele AM, Kumar A, Sant G, Taciroglu E PL, Young BA, Fujii AMK, Thiele AM, Kumar A, Sant G, et al. Effective elastic moduli of core-shell-matrix composites. Mech Mater 2016;92:94–106. https://doi.org/10.1016/j.mechmat.2015.09.006.

[56] Falzone G, Falla GP, Wei Z, Zhao M, Kumar A, Bauchy M, et al. The influences of soft and stiff inclusions on the mechanical properties of cementitious composites. Cem Concr Compos 2016;71:153–65. https://doi.org/10.1016/j.cemconcomp.2016.05.008.

[57] Liu F, Wang J, Qian X. Integrating phase change materials into concrete through microencapsulation using cenospheres. Cem Concr Compos 2017;80:317–25. https://doi.org/10.1016/j.cemconcomp.2017.04.001.

[58] de Gennaro R, Langella A, D'Amore M, Dondi M, Colella A, Cappelletti P, et al. Use of zeolite-rich rocks and waste materials for the production of structural lightweight concretes. Appl Clay Sci 2008;41:61–72. https://doi.org/10.1016/j.clay.2007.09.008.

[59] Ke Y, Beaucour a. L, Ortola S, Dumontet H, Cabrillac R. Influence of volume fraction and characteristics of lightweight aggregates on the mechanical properties of concrete. Constr Build Mater 2009;23:2821–8. https://doi.org/10.1016/j.conbuildmat.2009.02.038.

[60] Chandra S, Berntsson L. Lightweight Aggregate Concrete: Science, Technology, and Applications. New York: Noyes Publications; 2002.

[61] Aglan H, Shebl S, Morsy M, Calhoun M, Harding H, Ahmad M. Strength and toughness improvement of cement binders using expandable thermoplastic microspheres. Constr Build Mater 2009;23:2856–61. https://doi.org/10.1016/j.conbuildmat.2009.02.031.

[62] Wu Y, Wang JY, Monteiro PJM, Zhang MH. Development of ultra-lightweight cement composites with low thermal conductivity and high specific strength for energy efficient buildings. Constr Build Mater 2015;87:100–12. https://doi.org/10.1016/j.conbuildmat.2015.04.004.

[63] Xu B, Ma H, Hu C, Yang S, Li Z. Influence of curing regimes on mechanical properties of magnesium oxychloride cement-based composites. Constr Build Mater 2016;102:613–9. https://doi.org/10.1016/j.conbuildmat.2015.10.205.

[64] Hanif A, Parthasarathy P, Ma H, Fan T, Li Z. Properties improvement of fly ash cenosphere modified cement pastes using nano silica. Cem Concr Compos 2017;81:35–48. https://doi.org/10.1016/j.cemconcomp.2017.04.008.

[65] Joseph K V, Francis F, Chacko J, Das P, Hebbar G. FLY Ash Cenosphere Waste Formation In Coal Fired Power Plants And Its Applicationas A Structural Material- A Review. Int J Eng Res Technol 2013;2:18–21.

[66] Xi B, Zhou Y, Yu K, Hu B, Huang X, Sui L, et al. Use of nano-SiO2 to develop a high performance green lightweight engineered cementitious composites containing fly ash cenospheres. J Clean Prod 2020;262:121274. https://doi.org/10.1016/j.jclepro.2020.121274.

[67] Sayadi AA, Tapia J V, Neitzert TR, Clifton GC. Effects of expanded polystyrene (EPS) particles on fire resistance, thermal conductivity and compressive strength of foamed concrete. Constr Build Mater 2016;112:716–24. https://doi.org/10.1016/j.conbuildmat.2016.02.218.

[68] Madandoust R, Ranjbar MM, Yasin Mousavi S. An investigation on the fresh properties of self-compacted lightweight concrete containing expanded polystyrene. Constr Build

Mater 2011;25:3721–31. https://doi.org/10.1016/j.conbuildmat.2011.04.018.

[69] Xu Y, Jiang L, Xu J, Li Y. Mechanical properties of expanded polystyrene lightweight aggregate concrete and brick. Constr Build Mater 2012;27:32–8. https://doi.org/10.1016/j.conbuildmat.2011.08.030.

[70] Mousavi SA, Zahrai SM, Bahrami-Rad A. Quasi-static cyclic tests on super-lightweight EPS concrete shear walls. Eng Struct 2014;65:62–75. https://doi.org/10.1016/j.engstruct.2014.02.003.

[71] Wang L, Aslani F, Hajirasouliha I, Roquino E. Ultra-lightweight engineered cementitious composite using waste recycled hollow glass microspheres. J Clean Prod 2020;249:119331. https://doi.org/10.1016/j.jclepro.2019.119331.

[72] Al-Gemeel AN, Zhuge Y, Youssf O. Use of hollow glass microspheres and hybrid fibres to improve the mechanical properties of engineered cementitious composite. Constr Build Mater 2018;171:858–70. https://doi.org/10.1016/j.conbuildmat.2018.03.172.

[73] Bubnov AS, Khorev VS, Boyko IA. The effect of lightweight agents on the density of cement slurry applied during oil and gas well drilling. IOP Conf. Ser. Earth Environ. Sci., Manchester: 2015. https://doi.org/10.1088/1755-1315/24/1/012008.

[74] US Energy Information Administration. How much energy is consumed in US building? 2019.

[75] Sadineni SB, Madala S, Boehm RF. Passive building energy savings: A review of building envelope components. Renew Sustain Energy Rev 2011;15:3617–31. https://doi.org/10.1016/j.rser.2011.07.014.

[76] Rheinheimer V, Wu Y, Wu T, Celik K, Wang J, De Lorenzis L, et al. Multi-scale study of high-strength low-thermal-conductivity cement composites containing cenospheres. Cem Concr Compos 2017;80:91–103. https://doi.org/10.1016/j.cemconcomp.2017.03.002.

[77] Priyanka E, Sathyan D, Mini KM. Functional and strength characteristics of EPS beads incorporated foam concrete wall panels. Mater Today Proc 2021:1–4. https://doi.org/10.1016/j.matpr.2021.01.592.

[78] Cavalline TL, Gallegos J, Castrodale RW, Freeman C, Liner J, Wall J. Influence of lightweight aggregate concrete materials on building energy performance. Buildings 2021;11:1–21. https://doi.org/10.3390/buildings11030094.

[79] Hawes DW, Feldman D. Absorption of phase change materials in concrete. Sol Energy Mater Sol Cells 1992;27:91–101.

[80] Hawes DW, Banu D, Feldman D. Latent Heat Storage in Concrete. Sol Energy Mater 1989;19:335–48.

[81] Drissi S, Ling T, Hung K, Eddhahak A. A review of microencapsulated and composite phase change materials: Alteration of strength and thermal properties of cement-based materials. Renew Sustain Energy Rev 2019;110:467–84. https://doi.org/10.1016/j.rser.2019.04.072.

[82] Cao DV, Pilehvar S, Salas-bringas C, Szczotok AM, Rodriguez JF, Carmona M, et al.

Microencapsulated phase change materials for enhancing the thermal performance of Portland cement concrete and geopolymer concrete for passive building applications. Energy Convers Manag 2017;133:56–66. https://doi.org/10.1016/j.enconman.2016.11.061.

[83] Liu Z, Jerry Z, Yang T, Qin D, Li S, Zhang G, et al. A review on macro-encapsulated phase change material for building envelope applications. Build Environ 2018;144:281–94. https://doi.org/10.1016/j.buildenv.2018.08.030.

[84] Kumar P, Rathore S, Shukla SK. Potential of macroencapsulated PCM for thermal energy storage in buildings : A comprehensive review. Constr Build Mater 2019;225:723–44. https://doi.org/10.1016/j.conbuildmat.2019.07.221.

[85] Drissi S, Eddhahak A, Caré S, Neji J. Thermal analysis by DSC of Phase Change Materials , study of the damage effect. J Build Eng 2015;1:13–9. https://doi.org/10.1016/j.jobe.2015.01.001.

[86] Frigione M, Lettieri M. Phase Change Materials for Energy Efficiency in Buildings and Their Use in Mortars. Materials (Basel) 2019;12:1–25.

[87] Ali S. Phase change materials integrated in building walls : A state of the art review. Renew Sustain Energy Rev 2014;31:870–906. https://doi.org/10.1016/j.rser.2013.12.042.

[88] Soares N, Costa JJ, Gaspar AR, Santos P. Review of passive PCM latent heat thermal energy storage systems towards buildings' energy efficiency. Energy Build 2013;59:82–103. https://doi.org/10.1016/j.enbuild.2012.12.042.

[89] Cellat K, Tezcan F, Beyhan B, Kardas G, Paksoy H. A comparative study on corrosion behavior of rebar in concrete with fatty acid additive as phase change material. Constr Build Mater 2017;143:490–500. https://doi.org/10.1016/j.conbuildmat.2017.03.165.

[90] Vicente R, Silva T. Brick masonry walls with PCM macrocapsules: An experimental approach. Appl Therm Eng 2014;67:24–34. https://doi.org/10.1016/j.applthermaleng.2014.02.069.

[91] Cui H, Tang W, Qin Q, Xing F, Liao W, Wen H. Development of structural-functional integrated energy storage concrete with innovative macro-encapsulated PCM by hollow steel ball. Appl Energy 2020;185:107–18. https://doi.org/10.1016/j.apenergy.2016.10.072.

[92] Chandel SS, Agarwal T. Review of current state of research on energy storage, toxicity, health hazards and commercialization of phase changing materials. Renew Sustain Energy Rev 2017;67:581–96. https://doi.org/10.1016/j.rser.2016.09.070.

[93] Hunger M, Entrop AG, Mandilaras I, Brouwers HJH, Founti M. The behavior of self-compacting concrete containing micro-encapsulated Phase Change Materials. Cem Concr Compos 2009;31:731–43. https://doi.org/10.1016/j.cemconcomp.2009.08.002.

[94] Djamai ZI, Salvatore F, Larbi AS, Cai G, Mankibi M El. Cement and Concrete Research Multiphysics analysis of effects of encapsulated phase change materials (PCMs) in cement mortars. Cem Concr Res 2019;119:51–63. https://doi.org/10.1016/j.cemconres.2019.02.002.

[95] Djamai ZI, Salvatore F, Larbi AS, Cai G, Mankibi M El. Multiphysics analysis of effects

of encapsulated phase change materials (PCMs) in cement mortars. Cem Concr Res 2019;119:51–63. https://doi.org/10.1016/j.cemconres.2019.02.002.

[96] Hunger M, Entrop AG, Mandilaras I, Brouwers HJH, Founti M. The behavior of self-compacting concrete containing micro-encapsulated Phase Change Materials. Cem Concr Compos 2009;31:731–43. https://doi.org/10.1016/j.cemconcomp.2009.08.002.

[97] Cabeza LF, Castellón C, Nogués M, Medrano M, Leppers R, Zubillaga O. Use of microencapsulated PCM in concrete walls for energy savings. Energy Build 2007;39:113–9. https://doi.org/10.1016/j.enbuild.2006.03.030.

[98] Gencel O, Sarı A, Kaplan G, Ustaoglu A, Hekimoğlu G, Bayraktar OY, et al. Properties of eco-friendly foam concrete containing PCM impregnated rice husk ash for thermal management of buildings. J Build Eng 2022;58. https://doi.org/10.1016/j.jobe.2022.104961.

[99] Rucevskis S, Akishin P, Korjakins A. Performance Evaluation of an Active PCM Thermal Energy Storage System for Space Cooling in Residential Buildings. Environ Clim Technol 2019;23:74–89. https://doi.org/10.2478/rtuect-2019-0056.

[100] Das S, Aguayo M, Rajan SD, Sant G, Neithalath N. Microstructure-guided numerical simulations to predict the thermal performance of a hierarchical cement-based composite material. Cem Concr Compos 2018;87:20–8. https://doi.org/10.1016/j.cemconcomp.2017.12.003.

[101] Garboczi EJ, Bentz DP. Analytical formulas for interfacial transition zone properties. Adv Cem Based Mater 1997;6:99–108.

[102] AkzoNobel. Expancel® 461 DET 40 d25 datasheet. 2017.

[103] 3M. 3M Glass Bubbles K Series, S Series and iM Series. 2009.

[104] ISO22007-2:2008. Plastics - Determination of thermal conductivity and thermal diffusivity - Part 2: Transient plane source method. 2008.

[105] Log T, Gustafsson S. Transient Plane Source (TPS) technique for measuring thermal transport properties of building material. Fire Mater 1995;19:43–9.

[106] ASTM C1363. Standard Test Method for Thermal Performance of Building Materials and Envelope Assemblies by Means of a Hot Box Apparatus. 2005. https://doi.org/10.1520/C1363-11.2.

[107] Kaviany K. Principles of Heat Transfer in Porous Media (Mechanical Engineering Series). Berlin: Springer; 1995. https://doi.org/10.1016/j.applthermaleng.2011.11.001.

[108] Le Roy R, Parant E, Boulay C. Taking into account the inclusions' size in lightweight concrete compressive strength prediction. Cem Concr Res 2005;35:770–5. https://doi.org/10.1016/j.cemconres.2004.06.002.

[109] Felske JD. Effective thermal conductivity of composite spheres in a continuous medium with contact resistance. Int J Heat Mass Transf 2004;47:3453–61. https://doi.org/10.1016/j.ijheatmasstransfer.2004.01.013.

[110] Bielders CL, De Backer LW, Delvaux B. Particle Density of Volcanic Soils as Measured

with a Gas Pycnometer. Soil Sci Soc Am J 1990;54:822. https://doi.org/10.2136/sssaj1990.03615995005400030034x.

[111] Thiele AM, Wei Z, Falzone G, Young B a., Neithalath N, Sant G, et al. Figure of merit for the thermal performance of cementitious composites containing phase change materials. Cem Concr Compos 2016;65:214–26. https://doi.org/10.1016/j.cemconcomp.2015.10.023.

[112] Norris AN, Callegari AJ, Sheng P. A generalized differential effective medium theory. J Mech Phys Solids 1985;33:525–43. https://doi.org/10.1016/0022-5096(85)90001-8.

[113] Pal R. Thermal conductivity of three-component composites of core-shell particles. Mater Sci Eng A 2008;498:135–41. https://doi.org/10.1016/j.msea.2007.10.123.

[114] Lee YM, Yang R Bin, Gau SS. A generalized self-consistent method for calculation of effective thermal conductivity of composites with interfacial contact conductance. Int Commun Heat Mass Transf 2006;33:142–50. https://doi.org/10.1016/j.icheatmasstransfer.2005.10.004.

[115] Clarke JL, editor. Structural Lightweight Aggregate Concrete. London and New York: Blackie Academic & Professional; 1993.

[116] Kearsley EP, Wainwright PJ. Effect of porosity on the strength of concrete. Cem Concr Res 2002;32:233–9.

[117] Fomenko E, Anshits N, Vasil'eva NG, Rogovenko ES, Mikhaylova OA, Mazurova E V, et al. Composition and Structure of the Shells of Aluminosilicate Microspheres in Fly Ash Formed on the Combustion of Ekibastuz Coal. Solid Fuel Chem 2016;50:238–47. https://doi.org/10.3103/S0361521916040030.

[118] Xie Y, Mcallister SD, Edwards DB, Cheng IF. Fabrication of porous hollow glass microspheres. J Power Sources 2011;196:10727–30. https://doi.org/10.1016/j.jpowsour.2011.07.049.

[119] Fomenko E V, Bobko AA, Salanov AN, Kirilyuk IA, Grigorev IA, Khromtsov V V, et al. Perforated cenosphere supported pH sensitive spin probes. Russ Chem Bull 2008;57:493–8.

[120] Liston L, Krafcik M, Farnam Y, Tao B, Erk K, Weiss J. Toward the Use of Phase Change Materials (PCM) in Concrete Pavements: Evaluation of Thermal Properties of PCM. 2014 FAA Worldw. Airpt. Technol. Transf. Conf., Galloway, NJ: 2014, p. 1–14.

[121] Gustafsson SE. Transient diffusivity plane source techniques for thermal conductivity measurements of solid materials and thermal. Rev Sci Instrum 1991;62:797–804.

[122] ISO 22007-2. Plastics - Determination of thermal conductivity and thermal diffusivity - Part 2: Transient plan heat source (hot disc) method 2015.

[123] He Y. Rapid thermal conductivity measurement with a hot disk sensor: Part 1. Theoretical considerations. Thermochim Acta 2005;436:122–9. https://doi.org/10.1016/j.tca.2005.06.026.

[124] ASTM C1421. Standard Test Methods for Determination of Fracture Toughness of Advanced Ceramics at Ambient Temperature. ASTM; 2018.

https://doi.org/10.1520/C1421-18.

[125] Banthia N, Sheng J. Fracture toughness of micro-fiber reinforced cement composites. Cem Concr Compos 1996;18:251–69. https://doi.org/10.1016/0958-9465(95)00030-5.

[126] Shen Z, Zhou H. Predicting effective thermal and elastic properties of cementitious composites containing polydispersed hollow and core-shell micro-particles. Cem Concr Compos 2020;105:103439. https://doi.org/10.1016/j.cemconcomp.2019.103439.

[127] Li W, Ji W, Isfahani FT, Wang Y, Li G, Liu Y, et al. Nano-Silica Sol-Gel and Carbon Nanotube Coupling Effect on the Performance of Cement-Based Materials. Nanomaterials 2017;7:1–15. https://doi.org/10.3390/nano7070185.

[128] Sagar RV, Prasad R V, Ragji Prasad BK, Rao MVM. Microcracking and Fracture Process in Cement Mortar and Concrete: A Comparative Study Using Acoustic Emission Technique. Exp Mech 2013;53:1161–75. https://doi.org/10.1007/s11340-012-9708-z.

[129] Yu QL, Spiesz P, Brouwers HJH. Ultra-lightweight concrete: Conceptual design and performance evaluation. Cem Concr Compos 2015;61:18–28. https://doi.org/10.1016/j.cemconcomp.2015.04.012.

[130] Berge A, Adl-Zarrabi B, Hagentoft CE. Determination of specific heat capacity by transient plane source. Front Archit Res 2013;2:476–82. https://doi.org/10.1016/j.foar.2013.09.004.

[131] Yan H, Sun W, Chen H. Effect of silica fume and steel fiber on the dynamic mechanical performance of high-strength concrete. Cem Concr Res 1999;29:423–6. https://doi.org/10.1016/S0008-8846(98)00235-X.

[132] Nguyen LH, Beaucour a. L, Ortola S, Noumowé a. Influence of the volume fraction and the nature of fine lightweight aggregates on the thermal and mechanical properties of structural concrete. Constr Build Mater 2014;51:121–32. https://doi.org/10.1016/j.conbuildmat.2013.11.019.

[133] Valore RCJ. Calculation of U-Values of Hollow Concrete Masonry. Concr Int Am Concr Institue 1980;2:40–63.

[134] Valore RC. The Thermophysical Properties of Masonry and Its Constituents. Washington, DC: International Masonry Institute; 1988.

[135] ACI Committee 122. Guide to Thermal Properties of Concrete and Masonry Systems. 2002.

[136] Clauser C, Huenges E. Thermal Conductivity of Rocks and Minerals. In: Ahrens TJ, editor. Rock Phys. Phase Relations A Handb. Phys. Constants. Therm. Conduct. Rocks Miner., 1995, p. 105–26. https://doi.org/10.1029/RF003.

[137] Pietrak K, Wisniewski TS. A review of models for effective thermal conductivity of composite materials. J Power Technol 2015;95:14–24.

[138] Hochstein DP. Thermal Conductivity of Fiber-Reinforced Lightweight Cement Composites. Columbia University, 2013.

[139] Wu T, Temizer I, Wriggers P. Computational thermal homogenization of concrete. Cem

Concr Compos 2013;35:59–70. https://doi.org/10.1016/j.cemconcomp.2012.08.026.

[140] Valore RC, Green WC. Air Replaces Sand in “No-Fines” Concrete. ACI Mater J 1951;47:833–45.

[141] Choy TC. Effective medium theory: Principles and applications monographs on physics. Oxford University Press; 1999.

[142] Rigol Technologies Inc. Rigol Programming Guide: DP800 Series Programmable Linear DC Power Supply. 2015.

[143] Schumacher CJ, Ober DG, Straube JF, Grin AP. Development of a New Hot Box Apparatus to Measure Building Enclosure Thermal Performance. ASHRAE Therm. Perform. Exter. Envel. Whole Build. XII Int. Conf., 2013, p. 1–19.

[144] ASTM C1363. Standard Test Method for Thermal Performance of Building Materials and Envelope Assemblies by Means of a Hot Box Apparatus. 2018. https://doi.org/10.1520/C1363-11.2.

[145] Shen Z, Brooks AL, He Y, Shrestha SS, Zhou H. Evaluating dynamic thermal performance of building envelope components using small-scale calibrated hot box tests. Energy Build 2021;251:111342. https://doi.org/10.1016/J.ENBUILD.2021.111342.

[146] Awan AB, Shaikh FUA. Structural behavior of recycled tire crumb rubber sandwich panel in flexural bending. Struct Concr 2021;22:3602–19. https://doi.org/10.1002/suco.202100356.

[147] Awan AB, Shaikh FUA. Compressive behavior of precast concrete sandwich panels containing recycled tyre crumb rubber core. Struct Concr 2022;23:2786–802. https://doi.org/10.1002/suco.202100470.

[148] Gosselin C, Duballet R, Roux P, Gaudillière N, Dirrenberger J, Morel P. Large-scale 3D printing of ultra-high performance concrete - a new processing route for architects and builders. Mater Des 2016;100:102–9. https://doi.org/10.1016/j.matdes.2016.03.097.

[149] Park L. Section 2: hazards identification 2.1. 2019;77:1–10.

[150] Reiter L, Wangler T, Roussel N, Flatt RJ. The role of early age structural build-up in digital fabrication with concrete. Cem Concr Res 2018;112:86–95. https://doi.org/10.1016/j.cemconres.2018.05.011.

[151] Ma G, Li Z, Wang L. Printable properties of cementitious material containing copper tailings for extrusion based 3D printing. Constr Build Mater 2018;162:613–27. https://doi.org/10.1016/j.conbuildmat.2017.12.051.

[152] Perrot A, Mélinge Y, Rangeard D, Micaelli F, Estellé P, Lanos C. Use of ram extruder as a combined rheo-tribometer to study the behaviour of high yield stress fluids at low strain rate. Rheol Acta 2012;51:743–54. https://doi.org/10.1007/s00397-012-0638-6.

[153] Perrot A, Lanos C, Estellé P, Melinge Y. Ram extrusion force for a frictional plastic material: Model prediction and application to cement paste. Rheol Acta 2006;45:457–67. https://doi.org/10.1007/s00397-005-0074-y.

[154] Perrot A, Rangeard D, Mélinge Y. Prediction of the ram extrusion force of cement-based

materials. Appl Rheol 2014;24. https://doi.org/10.3933/APPLRHEOL-24-53320.

[155] Brooks AL, Fang Y, Shen Z, Wang J, Zhou H. Enabling high-strength cement-based materials for thermal energy storage via fly-ash cenosphere encapsulated phase change materials. Cem Concr Compos 2021;120:104033. https://doi.org/10.1016/j.cemconcomp.2021.104033.

[156] Shen Z, Zhou H, Brooks A, Hanna D. Evolution of elastic and thermal properties of cementitious composites containing micro-size lightweight fillers after exposure to elevated temperature. Cem Concr Compos 2021;118:103931. https://doi.org/10.1016/j.cemconcomp.2021.103931.

[157] Zhou H, Brooks A, Shen Z. A monolithic “unibody” construction of structural assemblies through vacuum-assisted processing of agro-waste fiberous composites. Submitt Constr Mater 2016.

[158] Microtek. Micronal 24D Material Safety Data Sheet 2019:2019.

[159] Rahul A V, Santhanam M, Meena H, Ghani Z. Mechanical characterization of 3D printable concrete. Constr Build Mater 2019;227:116710. https://doi.org/10.1016/j.conbuildmat.2019.116710.

Vita

Adam Brooks is a PhD student in the Civil and Environmental Engineering Department at the

University of Tennessee, Knoxville. He received his BS and MS from The University of Alabama in Huntsville, Huntsville, AL. Along with his work as a graduate student he currently works at Oak Ridge National Lab where he will continue to pursue research in the areas of irradiated concrete, additively manufactured concrete, and alternative binders. He is an active member of ACI technical committees 555- Concrete with Recycled Materials, 349 – Nuclear Structures and 378- Concrete Wind Turbine Towers.